Corina Kräuter, BSc

Pixel-wise quantification of myocardial perfusion indices from dynamic contrast-enhanced MRI

MASTER'S THESIS

to achieve the university degree of

Diplom-Ingenieurin

Master's degree programme: Biomedical Engineering

submitted to

Graz University of Technology

Supervisor

Univ.-Prof. Dipl.-Ing. Dr.techn. Rudolf Stollberger

Institute of Medical Engineering

Second supervisor: Dipl.-Ing. Dr.techn. Gert Reiter
Research and Development, Siemens Healthcare Diagnostics GmbH

Graz, October 2016

AFFIDAVIT

I declare that I have authored this thesis independently, that I have not used other than the declared sources/resources, and that I have explicitly indicated all material which has been quoted either literally or by content from the sources used. The text document uploaded to TUGRAZonline is identical to the present master‘s thesis dissertation.

Date

Signature

Acknowledgments

First of all, I would like to thank Prof. Dr. Rudolf Stollberger for his guidance and contribution to this thesis. Special thanks go to Dr. Gert Reiter and Dr. Ursula Reiter for their unequaled support and advice, for sharing their knowledge about cardiac MRI and for always being patient and highly motivated. I would also like to thank my parents for their unconditional support and for believing in me. A final thank goes to my friends and colleagues, especially Marc, Flo, Betti, Ines and Fanny, who have always been there for me.

The project was supported by the funds of the Österreichische Nationalbank, Anniversary Fund (grant number 141223, title "Kardiale Blutflussmuster bei chronischer KHK: Eine explorative Studie mit Magnetrsonanztomographie", project lead DI Dr.tech. Ursula Reiter).

Abstract

Pixel-wise perfusion quantification from dynamic contrast-enhanced magnetic resonance imaging (DCE-MRI) might allow detection and evaluation of myocardial perfusion deficits beyond visual analysis. However, relationships between different quantification approaches were not thoroughly studied. The aim of this thesis was to determine and compare semi-quantitative (up-slope, area under the curve and signal intensity maximum) and quantitative (deconvolution using Fermi modeling, Tikhonov regularization with B-splines and ARMA modeling) perfusion parameter maps from motion-corrected myocardial DCE-MRI data acquired in patients with coronary heart disease under resting condition.
Visual analysis for subendocardial perfusion deficits revealed the best sensitivity (100%) and specificity (100%) for signal intensity maximum maps. For no type of perfusion map dark rim artifacts were misinterpreted as perfusion deficits. Whereas semi-quantitative and quantitative parameters demonstrated only moderate correlations both pixel-based and patient-based, the correlations between different quantitative perfusion maps were strong. However, mean myocardial perfusion values of 0.72 ± 0.13 (Fermi), 0.67 ± 0.10 (Tikhonov) and 0.84 ± 0.16 $ml \cdot min^{-1} \cdot g^{-1}$(ARMA) differed significantly.
Consequently, pixel-wise myocardial perfusion quantification is feasible with any of the studied approaches, where practical aspects favor the deconvolution using Fermi modeling. Semi-quantitative parameters do not completely reflect quantitative myocardial perfusion, but signal intensity maximum maps represent a valuable tool for detection of perfusion deficits.

Key words: dynamic contrast-enhanced magnetic resonance imaging, myocardial perfusion, deconvolution, signal intensity to concentration conversion, perfusion parameters

Kurzfassung

Pixelweise Perfusionsquantifizierung unter Verwendung von dynamischer kontrastmittelverstärkter Magnetresonanztomographie (DCE-MRI) könnte eine Feststellung und Beurteilung myokardialer Perfusionsdefizite über die visuelle Analyse hinaus ermöglichen. Die Beziehungen zwischen verschiedenen Quantifizierungsmethoden wurde jedoch noch nicht gründlich untersucht. Das Ziel dieser Arbeit war es, semi-quantitative (Anstiegssteilheit, Fläche unter der Kurve und Signalintensitätsmaximum) und quantitative (Entfaltung mittels Fermi-Modell, Tikhonov Regularisierung mit B-Splines und ARMA-Modell) Perfusionsparameter-Maps aus bewegungskorrigierten myokardialen Ruheperfusions-DCE-MRI Daten von Patienten mit koronarer Herzkrankheit zu bestimmen und zu vergleichen.
Die visuelle Analyse subendokardialer Perfusionsdefizite ergab die beste Sensitivität (100%) und Spezifität (100%) für die Signalintensitätsmaximum-Maps. In keiner Art von Perfusions-Maps wurden Dark Rim Artefakte als Perfusionsdefizit missinterpretiert. Während semi-quantitative und quantitative Parameter sowohl pixelbasiert als auch patientenbasiert nur mittelmäßige Korrelationen aufwiesen, waren die Korrelationen zwischen den verschiedenen quantitativen Myokardperfusions-Maps stark. Allerdings unterschieden sich die mittleren Myokardperfusionswerte von 0.72 ± 0.13 (Fermi), 0.67 ± 0.10 (Tikhonov) und 0.84 ± 0.16 $ml \cdot min^{-1} \cdot g^{-1}$(ARMA) signifikant.
Pixelweise Myokardperfusionsquantifizierung war demzufolge mit allen untersuchten Methoden möglich, wobei die Entfaltung mittels Fermi-Modell aufgrund praktischer Aspekte zu bevorzugen ist. Semi-quantitative Parameter spiegeln quantitative Myokardperfusion nicht vollkommen wider, Signalintensitätsmaximum-Maps sind aber ein wertvolles Hilfsmittel zur Detektion von Perfusionsdefiziten.

Schlüsselwörter: dynamische kontrastmittelverstärkte Magnetresonanztomographie, Myokardperfusion, Entfaltung, Umrechnung von Signalintensität auf Konzentration, Perfusionsparameter

Contents

List of Abbreviations viii

List of Figures x

List of Tables xiii

1 Introduction 1

1.1 The left ventricular myocardium and its perfusion 1

1.2 Dynamic contrast-enhanced magnetic resonance imaging of the myocardium 3

1.2.1 Imaging principle 3

1.2.2 Paramagnetic relaxation enhancement 4

1.2.3 Myocardial DCE-MRI procedure 6

1.2.4 Sequence technique for myocardial DCE-MRI 7

1.2.5 Relationship between signal intensity and contrast agent concentration 10

1.3 Perfusion quantification from myocardial DCE-MRI 12

1.3.1 Semi-quantitative analysis 13

1.3.2 Quantitative analysis 14

1.4 Aim of the thesis 19

2 Methods 21

2.1 Study population 21

2.2 MRI acquisition 21

2.3 Overview of the data processing pipeline 23

2.4 Preprocessing . . . 25
2.4.1 Automated heart bounding box extraction . . . 25
2.4.2 Segmentation . . . 27
2.4.3 Signal intensity to concentration conversion . . . 28
2.4.4 Resampling for uniform time spacing . . . 29
2.4.5 Motion correction quality map and outlier detection . . . 30
2.4.6 Denoising for semi-quantitative analysis . . . 32
2.5 Perfusion quantification . . . 39
2.5.1 Semi-quantitative analysis . . . 39
2.5.2 Quantitative analysis . . . 41
2.6 Analysis of quantitative perfusion maps . . . 50
2.7 Phantom experiment . . . 51
2.8 Statistical analysis . . . 53

3 Results **55**

3.1 Phantom experiment . . . 55
3.2 Denoising for semi-quantitative analysis . . . 55
3.2.1 Automated PCA filter . . . 57
3.2.2 Savitzky-Golay filter . . . 57
3.2.3 Comparison of denoising methods . . . 57
3.3 Semi-quantitative analysis of SI data . . . 58
3.4 Semi-quantitative analysis of [CA] data . . . 58
3.4.1 Visual analysis and global indices . . . 60
3.4.2 Correlation between semi-quantitative parameters of SI and [CA] data 61
3.5 Quantitative analysis . . . 64
3.5.1 Typical single pixel results . . . 64
3.5.2 Visual analysis and global indices . . . 64
3.5.3 Correlation between MBF and semi-quantitative parameters of SI data . . . 66

3.5.4 Correlation between MBF and semi-quantitative parameters of [CA] data 68
3.5.5 Correlation between MBF methods 70
3.5.6 Motion correction quality map and outlier detection 73

4 Discussion **75**
4.1 Deconvolution analysis 75
4.2 Semi-quantitative analysis 79
4.3 Visual analysis 81
4.4 Outlier detection 82
4.5 Limitations 83
4.6 Conclusion 86

Bibliography **88**

List of Abbreviations

[CA]	Contrast Agent Concentration
AIF	Arterial Input Function
ARMA	Autoregressive Moving Average
AUC	Area Under the Curve
CA	Contrast Agent
CNR	Contrast-to-Noise-Ratio
CT	Computed Tomography
DCE-MRI	Dynamic Contrast-Enhanced Magnetic Resonance Imaging
ECG	Electrocardiogram
FLASH	Fast Low-Angle Shot
FRI	Fraction of Residual Information
Gd-CA	Gadolinium-based Contrast Agent
GRAPPA	Generalized Auto-calibrating Partially Parallel Acquisition
GRE	Gradient Echo
GSVD	Generalized Singular Value Decomposition
IIR	Infinite Impulse Response
LCCDE	Linear Constant Coefficient Difference Equation
LE	Late Enhancement

LV	Left Ventricle/Ventricular
MBF	Myocardial Blood Flow
MIP	Maximum Intensity Projection
mIP	Minimum Intensity Projection
MOLLI	Modified Look-Locker Inversion Recovery
MPRI	Myocardial Perfusion Reserve Index
MRI	Magnetic Resonance Imaging
OS	Outlier Suppression/Suppressed
PCA	Principal Component Analysis
PET	Positron Emission Tomography
RF	Radio Frequency
ROI	Region of Interest
RV	Right Ventricle/Ventricular
SD	Standard Deviation
SG	Savitzky-Golay
SI	Signal Intensity
SIM	Signal Intensity Maximum
SNR	Signal-to-Noise-Ratio
SR	Saturation Recovery
SSFP	Steady-State Free Precession
SVD	Singular Value Decomposition
TTP	Time-to-Peak
US	Up-Slope

List of Figures

1.1 Coronary system traversing the myocardium 2
1.2 DCE images of a short axis slice of the heart and corresponding SI time curves extracted from LV and myocardium 5
1.3 Selected images of a DCE series showing a subendocardial perfusion deficit 5
1.4 ECG-triggered acquisition of multiple slices 7
1.5 Longitudinal magnetization recovery after saturation pulse application . . . 8
1.6 Comparison of dark rim artifact and real perfusion deficit 9
1.7 Semi-quantitative parameters 14
1.8 Schematic myocardial capillary-tissue system characterized by its impulse response functions 15
1.9 AIF, impulse responses to AIF and tissue curve resulting from summation of impulse responses 17

2.1 Data processing pipeline 24
2.2 Image processing steps for the extraction of a ROI containing the heart . . 26
2.3 Comparison of an image of the DCE series with good contrast and the signal intensity maximum map 27
2.4 Exemplary T_1 map with ROIs in myocardium and LV blood pool 29
2.5 Example of resampling using `pchip` 30
2.6 Dependency of the amount of information and noise in PCA transformed data on the principal component number 33
2.7 FRI map and histogram for an increasing number of principal components 35

2.8 Generic form of the L-curve 46
2.9 Exemplary impulse responses determined with model-independent deconvolution for different time shifts between AIF and myocardial curve. 48
2.10 Segmentation of the myocardium and the ROI in the LV blood pool 51
2.11 MBF maps determined with Fermi modeling, Tikhonov regularization with B-splines and ARMA modeling 52
2.12 Photo of the phantom 53

3.1 Measured phantom signal intensity as a function of contrast agent concentration 56
3.2 Relationship between ground truth concentration and the concentration derived via the signal intensity model 56
3.3 Direct comparison of the results of SI time curve denoising with PCA and Savitzky-Golay filter 57
3.4 Comparison of semi-quantitative parameter maps obtained from PCA and SG filtered data 59
3.5 Typical semi-quantitative parameter maps of $[CA]$ data 61
3.6 Scatter plots of normalized global mean values of SI and $[CA]$ semi-quantitative parameters 62
3.7 Scatter plots of normalized SI and $[CA]$ semi-quantitative parameters of all myocardial pixels of all patients 63
3.8 Typical impulse responses and myocardial curve fits 65
3.9 Mean and standard deviation of the global mean MBF values of all patients determined with the three deconvolution methods. 66
3.10 Scatter plots relating semi-quantitative parameters of SI data and MBF . . 67
3.11 Scatter plots relating semi-quantitative parameters of $[CA]$ data and MBF 69
3.12 Scatter plots relating all patients' global mean MBF determined with Fermi modeling, Tikhonov regularization with B-splines and ARMA modeling . . 71

3.13 Scatter plots relating MBF values of all myocardial pixels of all patients determined with Fermi modeling, Tikhonov regularization with B-splines and ARMA modeling 72
3.14 Typical motion correction quality map and result of outlier detection . . . 73
3.15 Selected images of a DCE series with imperfect motion correction 73

4.1 Exemplary sigmoid function fit to typical and distorted myocardial $[CA]$ time curves 82
4.2 AIF and exemplary myocardial tissue curve of each patient excluded from comparative analysis 84

List of Tables

2.1 Contrast agent concentrations in the different bottles of the phantom. . . . 53

3.1 Specificity and sensitivity for visual detection of perfusion deficits in semi-quantitative parameter maps of SI data 60
3.2 Mean, standard deviation and range of the normalized global mean values of the SI semi-quantitative parameters of all patients 60
3.3 Specificity and sensitivity for visual detection of perfusion deficits in semi-quantitative parameter maps of $[CA]$ data 61
3.4 Mean, standard deviation and range of the normalized global mean values of the $[CA]$ semi-quantitative parameters of all patients 62
3.5 Correlation between respective SI and $[CA]$ semi-quantitative parameters . 62
3.6 Specificity and sensitivity for visual detection of perfusion deficits in MBF maps determined with Fermi modeling, Tikhonov regularization with B-splines and ARMA modeling 65
3.7 Correlation between SI semi-quantitative parameters and MBF determined with Fermi modeling, Tikhonov regularization with B-splines and ARMA modeling 68
3.8 Correlation between $[CA]$ semi-quantitative parameters and MBF determined with Fermi modeling, Tikhonov regularization with B-splines and ARMA modeling 70

3.9 Correlation between MBF results obtained with Fermi modeling, Tikhonov regularization with B-splines and ARMA modeling with and without outlier suppression 71

1 Introduction

Magnetic resonance imaging (MRI) has been applied for more than two decades for the assessment of myocardial perfusion. Compared to the gold standard method positron emission tomography (PET), it has the advantages of superior spatial resolution and absence of ionizing radiation. While visual analysis of MR images acquired during the passage of a contrast agent bolus through the heart is clinical routine, approaches to quantitative evaluation of myocardial perfusion are still at the stage of active research. Heterogeneity in quantification methodology as well as lack of studies with large patient populations complicate the implementation into clinical practice. However, semi-quantitative and quantitative perfusion studies have shown the potential to improve and enlarge diagnostic capabilities of MRI in the evaluation of impaired myocardial perfusion.
This chapter first provides a short introduction to anatomy and (patho-)physiology of the myocardium, followed by a description of dynamic contrast-enhanced magnetic resonance imaging (DCE-MRI) of the heart. Then, the concepts and methods of semi-quantitative and quantitative myocardial perfusion analysis are introduced and finally, the aim of this thesis is stated.

1.1 The left ventricular myocardium and its perfusion

The left ventricular myocardium - hereafter referred to as myocardium - is the cardiac muscle tissue lying between the interior single layer of endothelial cells, the endocardium, and the outermost layer of the heart, the epicardium. The rhythmic contraction of the

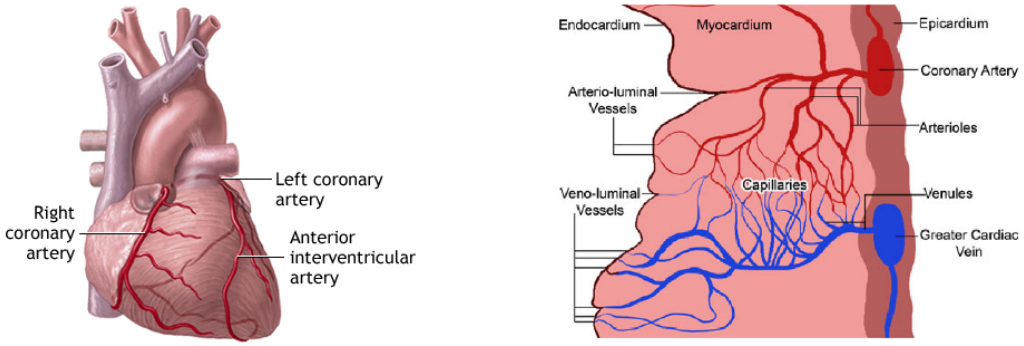

(a) (b)

Figure 1.1: Epicardial coronary arteries (a) and coronary system traversing the myocardium (b). Images taken from [1] and [2], respectively.

cardiac muscle causes the transport of blood through the body and thereby ensures the oxygen and nutritional supply of the body's tissues. The heart muscle itself is supplied with oxygenated blood by the large left and right epicardial coronary arteries, which originate from the root of the aorta and divide into a system of branches that traverse the myocardium (see Figure 1.1). Muscle fibers very close to the endocardium receive blood also directly from the ventricular cavity via the tiny arterio-luminal vessels. Blood flow through these auxiliary vascular channels account only for a small percentage of myocardial blood supply and it has no significance when a large coronary artery gets occluded [3]. The exchange of oxygen between blood and myocardial tissue occurs at the level of the capillaries [4].

Blood flow per myocardial tissue mass is called myocardial perfusion. In a healthy heart, the coronary blood flow and myocardial perfusion are adjusted by autoregulatory mechanisms so that the delivery of oxygen matches the requirements of the myocardium at rest as well as under stress conditions. The higher oxygen demand under stress conditions may cause up to four to sixfold increases in myocardial perfusion in normal individuals [5]. The relative increase of myocardial stress perfusion with respect to rest perfusion is also termed perfusion reserve.

In an ischemic heart, the blood supply to the muscle tissue is impaired. The vulnerability for ischemia is especially high in the subendocardium of the thick-walled left ventricular

myocardium [3, 5]. Insufficient supply of blood and oxygen even to small areas of the myocardium may result in mechanical dysfunction, arrhythmia as well as cardiac cell death and myocardial infarction [6]. A frequent cause for ischemia of the myocardium is the presence of coronary heart disease, where typically the transport of blood through the large epicardial coronary arteries is restricted by stenoses. Such stenoses do not cause reduced myocardial perfusion under resting conditions as long as the trans-stenotic pressure gradient can be compensated by a dilatation of the microvasculature. However, the ability to respond to stress is reduced and at higher stress levels ischemia might result [4].

1.2 Dynamic contrast-enhanced magnetic resonance imaging of the myocardium

1.2.1 Imaging principle

Dynamic contrast-enhanced magnetic resonance imaging (DCE-MRI) of tissue visualizes the passage of intravenously administered contrast agent (CA) by acquiring a time series of MR images of the tissue of interest. As the contrast agent is transported with blood through the vascular system of the tissue, resulting temporal signal intensity (SI) changes may allow for the derivation of perfusion-related parameters of the tissue. In myocardial DCE-MRI studies the focus lies on the first passage of contrast agent through the myocardium because this is the phase where contrast enhancement is most sensitive to alterations in myocardial blood flow [7]. Figure 1.2 shows selected images from a typical DCE series of a short-axis slice of the heart. MR imaging starts in parallel with the intravenous bolus administration of contrast agent. As the contrast agent needs some time to arrive at the heart, a few baseline images without any contrast enhancement in the imaging slice are acquired. Then the contrast agent passes through the right ventricular (RV) cavity and – via the lung – to the left ventricular cavity (LV) in order to finally arrive in the myocardium. SI time curves for a pixel in the LV and in the myocardium in Figure 1.2 indicate that CA appears

as a bolus in the LV causing an increase of CA concentration in the myocardium. The second peak of the LV SI time curve suggests already the presence of recirculating CA in the LV.

It is common to evaluate myocardial DCE series purely visually based on regionally different contrast enhancement in the myocardium during the first passage of contrast agent. Locally reduced contrast agent enhancement is identified as regional perfusion deficit (see Figure 1.3). When performing this type of visual analysis for myocardial DCE-MRI under pharmacological stress and – for comparative reasons – resting conditions, high diagnostic accuracy for the identification of relevant coronary artery stenoses in patients with coronary heart disease has been shown [8]. Obvious disadvantages of the visual analysis are, however, that neither diffuse alterations in myocardial perfusion can be detected nor perfusion reserves can be specified.

1.2.2 Paramagnetic relaxation enhancement

Myocardial DCE-MRI is commonly performed using gadolinium-based contrast agents (Gd-CA) [7]. There exist intravascular and extracellular Gd-CAs, the former remaining to a very large extent in the vascular blood pool and the latter leaking from the blood vessels into the interstitial space of the tissue without entering myocardial cells. In clinical practice, however, extracellular Gd-CAs are almost exclusively chosen because of their excellent safety profile and clinical approval [9]. The latter Gd-CAs are all available as chelates dissolved in concentrations of 0.5 mmol/ml or 1.0 mmol/ml. They are typically administered intravenously into the antecubital vein at high injection rate (3 - 7 ml/s), directly followed by a saline solution flush aiming to achieve a tight bolus and sharp increase of concentration in the (well-perfused) myocardium [7, 10, 11].
Gd-CAs are, due to gadolinium's seven unpaired electrons, highly paramagnetic and shorten the T_1 and T_2/T_2^* relaxation times of nearby water protons in tissue [9]. Myocardial DCE-MRI employs especially the T_1-shortening effect to generate higher signal intensities in regions with higher Gd-CA concentration by acquisition of heavily T_1-weighted images.

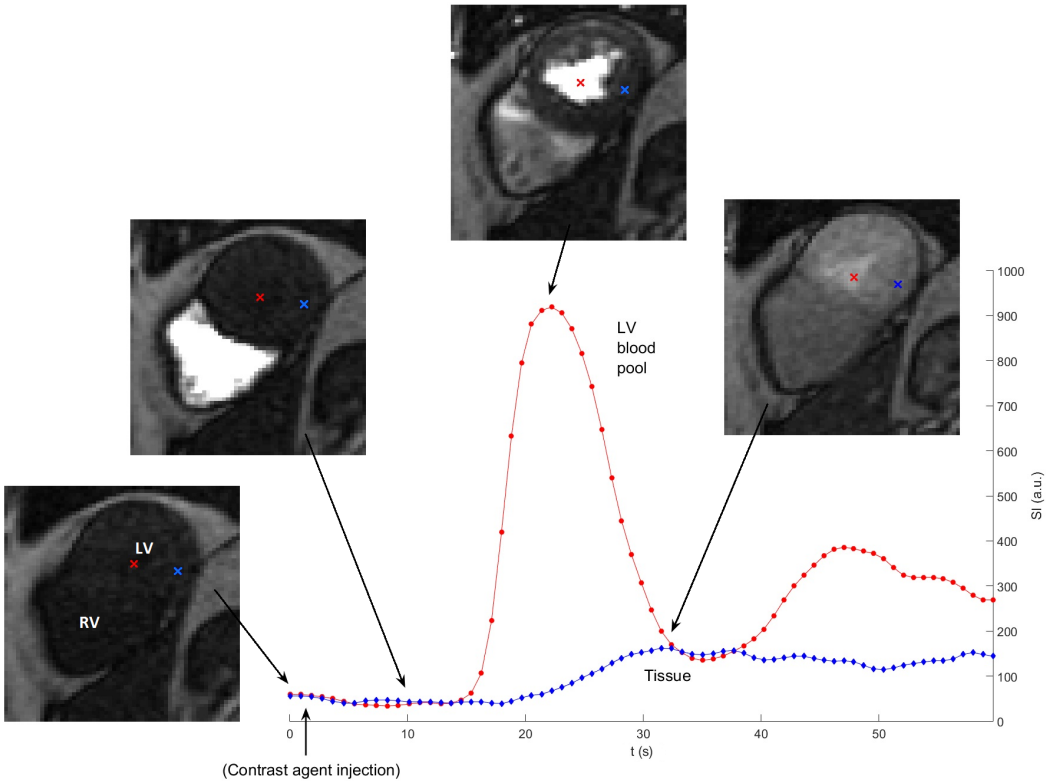

Figure 1.2: Selected images from a DCE series of a the short axis slice of the heart illustrate the contrast enhancement at the time point of intravenous contrast agent injection and at the time points of contrast agent appearance in the right ventricular (RV) cavity, in the left ventricular (LV) cavity and in the myocardium. The corresponding SI time curves extracted from single pixels of LV and myocardial tissue (marked in the DCE images by a red and a blue cross, respectively) indicate a sharp increase of contrast agent concentration in the LV which is followed by a more slowly increasing contrast agent concentration in the myocardium that reaches a much lower amplitude.

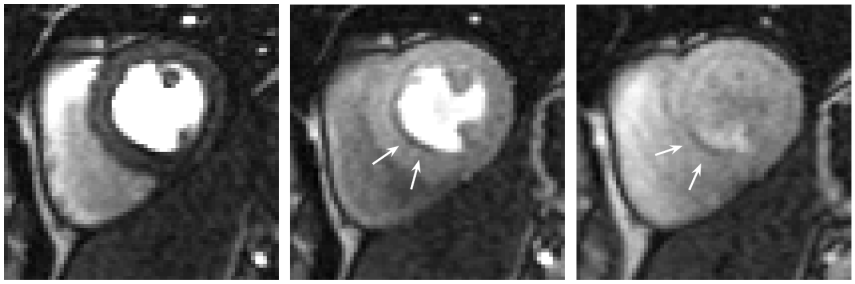

Figure 1.3: Selected images of a DCE series of a patient with subendocardial perfusion deficit. The corresponding hypo-enhanced area of the myocardium is marked with white arrows.

The precise relationship between T_1 and contrast agent concentration $[CA]$ in homogeneous tissue is given by the following equation [7]:

$$\frac{1}{T_1} = \frac{1}{T_{1,0}} + r_1 \cdot [CA], \tag{1.1}$$

where $T_{1,0}$ is the T_1 relaxation time constant in the absence of contrast agent and r_1 is the T_1 relaxivity constant of the contrast agent. r_1 depends on the specific contrast agent in use and decreases at higher magnetic field strengths [12]. Furthermore, studies show that the T_1 relaxivity is dependent on the temperature [13], the pH-value [14] and the macromolecular content of the region [15]. In all approaches focusing on quantification of myocardial perfusion from DCE-MRI, however, r_1 is assumed to be a constant that is unchanged when an extracellular contrast agent moves from the vascular into the interstitial space [7].

1.2.3 Myocardial DCE-MRI procedure

Acquisition of MR images for myocardial DCE-MRI should be fast because the heart contracts and dilates continuously on the one hand and concentrations of Gd-CAs change rapidly on the other hand (see Figure 1.2). Acquisition time per image or frame rate (T_{frame}) is therefore usually chosen shorter than 200 ms [11]. Moreover, as the same anatomical locations should be imaged during the passage of Gd-CA, consecutive images are acquired electrocardiogram-(ECG)-gated which limits the temporal resolution of the series of images to the duration of a heartbeat. Acquisition of more than one slice during each RR-interval allows to cover the myocardium (see Figure 1.4). Usually a basal, a mid-ventricular and an apical short-axis slice are acquired, which is supplemented by slices in long-axis orientation if the heart rate allows [8, 10, 11]. The heart moves not only by contraction and dilatation but also due to breathing maneuvers. This type of motion is commonly suppressed by breath-holding. As the time from contrast agent application to first and second pass of contrast agent is far too long for one breath-hold period,

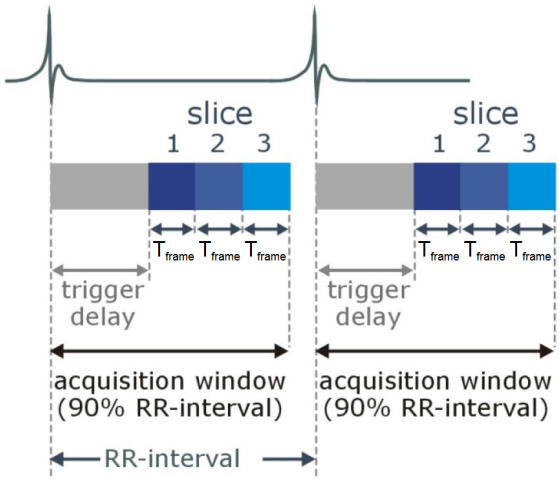

Figure 1.4: ECG-triggered acquisition of multiple slices during each RR-interval. Optionally a trigger delay can be used to restrict imaging to diastolic cardiac phases with less cardiac motion. Image modified from [11].

breath-holding is restricted to the first pass of CA through the LV and myocardium [10, 11].

1.2.4 Sequence technique for myocardial DCE-MRI

Myocardial DCE-MRI is most commonly accomplished using gradient echo (GRE) sequences [16]. Apart from allowing fast image acquisition, the sequence technique must also allow T_1-weighting to provide sufficient contrast between normally and hypo-perfused regions. This can be achieved by applying a non-slice-selective 90° saturation recovery (SR) preparation pulse and spoiling the transverse magnetization before each image acquisition [16]. As depicted in Figure 1.5, the longitudinal magnetization recovers faster for a myocardial region with high contrast agent concentration due to its shorter T_1 relaxation time. The time between saturation pulse and central k-space line of image readout (TI) determines the contrast between normally and poorly perfused myocardium, which is optimal where the two relaxation curves show the largest difference (case b in Figure 1.5). In practice, however, the chosen TI value is shorter than optimal (as in case a in Figure 1.5) to allow shorter frame rates [11].

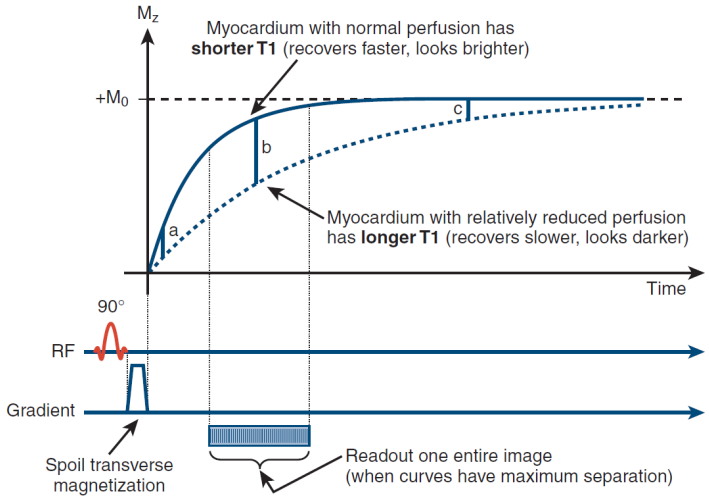

Figure 1.5: Longitudinal magnetization recovery in normally perfused (high $[CA]$) and hypo-perfused (low $[CA]$) myocardium after application of a saturation pulse. Image taken from [16].

Magnetization preparation is followed by a single-shot GRE readout sequence, typically either fast low-angle shot (FLASH) or steady-state free precession (SSFP). FLASH spoils the transverse magnetization that remains after data collection of each k-space line. SSFP, on the other hand, refocuses the remaining transverse magnetization, which has the effect that the remaining transverse magnetization is added to the newly excited magnetization of the next phase encoding step. Because of this re-use of the transverse magnetization, SSFP achieves at very short repetition times a higher signal-to-noise-ratio (SNR) than FLASH [17].

A typical problem encountered in myocardial DCE-MRI is the dark rim artifact. It appears as a dark band at the border between LV and myocardium after arrival of the contrast agent in the LV [18]. This artifact can be very disturbing because it may mimic hypo-perfusion in the subendocardial myocardium in visual analysis of a DCE series and has the potential to cause erroneous perfusion parameters in quantitative analysis. A way to distinguish the artifact from a real perfusion deficit is to visually inspect the appearance of the dark subendocardial line over time since only the artifact disappears after peak enhancement of the LV (see Figure 1.6). Other characteristics of the dark rim artifact are its most prominent appearance perpendicular to the direction of lowest resolution (typically the

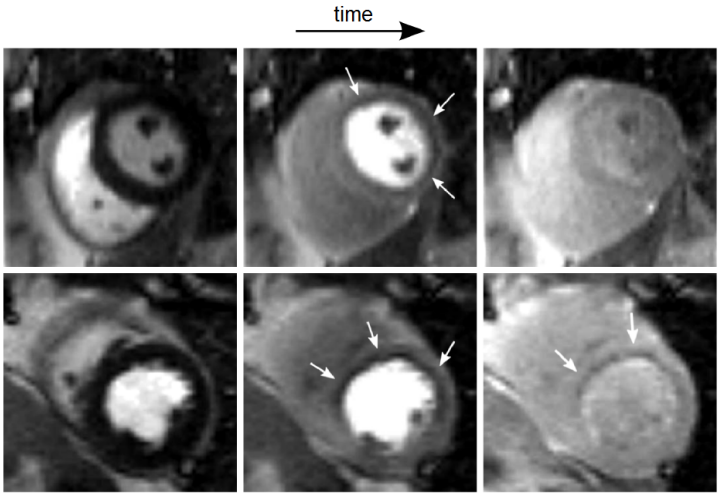

Figure 1.6: Comparison of a dark rim artifact (top) and a real subendocardial perfusion deficit (bottom) from two different patients. In contrast to the artifact, the real perfusion deficit persists also after contrast bolus arrival in the myocardium. Image taken from [8].

phase encoding direction) and a significant SI drop under the baseline of the myocardial region before contrast agent arrival [19]. The cause of the dark rim artifact is not yet fully understood. However, factors that may contribute to its occurrence include

- gadolinium-induced susceptibility effects, causing intra-voxel dephasing at the subendocardial border [18, 20],
- low resolution, causing Gibbs ringing adjacent to strong edges in the image [21], and
- cardiac motion [22].

Consequently, improving spatial and temporal resolution may lead to artifact reduction. In practice, this is optimized using parallel imaging [11]. Furthermore, it seems preferable to choose FLASH readout instead of SSFP since the latter is more prone to the appearance of the dark rim artifact [17, 23].

Two further aspects of DCE-MRI sequences possibly causing signal intensity variations across the heart not related to contrast agent enhancing tissue should be mentioned: B_1 inhomogeneity effects and inhomogeneous receive coil sensitivities across the heart.
In general, B_1 inhomogeneity or inhomogeneous radio frequency (RF) excitation may

become a noticeable issue if the wavelengths of the RF excitation in tissue reach body dimensions and dielectric properties of the imaged anatomical region are highly heterogeneous. As wavelengths decrease with higher magnetic field strengths, relevance of the problem increases with field strength. B_1 inhomogeneities cause inhomogeneous flip angles and flip angle variations over the LV in mid-ventricular short-axis orientation of up to almost 50% at 3T were reported [24]. Flip angle variations for myocardial DCE-MRI sequences may cause inhomogeneous signal either via the readout sequence or via the saturation recovery preparation, the latter being considered as more relevant [7, 25]. Common solutions to optimize inhomogeneous saturation are the utilization of adiabatic or composite saturation pulses, where both variants were shown to achieve satisfactory results [26].

As the MR signal is received with phased-array receive coils, spatial inhomogeneous signal intensities across the heart might also result from inhomogeneous surface coil sensitivity. Whereas different procedures have been suggested to correct these inhomogeneities in myocardial DCE-MRI, the most common approach is based on the acquisition of proton density images prior to DCE-MRI measurements, using these images for estimation of coil sensitivity and finally applying these estimates for signal correction in DCE-MRI frames [27]. Current DCE-MRI sequence implementations include such proton-density acquisitions as the first 1-2 images in the dynamic imaging scan, by leaving out the magnetization preparation and using small flip angle acquisitions with all other parameters unchanged for the image readout; the coil sensitivity correction based on the resulting proton density images is performed during image reconstruction [7, 28].

1.2.5 Relationship between signal intensity and contrast agent concentration

Signal intensities of SR-prepared gradient echo sequences depend non-linearly on contrast agent concentration, with deviations from linearity towards signal saturation becoming more distinct at higher concentrations [29]. This signal saturation effect would ultimately

even lead to a decreasing signal intensity above a certain $[CA]$-level due to T_2^* effects [30]. Notably, the increase of contrast agent concentration in the myocardium depends, apart from myocardial perfusion, on the arterial input of contrast agent. Consequently, approaches of myocardial perfusion analysis beyond the scope of visual analysis will typically have to consider the relationships between signal intensity in SR-prepared gradient echo sequences and contrast agent concentration in myocardium and the LV blood pool, which is usually considered the arterial input to myocardium due to its close vicinity to the myocardium and its visibility on DCE images. As during the first pass contrast agent concentration is higher in the LV blood pool compared to myocardium, signal saturation effects are more prominent in the LV blood pool [7]. Different approaches have been suggested and applied to facilitate the interpretation and recalculation of signal intensity changes in terms of contrast agent concentration changes.

The simplest approach to solve the signal saturation problem is to apply low contrast agent dosages ($\leq$ 0.025mmol/kg body weight [31]) exploiting the almost linear dependency of SI on $[CA]$ at resulting concentration levels. However, using a low contrast agent dosage leads to a low contrast-to-noise-ratio (CNR), especially in the myocardium. In order to avoid the problem of low myocardial CNR while keeping almost linear dependency of SI on $[CA]$, two methods have been proposed to perform myocardial DCE-MRI at recommended CA doses of 0.05-0.1 mmol/kg for visual perfusion analysis [10]. The dual bolus technique [32] applies first a low-dosed bolus to stay in the linear range for the LV. In a second measurement, a higher-dosed bolus is administered to maximize the CNR in the myocardium. The dual sequence approach [33], on the other hand, applies one high-dose bolus and combines a low-resolution image acquisition with short TI for LV blood pool assessment (exploiting the short TI to stay in the linear range for the CA bolus in the LV) with high-resolution imaging with longer TI for the assessment of the myocardial enhancement.

A more measurement-independent solution to the problem of transforming signal intensities into concentrations is the recalculation based on either T_1 phantom calibration curves [30] or signal intensity models for the DCE-MRI sequence [34, 35]. In greater detail, for retrospective SI to $[CA]$ conversion it is sufficient to find the T_1 values corresponding to the measured SI values [34] since the contrast agent concentration can be determined from

T_1 using Equation (1.1) provided the pre-contrast $T_{1,0}$ of the enhancing tissue is known. The relationship between SI and T_1 can be written as [34]:

$$SI = \Psi f(T_1), \tag{1.2}$$

where Ψ denotes a scaling coefficient that depends on factors like system gain, receive coil sensitivity or localization of the tissue and $f(T_1)$ is a function depending on the DCE-MRI sequence [34]. Ψ can be estimated using the baseline signal S_0 and the pre-contrast $T_{1,0}$ value of the investigated region [34]. $T_{1,0}$ of LV blood pool and myocardium can be measured from a T_1 map acquired previous to DCE-MRI.

1.3 Perfusion quantification from myocardial DCE-MRI

Apart from purely visual analysis of myocardial DCE-MRI series it is possible to derive quantitative parameters related to myocardial perfusion, which might allow deeper insights into physiology and pathophysiology of myocardial perfusion and enlarge diagnostic capabilities [4, 7, 36]. Within the quantification approaches one subdivides into semi-quantitative analysis, where one aims to derive suitable SI time curve parameters which should be related to myocardial perfusion, and quantitative analysis, where one tries to quantify myocardial perfusion.

In principle, the analysis can be performed either region of interest (ROI) based or pixel-wise. Even though first passage of contrast agent through LV and myocardium is typically imaged under breath-hold, anatomical structures tend to move, which nevertheless necessitates motion correction for the derivation of sensible SI time curves and renders pixel-wise evaluation difficult. However, different motion correction algorithms for myocardial DCE-MRI series have been developed [37] and approaches for pixel-wise perfusion quantification have shown promising results [38, 39].

1.3.1 Semi-quantitative analysis

In semi-quantitative perfusion analysis from myocardial DCE-MRI series, a set of parameters is calculated that characterizes the SI time curves resulting from the first passage of contrast agent through the myocardium. Those parameters are expected to vary if myocardial perfusion is altered. As myocardial perfusion depends on the arterial input as well, the myocardial curve parameters are – for comparative reasons - frequently normalized to corresponding parameters of the arterial input function (AIF) which is an arterial SI time curve typically gained from the LV blood pool. The most common semi-quantitative parameters are (see Figure 1.7):

- Signal intensity maximum (SIM): Maximum value of the SI time curve relative to the baseline signal.
- Up-slope (US): The maximum slope of the SI time curve during the early phase of contrast agent passage through the myocardium. The up-slope of the myocardial SI time curve is usually normalized by the up-slope of the LV as measure of speed and compactness of the contrast agent bolus [40].
- Time-to-peak (TTP): The time from contrast agent arrival until the peak signal intensity is reached.
- Area under the curve (AUC): Area under the SI time curve from contrast agent arrival to the time point of maximal SI.
- Myocardial perfusion reserve index (MPRI): The ratio of the normalized myocardial up-slope at stress and at rest [41].

The expected advantage of a theoretically simple calculation of these parameters is in practice confronted with the problem of disruptive changes in the SI time curve due to noise and artifacts. This may result in an incorrect computation of for example the baseline, the point of contrast agent arrival or the up-slope, which in turn would lead to an erroneous estimation of subsequently calculated parameters [37].

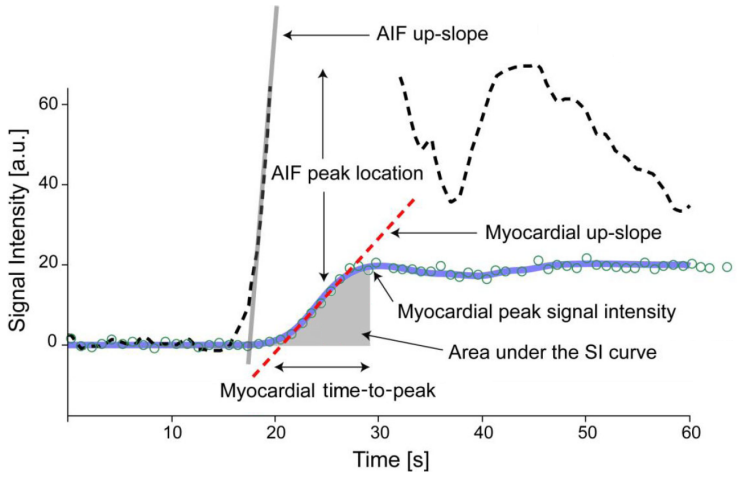

Figure 1.7: Typical semi-quantitative parameters describing the SI time curves extracted from LV (denoted AIF) and myocardium. Image modified from [7].

1.3.2 Quantitative analysis

Quantification of myocardial perfusion from myocardial DCE series is usually based on a system theory motivated convolutional relationship between the contrast agent concentration in the arterial input and the contrast agent concentration in tissue. To motivate this relationship the circulatory system of a tissue might be considered as a black box with only one arterial inlet and one venous outlet [43] (see Figure 1.8 (a)). Applying the principle of mass balance yields that the contrast agent concentration in the myocardial capillary-tissue system (the black box) at any time, $c_{tissue}(t)$, is equal to the difference of the contrast agent concentrations washed into and out of the system, multiplied by the myocardial perfusion, or synonymously, myocardial blood flow (MBF) [44]:

$$c_{tissue}(t) = MBF \cdot sg \cdot \int_0^t [c_{AIF}(\tau) - c_{out}(\tau)]\, d\tau, \tag{1.3}$$

where sg denotes the specific gravity of myocardial tissue ($sg = 1.05 g/ml$ [45]) and c_{AIF} and c_{out} denote the contrast agent concentrations at inlet and outlet specified in units of $mmol/ml$, respectively; c_{tissue} is specified in units of $mmol/ml$ of tissue and MBF in units of $ml \cdot min^{-1} \cdot g^{-1}$. If the transport processes in the tissue system are assumed to be

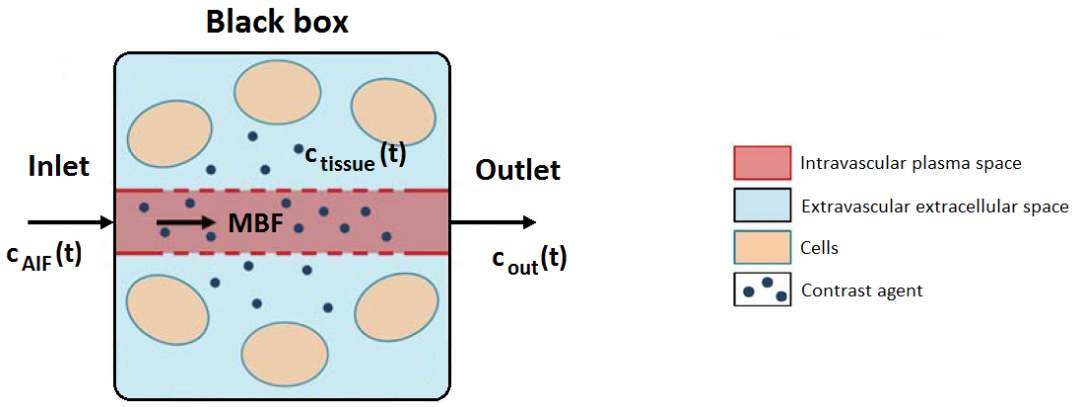

(a)

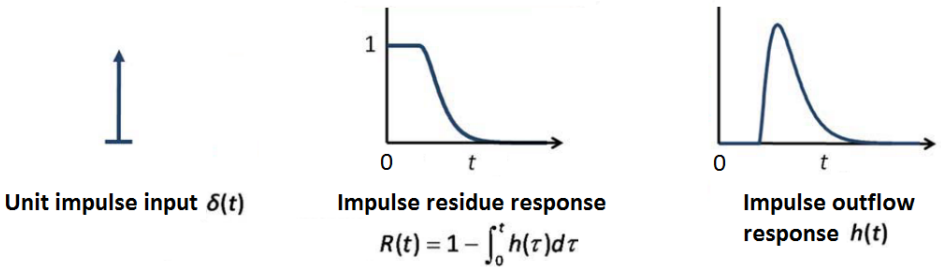

(b)

Figure 1.8: Schematic myocardial capillary-tissue system as a black box characterized by its impulse response functions. The extracellular contrast agent, supplied by a constant myocardial blood flow (MBF), enters the system through the inlet and moves between intravascular plasma space and extravascular extracellular space, but does not enter cells (a). The contrast agent concentrations washed into and out of the system are denoted $c_{AIF}(t)$ and $c_{out}(t)$, respectively; the contrast agent concentration inside the black box is represented by $c_{tissue}(t)$. If $c_{AIF}(t)$ is assumed to be an impulse input $\delta(t)$, the impulse outflow response $h(t)$ describes the probability that a contrast agent molecule has left the system at time t (b). The impulse residue response $R(t)$, on the other hand, describes the probability that a contrast agent molecule remains in the tissue system at time t. Images modified from [42].

linear and time-invariant, $c_{out}(t)$ can be calculated as the convolution of $c_{AIF}(t)$ with the transfer function of the system, $h(t)$ [31]:

$$c_{out}(t) = \int_0^t c_{AIF}(\tau)h(t-\tau)d\tau = c_{AIF}(t) * h(t). \tag{1.4}$$

The transfer function $h(t)$ can be interpreted as the probability density function of transit times through the system [43]. Hence, it gives the probability that a contrast agent molecule has left the system at time t if $c_{AIF}(t)$ is assumed to be a Dirac delta impulse ($\delta(t) = 1$ if $t = 0$, $\delta(t) = 0$ if $t \neq 0$). As shown in Figure 1.8 (b), $h(t)$ is equal to zero at $t = 0$ since the contrast agent cannot instantly pass from inlet to outlet. The probability that a contrast agent molecule remains in the tissue system at time t, $R(t)$, can be calculated as:

$$R(t) = 1 - \int_0^t h(\tau)d\tau. \tag{1.5}$$

$R(t)$ is called the impulse response function of the system. Using Equations (1.4) and (1.5), Equation (1.3) can be rewritten to:

$$c_{tissue}(t) = MBF \cdot sg \cdot \int_0^t c_{AIF}(\tau)R(t-\tau)d\tau = c_{AIF}(t) * R_F(t) \tag{1.6}$$

where $R_F(t) = MBF \cdot sg \cdot R(t)$ represents the myocardial perfusion-weighted impulse response function of the system. That means the contrast agent concentration $c_{tissue}(t)$ in the myocardium is a result of the convolution of the contrast agent concentration $c_{AIF}(t)$ at inlet and the myocardial perfusion-weighted impulse response function $R_F(t)$ of the system. Figure 1.9 illustrates this relationship.

From Equation (1.5) it can be seen that $R(t)$ is a positive function with initial value equal to one, ($R(0) = 1$). Consequently, myocardial perfusion can be derived from the myocardial perfusion-weighted impulse response function at $t = 0$:

$$MBF = \frac{R_F(0)}{sg}. \tag{1.7}$$

Equations (1.6) and (1.7) form the basis of myocardial perfusion quantification from myocardial DCE-MRI. MBF in a tissue region can be quantified if the concentration of contrast agent in the myocardial tissue ($c_{tissue}(t)$) and in the LV ($c_{AIF}(t)$) can be determined,

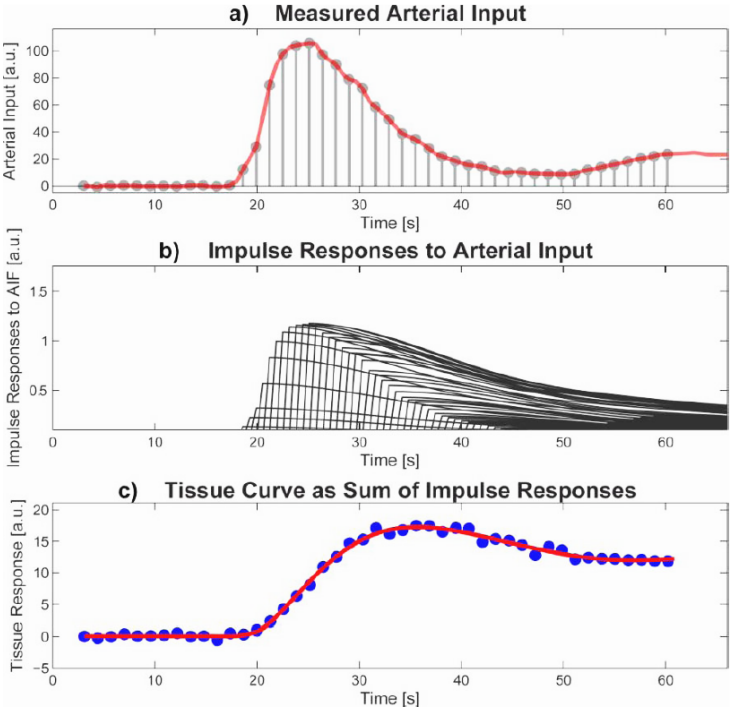

Figure 1.9: Illustration of the convolution operation using a general arterial input. a) The measured arterial input curve can be represented as a train of Delta impulses with a uniform time interval Δt and different amplitudes. b) When entering the tissue system, each of the Delta impulses produces an impulse response. The impulse response is characteristic of the system, so all the impulse responses to the input train are the same, just that they are shifted in time and scaled depending on the amplitude of the corresponding Delta impulse. c) The tissue curve is the result of summing up all the time-shifted and differently scaled impulse responses from b. This operation is equivalent the convolution operation in Equation (1.6). Image taken from [7].

assuming that the contrast agent concentration at inlet is adequately described by the one in the LV. Hence, the first step is to deduce $[CA]$ from the measured SI (see Section 1.2.5). Then, one can approach to calculate $R_F(t)$ by deconvolving $c_{tissue}(t)$ and $c_{AIF}(t)$ and determine the MBF from its initial (or maximal) value.

Deconvolution analysis for the determination of perfusion-related parameters can be divided into model-based and model-independent methods. Model-based approaches describe the myocardial perfusion-weighted impulse response function $R_F(t)$ with a model function whose parameters are to be determined in a model-fitting process that satisfies Equation (1.6). Several model-based methods exist that make assumptions about the structure and processes inside the myocardial black box, for example by dividing the circulatory system of the myocardial tissue into functional compartments and describing how contrast agent concentrations in the compartments change as contrast agent molecules move between them [46]. However, those methods simplify the myocardial circulatory system to a high degree [7] and vulnerable assumptions are required to derive the mathematical description of contrast agent transport processes [43]. To avoid those problems, other model-based approaches do not explicitly investigate processes inside the black box, but rather determine the impulse response function by specifying features like its shape or a certain relation between the contrast agent concentration at the inlet and inside the system.

Model-independent methods determine the impulse response by inversion of Equation (1.6) in the time or Fourier domain without assuming a certain functional form of the impulse response. This numerical deconvolution is considered an 'ill-posed' problem because there is no unique solution for $R_F(t)$ and small errors in the measured data can cause large perturbations in the solution [47]. Therefore, the deconvolution can yield a mathematically correct solution that yet makes no sense physiologically. Solving the deconvolution problem can be approached by looking for an approximate solution that fulfills physiologically meaningful side constraints. This means that prior knowledge about the solution $R_F(t)$ has to be included in the calculation process. According to Jerosch et al., $R(t)$ must be a monotonically decaying function because after an initial Dirac delta input the contrast

agent is washed out of the tissue system if there is no replenishment [47]. Additionally, smoothness constraints can be added since for $t > 0$ no sudden jumps are expected in the impulse response [7].

Deconvolution approaches commonly applied for the determination of myocardial perfusion from DCE-MRI series are

- Fermi function modeling,
- Tikhonov regularization with B-splines and
- ARMA modeling.

The first method is a model-fitting approach that constrains the impulse response to take the shape of a Fermi function [31]. In the second method, the MBF is determined by model-independent deconvolution. The impulse response is parametrized as a sum of B-splines and the deconvolution is solved applying Tikhonov regularization [47]. The autoregressive moving average (ARMA) approach is a linear algebraic technique that assumes a linear differential relation between AIF and myocardial tissue curve [48]. All three deconvolution methods will be described in detail in Chapter 2.

1.4 Aim of the thesis

Due to the lack of suitable motion correction algorithms, determination of quantitative myocardial perfusion parameters has been limited to region-based analysis for a long time. However, pixel-wise evaluation of myocardial perfusion parameters has the potential to provide additional information about location and extent of perfusion deficits compared to ROI-based evaluation or visual analysis of DCE-MRI series. Studies have shown that pixel-wise determination of absolute myocardial perfusion in DCE-MRI data of patients is feasible [39, 49, 50]. Moreover, for pixel-wise semi-quantitative analysis, automated frameworks exist that include steps like image registration, denoising and semi-quantitative pa-

rameter map generation [51–53]. However, the relationships of pixel-wise semi-quantitative and quantitative myocardial perfusion analysis need to be evaluated, especially when employing standard clinical imaging procedures and contrast agent dosages.

The aim of this thesis was to develop algorithms and prototype software for the pixel-wise determination of

- SI-based semi-quantitative myocardial perfusion parameters,
- concentration-based semi-quantitative myocardial perfusion parameters, and
- quantitative myocardial perfusion by three different deconvolution approaches (Fermi modeling, Tikhonov regularization with B-splines, ARMA modeling)

from motion-corrected myocardial DCE-MRI data and to compare the results for resting perfusion studies in patients with coronary heart disease.

2 Methods

2.1 Study population

Cardiac MRI data sets of eleven patients with chronic coronary heart disease were evaluated in this thesis. All data sets were acquired within the explorative study "Cardiac blood flow patterns associated with regional and global left ventricular myocardial damage: an explorative study by cardiac magnetic resonance" (EK-Nr. 25-096 ex 12/13) approved by the local review board. All subjects gave written informed consent.
Data of three patients were excluded from comparative analysis of myocardial perfusion parameters because of limited data quality (explained in more detail in the Discussion section). Characteristics of the comparatively studied population of the remaining eight patients (two female) were age = 65 ± 8 years, height = 172 ± 8 cm, weight = 83 ± 13 kg, and heart rate = 68 ± 11 min^{-1}.

2.2 MRI acquisition

Cardiac MRI acquisition was performed on a 3 T clinical MR scanner (Magnetom Skyra, Siemens Healthcare, Erlangen, Germany) using a 18-channel body coil and 12 elements of a 32-channel spine coil. Native T_1 mapping and myocardial DCE-MRI under resting conditions were performed within a comprehensive cardiac imaging protocol.

An ECG-gated modified Look-Locker inversion recovery (MOLLI) sequence with single-shot SSFP readout, motion correction and automatic T_1 map generation [54, 55] was used to acquire a mid-ventricular short-axis myocardial T_1 map in end-systole. The MOLLI scheme consisted of the acquisition of a total of eight images. Five images were acquired after an initial non-slice selective inversion pulse at an inversion time of TI = 90 ms to 4×RR + 90 ms, with RR denoting the cardiac interval. After a recovery phase of five heartbeats, three further images were measured after a second non-slice selective inversion pulse at TI = 170 ms to 2×RR + 170 ms. Protocol parameters of the SSFP readout were repetition time TR = 2.7 ms, echo time TE = 1.1 ms, flip angle = 35°, bandwidth = 1085 Hz/pixel, field of view FOV = 307×360 mm^2, voxel size = 2.1×1.4×8.0 mm^3. GRAPPA (generalized auto-calibrating partially parallel acquisition) with a parallel acquisition factor of 2 and the separate measurement of gradient echo reference lines as well as partial Fourier 7/8 reconstruction were employed to minimize acquisition time within each cardiac interval.

Myocardial DCE-MRI was performed with the contrast agent Gadobutrol (Gadovist, Bayer Schering Pharma, Germany) at a dose of 0.05 mmol/kg. The contrast agent was administered into the right antecubital vein by means of a power injector (Medrad, Volkach, Germany) at a rate of 4 ml/s, followed by a saline flush of 30 ml. Starting with contrast agent administration its passage was imaged employing an ECG-gated single-shot SR FLASH sequence in short-axis orientation for 70 heart beats; a breath-hold command given during acquisition targeted a breath-hold period from the arrival of the bolus in the left ventricle until its second pass.

The frame rate of the employed SR FLASH sequence was T_{frame} = 158.8 ms allowing to image four to six slices per heart beat. Further protocol parameters were repetition time TR = 2.2 ms, echo time TE = 1.1 ms, time between saturation and central k-space line of image readout TI = 90 ms, flip angle = 12°, bandwidth = 930 Hz/pixel, field of view FOV = 330×360 mm^2, voxel size = 2.7×1.9×8.0 mm^3, matrix = 124×192, GRAPPA with a parallel acquisition factor of 2 and separate measurement of gradient echo reference lines. For B_1-insensitive saturation a composite saturation pulse consisting of

three consecutive radio frequency pulses and crusher gradients was employed [26]. Images of the myocardial DCE-MRI scan within the first two heart beats were acquired without applying magnetization preparation at a low flip angle of 5°. The resulting (pre-contrast) proton density weighted images were used to estimate the coil sensitivity of the receiver coils. This estimation, together with a surface coil correction as well as a non-rigid motion correction of every frame, was performed automatically during image reconstruction [52]. The resulting coil sensitivity-corrected and motion-corrected mid-ventricular short-axis DCE series whose slice position coincided with the T_1 map was used for myocardial perfusion analysis.

2.3 Overview of the data processing pipeline

Figure 2.1 illustrates the data processing pipeline for the determination of pixel-wise semi-quantitative and quantitative myocardial perfusion parameter maps from a motion and coil sensitivity corrected short-axis DCE-MRI series of the heart. The pipeline was implemented in Matlab (Mathworks Inc., Natick, USA) and computations were performed on a notebook Acer Aspire VN7-592G-79U3 (Acer Group, Taipeh, Taiwan).

Preprocessing of the given data can be divided into:

- Automated heart bounding box extraction
- Selection of a ROI in the LV
- SI to $[CA]$ conversion
- Specific steps for quantitative analysis:
  - Manual segmentation of the myocardium
  - Resampling of the $[CA]$ time curves
  - Motion correction quality map and outlier detection

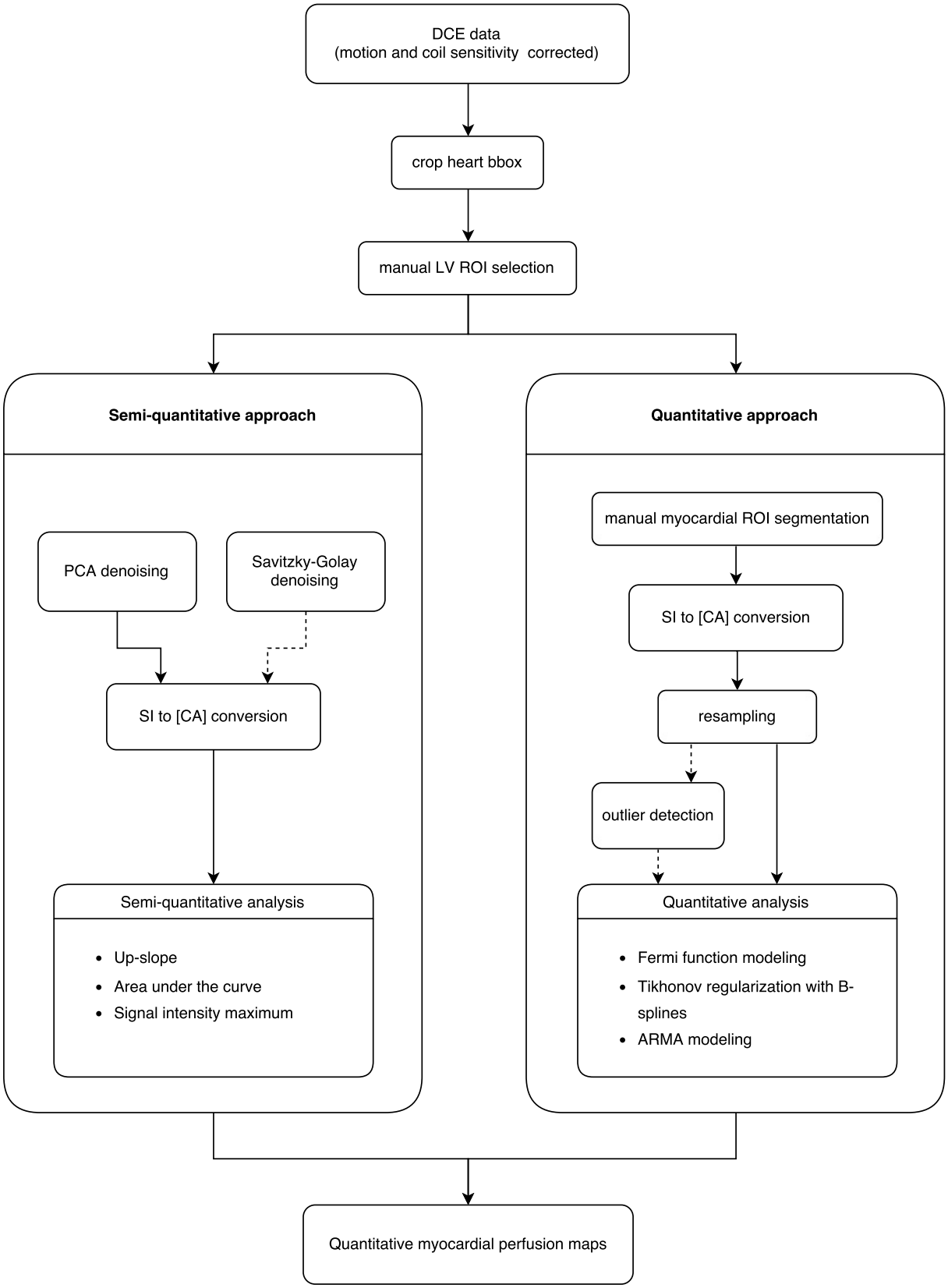

Figure 2.1: Data processing pipeline for determination of semi-quantitative and quantitative perfusion parameters and generation of quantitative myocardial perfusion maps.

- Specific step for semi-quantitative analysis: denoising with a
    1. Principal component analysis (PCA) filter or
    2. Savitzky-Golay filter

Preprocessing is followed by a pixel-wise calculation of perfusion-related parameters. In semi-quantitative analysis, whole-heart parameter maps are calculated for both $[CA]$ and SI data. In quantitative analysis, parameters can sensibly only be calculated for a myocardial ROI using $[CA]$ time curves.

2.4 Preprocessing

2.4.1 Automated heart bounding box extraction

As a first step of preprocessing, the heart is automatically selected and extracted from the thoracic images as the region of interest. This is done by exploiting the fact that the right and left ventricle are the largest (substantially) enhancing areas in the image series. The main reason for cropping the images is the reduction of computation time when functions are applied on all pixels in the image, as done when calculating semi-quantitative parameter maps.

Implementation: First of all, a temporal maximum intensity projection (MIP) and a temporal minimum intensity projection (mIP) are calculated for every pixel, as suggested by Hautvast et al. [56]:

$$MIP_{x,y} = \max_t \{\mathbb{I}_{x,y,t}\} \tag{2.1}$$

$$mIP_{x,y} = \min_t \{\mathbb{I}_{x,y,t}\}, \tag{2.2}$$

where $\mathbb{I}_{x,y,t}$ is the signal intensity at position (x,y) over time t. The mIP map gets subtracted from the MIP map in order to black out bright regions that do not change their SI over time, as for example fat tissue. The result is a difference image (I_{diff}) as shown in Figure 2.2 (a).

(a) (b) (c) (d)

Figure 2.2: Image processing steps for the extraction of a ROI containing the heart. a) Difference image of MIP and mIP maps, b) binary image after applying a threshold, c) merged ventricles as the biggest connected component resulting from morphological 'opening' and 'closing' and d) bounding box containing the heart.

As a next step, all pixels inside a 30 pixel distance from each border of the difference image are set to zero to exclude perturbing bright artifacts and facilitate the heart detection. Since now the heart should be brightest area in the difference image, a threshold of $thr = 0.4 \cdot max\{I_{diff}\}$ is applied, which yields a binary image as in Figure 2.2 (b). Then, the morphological operations 'opening' and 'closing' are applied using the functions `imopen` and `imclose`, respectively. The 'opening' is done using a small diamond-shaped structuring element (radius $r = 3$ pixels) to remove noise and small objects. For the 'closing' a large diamond-shaped structuring element ($r = 11$ pixels) is applied to merge both ventricles (see Figure 2.2 (c)). The last step is identifying the largest connected component in the binary image using the function `bwconncomp` and generating a rectangular bounding box in a certain distance to the border pixels to the object (15 pixels in the directions north, east, south and 10 pixels in western direction). Figure 2.2 (d) shows the obtained heart bounding box in red. At these coordinates the image series gets cropped to speed up further analysis.

As imaging was started with contrast agent application and in the first images of the DCE series steady state is not fully reached, from this point on, the first ten images of the cropped image series are not loaded and used for analysis. There are enough baseline signal measurement points before contrast agent arrival in the LV anyhow, while computation time of point-wise operations can be further reduced.

2.4.2 Segmentation

The ROI in the LV, which will be used to determine the AIF, is drawn by the user in an image with good contrast between left-ventricular blood pool and myocardium. The selection of this image from the DCE series is not critical because of the prominent appearance of the left-ventricular blood pool throughout all first pass images.
Intuitively, the same approach could also be used for the segmentation of the myocardium [57, 58]. However, looking for an image which exhibits a good contrast between myocardium and its surrounding structures is more time consuming than for the LV and also highly user-dependent. Consequently, the signal intensity maximum (SIM) map is chosen as base image for segmentation of the myocardium (see comparison in Figure 2.3).

Implementation: The function `roipoly` is used for both selection of a ROI in the LV as well as segmentation of the myocardium. The user is asked to draw the borders in a way that pixels exhibiting partial volume effects are excluded. For a description of the calculation of the SIM map the reader is referred to Section 2.5.1.

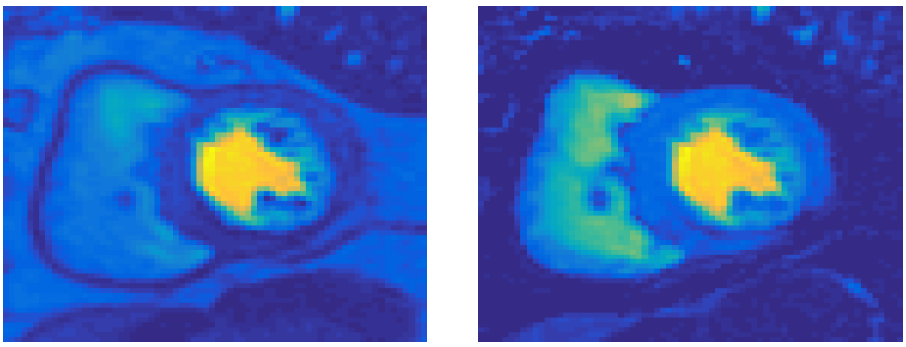

(a) (b)

Figure 2.3: Comparison of an image of the DCE series with good contrast (a) and the corresponding signal intensity maximum map (b). The region of the myocardium as well as its borders are better distinguishable in the signal intensity maximum map.

2.4.3 Signal intensity to concentration conversion

The conversion from SI to $[CA]$ is done using a signal intensity model for the employed DCE-MRI sequence. For a saturation recovery FLASH sequence with linear ordering of phase-encodings the signal intensity after half of all phase encoding steps (when reaching the k-space center) is given by [31, 59]:

$$SI = \Psi \left[\left(1 - e^{-TD \cdot R_1}\right) \cdot \left(e^{-R_1 \cdot T_R} \cdot \cos(\alpha)\right)^{n-1} + \left(1 - e^{-R_1 \cdot T_R}\right) \cdot \frac{1 - \left(e^{-R_1 \cdot T_R} \cdot \cos(\alpha)\right)^{n-1}}{1 - e^{-R_1 \cdot T_R} \cdot \cos(\alpha)} \right], \quad (2.3)$$

where Ψ is a scaling factor proportional to the equilibrium magnetization, TD the time delay between the 90° pulse and the start of FLASH readout, R_1 the T_1 relaxation rate, T_R the repetition time per phase encoding, α the flip angle and n the number of phase encodings between acquisition start and k-space center. TD is related to the time TI between saturation pulse and central k-space line of image readout according to:

$$TD = TI - n \cdot T_R. \quad (2.4)$$

Ψ can be estimated from the baseline signal S_0 and the pre-contrast $T_{1,0}$ determined from a T_1 map the according to [34]:

$$\Psi = \frac{S_0}{f(T_{1,0})}. \quad (2.5)$$

After calculating Ψ, the T_1 values for each time frame of the DCE series are determined with Equation (2.3) and then inserted into Equation (1.1) to calculate the corresponding $[CA]$ values.

Implementation: The AIF is determined as the mean SI curve of all pixels in the LV ROI. The baseline signal S_0 of each pixel is then estimated as the mean value of the SI values measured before contrast agent arrival in the LV, meaning from $t = 0$ up to the minimum point of the AIF. For a description of the minimum point detection the reader is referred to Section 2.5.1.1. In order to estimate $T_{1,0}$ of LV blood pool and myocardium, the user is asked to draw with `roipoly` two respective ROIs in the T_1 map acquired with

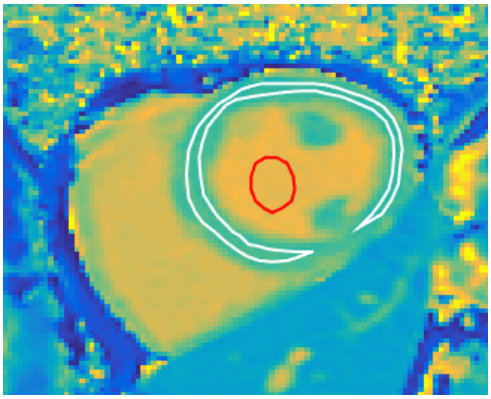

Figure 2.4: Exemplary T_1 map with ROIs in myocardium (white) and LV blood pool (red).

the MOLLI sequence (see example in Figure 2.4). The $T_{1,0}$ values are calculated as the mean values of all pixels in each ROI. Then, Ψ is estimated by inserting S_0 and $T_{1,0}$ into Equation (2.5). For calculating T_1 values from SI values the zero-finding algorithm `fzero` is used, which requires rearranging Equation (2.3) to:

$$0 = f(T_1) - \frac{SI}{\Psi} \tag{2.6}$$

and using the protocol parameters $T_R = 2.2ms$, $TI = 90ms$, $\alpha = 12°$, $n = 31$ as well as $TD = 21.18ms$ according to Equation (2.4). Finally, the $[CA]$ values for every time point are determined by inserting the T_1 values into Equation (1.1) in the form:

$$[CA] = \frac{1}{r_1}\left(\frac{1}{T_1} - \frac{1}{T_{1,0}}\right), \tag{2.7}$$

where $r_1 = 5.0l/mmol \cdot s$ for Gadovist in plasma at 37° at 3T [12].

2.4.4 Resampling for uniform time spacing

The ECG-gated image acquisition naturally leads to a non-uniform time spacing between the images of the measured DCE series. This non-uniform temporal sampling is even more pronounced for patients with arrhythmia or in case single ECG-triggers are missed. Since the deconvolution approach requires signals with uniform time spacing, the $[CA]$ time curves are resampled using monotonic piecewise cubic interpolation [60], as suggested by

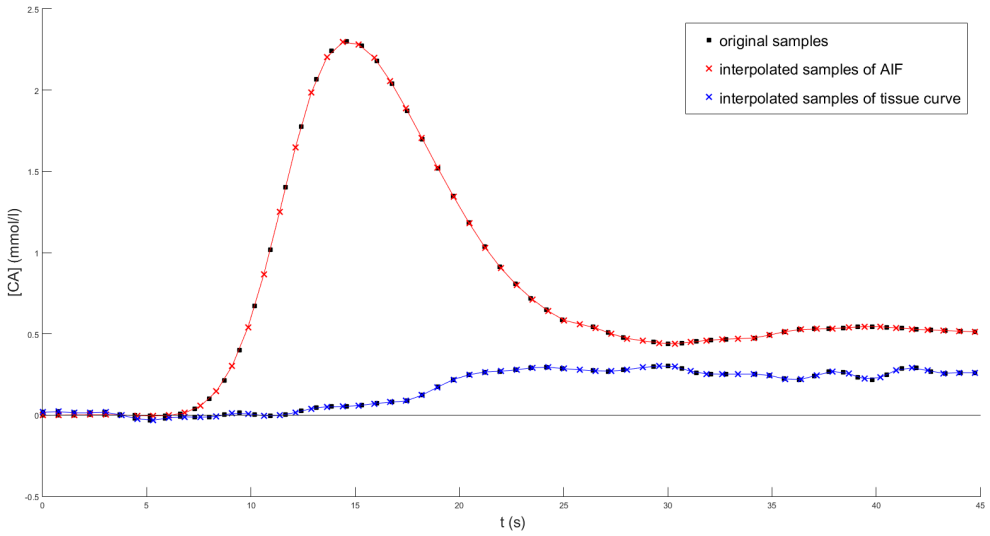

Figure 2.5: Example of resampling myocardial and left-ventricular $[CA]$ time curve using `pchip`.

Biglands et al. [57]. The sampling rate of the resulting uniformly sampled $[CA]$ time curves is chosen equal to the average heart rate of the respective patient [61].

Implementation: The time stamps of the DCE image frames are read out from the respective DICOM file of each patient. Then, the function `pchip` (Piecewise Cubic Hermite Interpolating Polynomial) is used for interpolation. This method has the advantage of preserving the shape of the data, meaning that in the interpolated time curve there are no oscillations between data points and extreme values stay the same. Figure 2.5 shows an example of myocardial and left-ventricular $[CA]$ time curves resampled with `pchip`. The number of sampling points stays the same, but after interpolation they are uniformly spaced.

2.4.5 Motion correction quality map and outlier detection

Quantitative perfusion analysis relies on the assumption that AIF and myocardial $[CA]$ time curve used for deconvolution are not distorted by artifacts or imperfect motion correction. Unfortunately, pixel-wise analysis is especially vulnerable to those non-physiological

deformations of the myocardial $[CA]$ time curves. Therefore, a motion correction quality map is generated which gives a measure of how much the shape of the $[CA]$ time curve of each pixel deviates from the expected shape of a myocardial signal curve. This is done by fitting a sigmoid function to the $[CA]$ time curve in the least squares sense and calculating a normalized squared L^2-norm of the residual. In order to detect heavily distorted $[CA]$ time curves and to exclude these outliers from quantitative analysis, an upper threshold depending on the quality values in the myocardial ROI is set.

Implementation: First of all, SI to $[CA]$ conversion and resampling with `pchip` is done as described above for every investigated pixel. A pixel is thereby treated as a LV pixel if the maximum of its SI time curve is $\geq 50\%$ of the maximum of the AIF. `lsqnonlin` with its default 'trust-region-reflective' algorithm is used to fit the following function to every $[CA]$ time curve:

$$f(t) = \frac{a}{1 + e^{-b(t-c)}}, \tag{2.8}$$

where a, b and c are the shape parameters to be determined. The initial values are set so that a equals the maximum value of the SIM map in the myocardial ROI (see Section 2.5.1), $b = 1$ and c is equal to one third of the temporal duration of the whole curve. In order to treat background pixels correctly, boundary constraints are included in the fitting process. The lower boundaries of a, b and c are chosen as the minimum value of the SIM map in the myocardial ROI, zero and the 10^{th} time point, respectively. The only upper boundary set is c equal to the 10^{th} last time point of the $[CA]$ time curve. `lsqnonlin` returns the fitting parameters a, b and c as well as $resnorm$, the squared L^2-norm of the residual. The motion correction quality map is generated by normalizing $resnorm$ of each pixel by the maximum amplitude of the fitted curve of the respective pixel.
Outlier detection is performed by calculating the median of the quality map values in the myocardial ROI and applying the threshold $thr = 2 \cdot median$. All quality values higher than this threshold are identified as outliers and the corresponding pixels of the myocardial ROI are excluded from deconvolution analysis.

2.4.6 Denoising for semi-quantitative analysis

Disruptive changes in the SI or $[CA]$ time curves can have a significant influence on the results of semi-quantitative analysis, especially in the pixel-wise approach. Therefore, denoising is a crucial preprocessing step. In this thesis, two denoising methods are discussed and compared, namely automated PCA filtering and application of a Savitzky-Golay filter.

2.4.6.1 Automated principal component analysis filtering

Principal component analysis (PCA)[1] transforms a data set of interrelated variables to a set of uncorrelated variables which are called principal components. These components describe the variation present in all the variables of the input data and are ordered in a descending way, with the first component corresponding to the maximum variation [62]. When PCA is applied on DCE data, meaning on the temporal SI changes in individual pixels of a ROI, the number of principal components m is equal to the number of image frames of the series.

In this thesis, the singular value decomposition (SVD) is chosen for PCA calculation since it is computationally efficient in determining the principal components [62]. The SVD of a real $m \times n$ matrix A, where $m \geq n$, is defined as follows [63, 64]:

$$A = U\Sigma V^T = \sum_{i=1}^{n} \mathbf{u}_i \sigma_i \mathbf{v}_i^T, \tag{2.9}$$

$$U = (\mathbf{u}_1, ..., \mathbf{u}_n) \in \mathbb{R}^{m \times n}, \quad V = (\mathbf{v}_1, ..., \mathbf{v}_n) \in \mathbb{R}^{n \times n} \quad \text{and} \quad \Sigma = diag(\sigma_1, ..., \sigma_n) \in \mathbb{R}^{n \times n},$$

where U and V have orthonormal columns ($U^TU = I$, $V^TV = I$) and Σ contains the singular values σ_i ordered in a non-increasing way ($\sigma_1 \geq ... \geq \sigma_n \geq 0$) [63]. $\mathbf{u}_i$ and $\mathbf{v}_i$ denote the left and right singular vectors of A, respectively. For PCA calculation it is very convenient that V represents the matrix of principal components, Σ contains the square

[1] For the basics of principal component analysis the reader is referred to the literature [62].

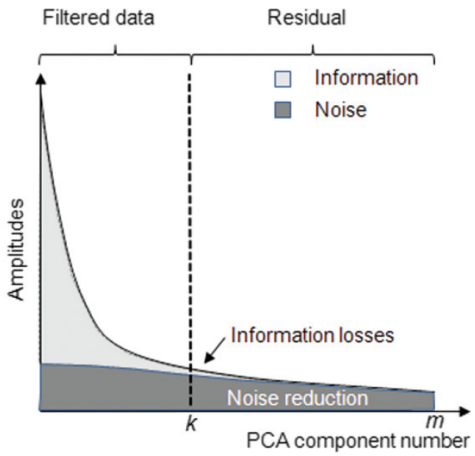

Figure 2.6: Dependency of the amount of information and noise in PCA transformed data on the principal component number. If the back transformation is done with a reduced number of principal components ($k < m$), noise can be reduced but also a part of the informative signal may be lost. Image taken from [66].

root of the variances and U is the matrix of scaled versions of the individual transformed observations (for details see [62, 65]).

The first few principal components represent the most informative part of the data, while noise is assumed to be evenly distributed on all components [66] (see light and dark grey areas in Figure 2.6). A reduction of noise in the data can be accomplished by using $k < m$ principal components for the back transformation. The smaller k, the higher the noise reduction but also the higher the information loss (see Figure 2.6). The common problem is therefore to determine the optimal cut-off value of components in order to maximize noise reduction as well as information conservation [66]. In this thesis, the number of components for the back transformation k is estimated by an automated approach introduced by Balvay et al. [66], which uses the fraction of residual information (FRI) criterion [67].

The FRI method assumes that the residual signal, which is calculated by subtracting the filtered from the original signal, is composed of an informative part and random noise (see Figure 2.6). For a given k, the FRI in each pixel (FRI_{pk}) can be calculated as [66]:

$$FRI_{pk} = \frac{\|i_{pk}\|^2}{\|i_{pk} + n_{pk}\|^2} = \frac{\|i_{pk}\|^2}{\|r_{pk}\|^2}, \tag{2.10}$$

where i_{pk} denotes the informative signal, n_{pk} random noise and r_{pk} the residual signal. In order to maximize the information in the filtered signal, the FRI has to be minimized. Balvay et al. estimate $\|i_{pk}\|^2$ by using the temporal autocorrelation function of the residual signal ($C_{rr}(j)$), which is defined as [67]:

$$C_{rr}(j) = \frac{1}{N - |j|} \sum_{i=1}^{N-j} r(t_i) r(t_{i+j}), \tag{2.11}$$

where N is the number of samples of the signal r and j the time lag. $C_{rr}(j)$ can be considered as the sum of the respective autocorrelations of informative and noise signal and the intercorrelation between them [66]. Since the statistical expectation of the autocorrelation of white noise is zero for $j > 0$, $C_{rr}(j)$ corresponds in theory to the autocorrelation of the informative signal for $j > 0$ [67]. In order to estimate the contribution of i_{pk} at $j = 0$, Balvay et al. fit a second-order polynomial to $C_{rr}(j)$ for low values of j and extrapolate it to zero. $\|i_{pk}\|^2$ can then be determined as:

$$\|i_{pk}\|^2 = N \cdot P_{rr}(0), \tag{2.12}$$

where $P_{rr}(0)$ is the fitted polynomial function at $j = 0$.

Calculating the FRI for every pixel in the ROI yields a FRI map and a corresponding FRI histogram, which represents the global information loss [66]. Since not only the information loss but also the uncertainty of the estimator contributes to the FRI distribution, it is necessary to correct for the uncertainty of the estimator. This is done by comparing the FRI distribution with a reference FRI distribution which corresponds to the uncertainty of the estimator [66]. Balvay et al. generate the reference FRI distribution by replacing the original signals with spatially independent Gaussian noise signals and calculating the FRI map as described above.

In order to determine the optimal cut-off value of principal components, FRI and reference FRI distribution are calculated for an increasing number of principal components, respectively. For every component number, the histograms of FRI and reference FRI map are compared by counting the number of occurrences L where the FRI distribution is higher than the reference FRI distribution [66]. Those occurrences reflect the true information loss

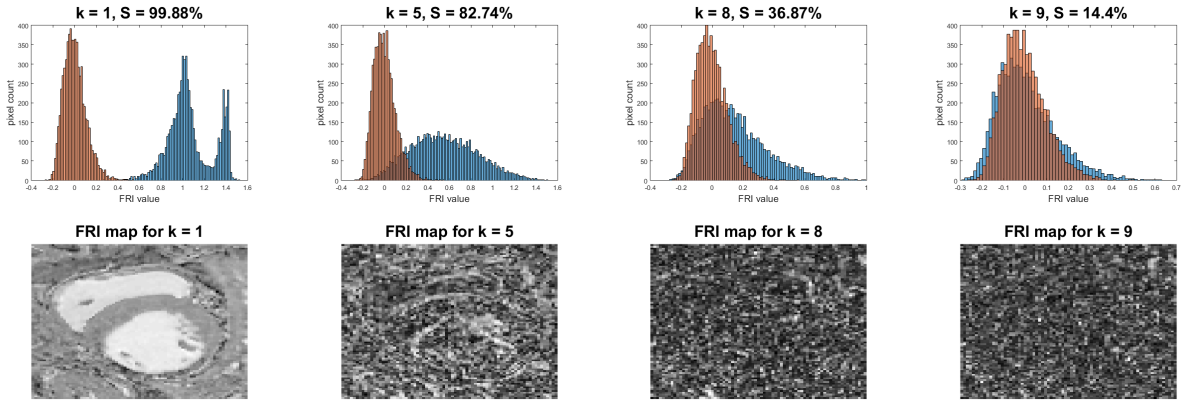

Figure 2.7: FRI map and histogram for an increasing number of principal components. In the first row the orange histogram represents the reference FRI distribution, the blue histogram the data FRI distribution. The second row shows the data FRI maps corresponding to the number of principal components k used for back transformation. As k increases, information loss decreases. At the optimal number of components, the data FRI histogram resembles the reference FRI histogram and no anatomical structures can be identified in the FRI map. The percentage S is used as a marker of this event. In this thesis, the optimal number of components is chosen as the first one where $S \leq 15\%$ (in this example at 9 principal components). It can be noticed that for low values of principal components the FRI values of some pixels are higher than one. This occurs if the noise peak of the autocorrelation at $j = 0$ is smaller than the peak of the informative part of the signal, leading to an over-estimation of the FRI value by the polynomial fit.

that does not arise from the uncertainty of the estimator. Hence, one needs to determine the principal component number k for which L is minimized. Balvay et al. express the number of occurrences as a percentage S of the total number of pixels in the FRI map. This percentage decreases with increasing k until the optimum k is reached (see Figure 2.7). Incrementing the number of principal components is stopped and therefore the optimal k found when the percentage drops under a threshold value, which corresponds to the accepted information loss [66].

When simulating Gaussian noise signals to determine the reference FRI distribution, one has to choose a value for the noise standard deviation. In this thesis, the standard deviation is estimated using the 'difference method' [68], which evaluates the difference image of two

subsequent images acquired with the same imaging parameters [69]. The noise standard deviation can be estimated in a ROI of the difference image according to [68]:

$$\sigma_{ROI} = \sqrt{\frac{var(S_1 - S_2)|_{ROI}}{2}} = \frac{std(S_1 - S_2)|_{ROI}}{\sqrt{2}}, \tag{2.13}$$

where S_1 and S_2 are the subsequent images. Since this equation bases on the assumption of a Gaussian noise distribution in the evaluated region, the ROI must be placed in a region with sufficiently high SNR [70].

Implementation: The noise standard deviation is determined using two subsequent images of the original DCE series (before limiting it to the heart ROI)[2] that correspond to time points before contrast agent arrival in the right ventricle. The user is asked to draw with `roipoly` three times one after the other a ROI in fat tissue, a region exhibiting high SNR. The noise standard deviation is then calculated as the mean value of the standard deviations determined for the three ROIs using Equation (2.13). The Gaussian noise signal for the reference FRI distribution is generated with `randn` choosing the same dimensions as the ones of the heart ROI image series and using the estimated standard deviation. As another preparation step, `pchip` interpolation (see Section 2.4.4) is applied on the image series to ensure uniform time spacing, which is required for autocorrelation calculation.
PCA is performed with the function `pca`, which uses by default the SVD algorithm. The input data for `pca` has to be organized as a two-dimensional matrix P where the rows correspond to the observations (pixels of each image in the time series) and the columns correspond to the variables (time points):

$$P = \begin{pmatrix} p_1(t_1) & p_1(t_2) & \dots & p_1(t_N) \\ p_2(t_1) & p_2(t_2) & \dots & p_2(t_N) \\ \vdots & \vdots & \ddots & \vdots \\ p_M(t_1) & p_M(t_2) & \dots & p_M(t_N) \end{pmatrix}, \tag{2.14}$$

[2]The noise estimation is the only step in the data processing pipeline that re-uses the non-cropped original images because regions in fat tissue are evaluated.

where N is the total number of time frames and M the total number of pixels in each image. After application of the `pca` function, the back transformation is performed with a reduced number of principal components in order to reduce the noise in the data. The estimation of the optimal number of principal components for back transformation is done iteratively, starting at five components. In each iteration, the following steps are performed:

- apply PCA filtering (transformation and back transformation) on the image data series and reference noise series using the current number of principal components to keep,
- calculate the respective residuals for image data series and reference noise series,
- calculate for both residuals the temporal autocorrelation in every pixel using `xcorr` with maximum lags equal to 20 and scale option 'unbiased',
- fit a second order polynomial to the values from $j = 1$ to $j = 19$ of each autocorrelation function using `polyfit` and determine the value at $j = 0$ via extrapolation,
- calculate the FRI for every pixel using equation (2.10), which yields a data and reference FRI map,
- determine the optimal histogram bin width applying the Freedman–Diaconis rule [71] on the reference FRI map,
- calculate data and reference FRI histogram using `histcounts`,
- count the number of occurrences where the data FRI histogram is higher than the reference FRI histogram and express it as a percentage S of all pixels in one FRI map,
- if $S \leq 15\%$, end the loop and select the current number of principal components as the optimal one; otherwise, increment the number of components and start the next iteration.

2.4.6.2 Savitzky-Golay filtering

The second option of denoising implemented in this thesis is applying a Savitzky-Golay (SG) filter [72]. This smoothing filter bases on polynomial regression, which is performed consecutively on a series of data points that are treated as equidistant [73]. For a single data point the new value is determined by fitting a polynomial in the least-square sense to all data points inside a symmetric window around the current data point. The window length as well as the order of the polynomial is chosen by the user. After determination of the new value for the current data point, the window slides one step to the right and the fitting process restarts for this new data point. Different window lengths yield different fitting results. Therefore, a suitable window length for every SI or $[CA]$ time curve is determined in this thesis by an adaptive filtering approach, while the order of the fitting polynomial is kept fixed. Assuming that for a perfect fit the residual is equal to white noise, the optimal window length in a certain range is determined by finding the window length corresponding to the minimum absolute mean residual.

Implementation: The SI or $[CA]$ time curves are first interpolated and up-sampled to 300 equidistant points using `pchip`. Increasing the apparent temporal resolution leads to a better fit due to more data points while ensuring that the original curve shape is well preserved. Savitzky-Golay filtering is done using the function `sgolayfilt`, which requires the input parameters *signal*, *window_length* and *polynomial_order*. For all signal curves third order polynomials are chosen. In contrast, for the window length a difference is made between AIF and myocardial signal curve. Since the AIF is calculated as the mean signal in the left-ventricular ROI, it is not distorted by noise. Therefore, the window length for the AIF is chosen $w = 5$, which basically keeps the signal curve as it is. For the myocardial signal curves, the window length is chosen by adaptive filtering. At this, `sgolayfilt` is applied to the signal 15 times, starting at $w = 0.25 \cdot length(signal)$ and increasing the window length by 6 sample points each round. For every filtered signal corresponding to a certain window length the residual is calculated and the optimal window length is chosen as the one that minimizes the absolute value of the mean residual.

2.5 Perfusion quantification

2.5.1 Semi-quantitative analysis

2.5.1.1 Maximum and minimum detection

Detecting the maximum and minimum value of SI and $[CA]$ curves is a crucial step since those values are used in several other processing steps, like the SI to $[CA]$ conversion or the determination of semi-quantitative parameters. Since for the evaluated curves maximum detection is less complicated than minimum detection, it is done first and then the maximum is used as a landmark for minimum detection.

As can be inferred from Figure 1.2, the maximum detection of the AIF is straightforward. Detecting the maximum in the myocardial signals, however, proves difficult since the curves reach their maximum more slowly and exhibit only a gentle descent, if any. The sought-for maximum of myocardial curves is the one at the end of the first contrast wash-in (see Figure 1.7). The condition employed is that the maximum of the myocardial signal has to be found before end of first pass of contrast agent, which is defined at the minimum point of the valley after the maximum point of the AIF [57]. Furthermore, the detected maximum has to be $\geq 80\%$ of the global maximum value of the first pass limited curve to avoid local maxima detection.

The minimum point is defined as the minimum before contrast wash-in. In order to determine the minimum, the zero-crossings of the first derivative of the curve from $t = 0$ to the maximum point are detected and the corresponding local minima evaluated. The sought-for minimum is chosen as the minimum closest to the maximum point which has a value smaller than a certain percentage of the maximum value (60% for myocardial SI curves, 10% for AIF SI curve and all $[CA]$ curves). Additionally, it is ensured that the sought-for minimum value cannot be smaller than the baseline, which is calculated as the mean value from $t = 0$ to the site of the current evaluated local minimum point.

Regarding the implementation it should be noted that for PCA filtered curves the function `gradient` is used to determine the first derivate since it can work with non-uniform time spacing. In case of Savitzky-Golay filtered curves, the `diff` function is applied.

2.5.1.2 Up-slope, AUC and SIM calculation

For determination of the up-slope parameter, the first derivative of the signal points between the minimum and maximum point is calculated. In order to avoid spotting the maximum slope too close to the minimum or maximum point, only the central points of the temporal interval (30% in both directions around the central point between minimum and maximum point) are evaluated to determine the maximum slope point. This point is chosen as the center point for a three point linear fit to the signal curve in case of the AIF or a five point linear fit in case of a myocardial signal, which is done with the function `polyfit`. The up-slope is then determined as the slope of the fitted line.
The time-to-peak is determined as the temporal distance between minimum and maximum point of the curve. The area under the curve is calculated using time-to-peak and the function `trapz`. The signal intensity maximum is determined as the maximum of the myocardial signal relative to its baseline, which is estimated as the mean of the values measured before contrast agent arrival in the LV (from $t = 0$ up to the minimum point of the AIF). To allow an inter-patient comparison, each semi-quantitative parameter is normalized by the respective parameter calculated for the AIF.

If semi-quantitative parameters are calculated not only for myocardial pixels but for all pixels in the whole heart ROI, one additional step is employed that detects if the current pixel can be categorized as a myocardial or a LV pixel. This is necessary because the SI to $[CA]$ conversion algorithm as well as the algorithm for determination of semi-quantitative parameters treat AIF and tissue curve differently. Categorizing a pixel as a LV pixel is done by checking if the maximal value of the pixel's corresponding signal curve is $\geq 50\%$ of the maximum value of the AIF.

2.5.2 Quantitative analysis

2.5.2.1 Fermi function model constrained deconvolution

Fermi function modeling was introduced by Axel [74], who showed in computed tomographic (CT) brain perfusion studies that the expected shape of the impulse response for an intravascular tracer is very similar to the one of a Fermi function [7]. The Fermi representation of the impulse response is defined as [31]:

$$R_F(t) = MBF \cdot sg \cdot \left[\frac{1}{e^{(t-\tau_0-\tau_d)\cdot k}+1}\right] \cdot \theta\left(t-\tau_d\right), \tag{2.15}$$

where $R_F(t)$ is the myocardial perfusion-weighted impulse response, MBF the myocardial blood flow, sg the specific gravity of myocardial tissue and τ_0 the width of the initial plateau of the Fermi function before it decays with rate k. τ_d denotes the time delay between contrast agent arrival in the LV and in the analyzed myocardial region. $\theta\left(t-\tau_d\right)$ is a unit step function that is 0 for $t < \tau_d$ and 1 for $t \geq \tau_d$.

Since the Fermi function approximates the impulse response for an intravascular contrast agent, it is necessary to limit the signal curves obtained with an extracellular contrast agent to the first pass, a phase where the differences between intravascular and extracellular contrast agent are negligible [7]. Jerosch et al. [31] determine the parameters MBF, τ_0 and k using a Marquardt-Levenberg non-linear least squares fitting algorithm [73] when calculating equation (1.6). τ_d is thereby kept fixed at a user defined value. However, since τ_d can differ between myocardial regions due to their different vascular properties, it is treated as unknown in this thesis. In order to determine the correct τ_d for every pixel, the Fermi parameters are fitted for a set of time shifts. τ_d is then determined as the time shift corresponding to the impulse response that minimizes the squared L^2-norm of the residual of measured and fitted myocardial $[CA]$ time curve. Finally, the myocardial blood flow in units of $ml \cdot min^{-1} \cdot g^{-1}$ is calculated using the maximal amplitude value of the myocardial perfusion-weighted impulse response, R_{max}.

Implementation: AIF and myocardial $[CA]$ time curves are first limited to the first pass as described in Section 2.5.1.1. For determining the parameters MBF, τ_0 and k the function `lsqnonlin` with its option `'levenberg-marquardt'` is used. The fitting function is the convolution of the Fermi function with the AIF, calculated with the discrete version of equation (1.6) [75]:

$$c_{tissue}(t_i) = \sum_{j=1}^{N} A_{ij} R_{Fj}. \tag{2.16}$$

A is the convolution matrix constructed from the AIF [47]:

$$A = \begin{pmatrix} c_{AIF}(t_1) & 0 & \dots & 0 \\ c_{AIF}(t_2) & c_{AIF}(t_1) & \dots & 0 \\ \vdots & \vdots & \ddots & \vdots \\ c_{AIF}(t_N) & c_{AIF}(t_{N-1}) & \dots & c_{AIF}(t_1) \end{pmatrix} \cdot \Delta t, \quad A \in \mathbb{R}^{N \times N}, \tag{2.17}$$

where $c_{AIF}(t_i), i = 1...N$ is the AIF value at a certain time point and N is the number of samples. The starting values are chosen as $MBF = \frac{0.01}{sg}$, $\tau_0 = 0.5 \cdot length(first\_pass)$ and $k = 100$ since they yield physiologically meaningful solutions. The output of `lsqnonlin` includes the fitted Fermi function parameters as well as the squared L^2-norm of the residual. The fitting process is repeated for time shifts from $\tau_d = 0 \cdot \Delta t$ to $\tau_d = 15 \cdot \Delta t$ and the correct one determined as the one that yields the minimal squared L^2-norm of the residual. The maximal amplitude value of the myocardial perfusion-weighted impulse response corresponding to the determined τ_d is then used to calculate MBF according to [49]:

$$MBF = \frac{R_{max}}{\Delta t \cdot sg}, \tag{2.18}$$

where Δt is the sampling interval equal to the mean heart rate of the patient and $sg = 1.05 g/ml$.

2.5.2.2 Tikhonov regularization with B-splines

Jerosch et al. [47] proposed in 2002 to solve the problem of deconvolving AIF and tissue curve by using a model-independent representation of the impulse response and applying Tikhonov regularization [76]. In order to include smoothness and continuity constraints to the solution of the impulse response, the authors represent $R_F(t)$ as a sum of piecewise smooth B-spline components:

$$R_F(t_i) = sg \cdot \sum_{j=1}^{p} B_j^{(k)}(t_i) \cdot \alpha_j, \quad \alpha_j \in \mathbb{R}. \tag{2.19}$$

In the equation above, $B_j^{(k)}(t_i)$ denotes the j^{th} B-spline of order k, which is defined for a sequence of distinct and non-decreasing numbers, the knots ($\xi_1 \leq \xi_2 ... \leq \xi_{p+k}$), as [77]:

for $k = 1$

$$B_j^{(1)}(t) = \begin{cases} 1 & \text{if } \xi_j \leq t < \xi_{j+1} \\ 0 & \text{otherwise} \end{cases} \tag{2.20}$$

and for $k \geq 2$

$$B_j^{(k)}(t) = \begin{cases} \frac{t-\xi_j}{\xi_{j+k-1}-\xi_j} \; B_j^{(k-1)}(t) & \text{if } \xi_j \leq t < \xi_{j+1} \\ \frac{\xi_{j+k}-t}{\xi_{j+k}-\xi_{j+1}} \; B_{j+1}^{(k-1)}(t) & \text{if } \xi_{j+1} \leq t < \xi_{j+2}. \end{cases} \tag{2.21}$$

Each function $B_j^{(k)}(t)$ is positive definite and non-zero only at time points t_i that lie inside the interval $\xi_j ... \xi_{j+k}$ [47, 77]. α_j in Equation (2.19) are the real-valued B-spline coefficients. In order to generate a clamped B-spline curve, the knots are assigned to the so-called break points in a way that the first k knots take the value of the first break point, each interior knot corresponds to one break point and the last k knots take the value of the last break point [77]. Including the B-spline representation of the impulse response, the convolution in Equation (2.16) can be rewritten to [47]:

$$\begin{aligned} c_{tissue}(t_i) &= \sum_{j=1}^{p} \alpha_j \cdot sg \cdot \int_0^{t_i} B_j^{(k)}(s) \cdot c_{AIF}(t_i - s) ds \\ &= \sum_{j=1}^{p} D_{i,j} \cdot \alpha_j \cong \sum_{j=1}^{p} \sum_{l=1}^{i-1} \alpha_j \cdot sg \cdot B_j^{(k)}(u_l) \cdot c_{AIF}(t_i - u_l) \Delta t, \end{aligned} \tag{2.22}$$

where u is a dummy integration variable. The design matrix $D_{i,j}$ is introduced to express the convolution of the B-splines with the AIF more compactly [47]:

$$D_{i,j} = sg \cdot \int_0^{t_i} B_j^{(k)}(u) \cdot c_{AIF}(t_i - u)du, \quad D \in \mathbb{R}^{N \times p}. \tag{2.23}$$

In order to find a solution for the vector of B-spline coefficients $\boldsymbol{\alpha}$, the deconvolution problem can be recast into a linear least-squares problem [47, 77]:

$$min\{\|D \cdot \boldsymbol{\alpha} - \mathbf{c_{tissue}}\|^2; \boldsymbol{\alpha} \in \mathbb{R}^p\}. \tag{2.24}$$

It can be shown that the matrix D is ill-conditioned [75], which might lead to large disruptive oscillations in the solution [47]. Jerosch et al. [47] approach this problem by adding a side constraint to the system of linear equations in order to regularize the solution, as introduced by Tikhonov [76]:

$$min\{\|D \cdot \boldsymbol{\alpha} - \mathbf{c_{tissue}}\|^2 + \lambda^2 \|L\boldsymbol{\alpha}\|^2; \boldsymbol{\alpha} \in \mathbb{R}^p\}, \tag{2.25}$$

where $\|L\boldsymbol{\alpha}\|^2$ is termed the discrete smoothing norm [63]. L is typically the identity matrix I or a discrete approximation of first- or second-order derivative operator. $\lambda > 0$ is a weighting factor which balances the minimization of the residual norm with the minimization of the side constraint [47]. From Equation (2.25) it can be seen that the solution for $\boldsymbol{\alpha}$ is a trade-off between smoothing and goodness of fit [47]. In this thesis, L is chosen to be a first-order difference operator to reduce oscillations in the amplitudes of $\boldsymbol{\alpha}$, as suggested by Jerosch et al. [47].

By setting the first derivative of Equation (2.25) with respect to $\boldsymbol{\alpha}$ to zero one arrives at the normal equations [47]:

$$(D^T D + \lambda^2 L^T L)\boldsymbol{\alpha} = D^T \mathbf{c_{tissue}} \quad \Leftrightarrow \quad \boldsymbol{\alpha} = (D^T D + \lambda^2 L^T L)^{-1} D^T \mathbf{c_{tissue}}. \tag{2.26}$$

If $L \neq I$, the generalized singular value decomposition (GSVD) of the matrix pair (D, L) can be used to find a solution for the B-spline coefficient vector $\boldsymbol{\alpha}$ [63]. For the matrices $D \in \mathbb{R}^{N \times p}$ and $L \in \mathbb{R}^{r \times p}$, where $N \geq p \geq r$, the GSVD is defined as [78]:

$$D = U\Sigma X^{-1}, \quad L = VMX^{-1}, \tag{2.27}$$

$$\Sigma = \begin{pmatrix} \Sigma_r & 0 \\ 0 & I_{p-r} \end{pmatrix}, \quad \begin{pmatrix} M_r & 0 \end{pmatrix},$$

where $U \in \mathbb{R}^{N \times p}$ and $V \in \mathbb{R}^{r \times r}$ have orthonormal columns ($U^T U = I_p$, $V^T V = I_r$) and $X \in \mathbb{R}^{p \times p}$ is a non-singular matrix. $\Sigma_r = diag(\sigma_i)$ and $M_r = diag(\mu_i)$ are diagonal $r \times r$ matrices whose diagonal entries are non-negative and ordered and normalized as follows [79]:

$$0 \leq \sigma_1 \leq ... \leq \sigma_r \leq 1, \quad 1 \geq \mu_1 \geq ... \geq \mu_r \geq 0,$$

$$\sigma_i^2 + \mu_i^2 = 1, \quad i = 1, ..., r.$$

The generalized singular values of (D, L) are defined as [78]:

$$\gamma_i = \frac{\sigma_i}{\mu_i}, \quad i = 1, ..., r. \tag{2.28}$$

It can be shown that using the GSVD yields the following solution for the normal equations [63]:

$$\begin{aligned} \boldsymbol{\alpha} &= \sum_{i=1}^{s} \left(\frac{\gamma_i^2}{\gamma_i^2 + \lambda^2} \right) \cdot \frac{\mathbf{u}_i^T \mathbf{c_{tissue}}}{\sigma_i} \mathbf{v}_i + \sum_{i=s+1}^{p} (\mathbf{u}_i^T \mathbf{c_{tissue}}) \mathbf{v}_i \\ &= \sum_{i=1}^{s} f_i \cdot \frac{\mathbf{u}_i^T \mathbf{c_{tissue}}}{\sigma_i} \mathbf{v}_i + \sum_{i=s+1}^{p} (\mathbf{u}_i^T \mathbf{c_{tissue}}) \mathbf{v}_i, \end{aligned} \tag{2.29}$$

where s is the number of non-zero singular values and f_i are the filter factors. For generalized singular values γ_i much larger than λ, the filter factors are $f_i \approx 1$, and for $\gamma_i < \lambda$, $f_i \approx \frac{\gamma_i^2}{\lambda^2}$. Since the largest perturbations in the ordinary least squares solution (Equation (2.24)) correspond to the smallest σ_i [78] and $\sigma_i \approx \gamma_i$ for $\sigma_i << 1$, the filter factors of Tikhonov regularization can stabilize the solution if λ is chosen appropriately [47].

In order to determine a suitable value for the regularization parameter λ, the L-curve approach is used [78]. The L-curve is a log-log plot of the regularized solution norm $\|L\alpha_\lambda\|$ versus the corresponding residual norm $\|D \cdot \boldsymbol{\alpha}_\lambda - \mathbf{c_{tissue}}\|$ [79]. As can be seen in Figure 2.8, the curve is typically L-shaped, consisting of a vertical part, a corner and a horizontal part. The vertical part of the L-curve represents the solutions where small changes of λ

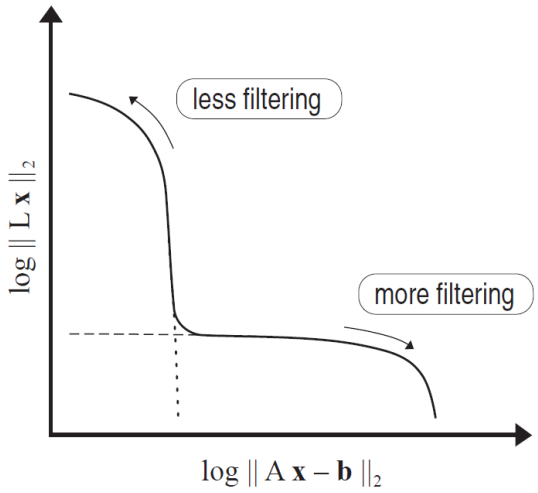

Figure 2.8: Generic form of the L-curve, where A corresponds to D, $\mathbf{x}$ to $\boldsymbol{\alpha}$ and $\mathbf{b}$ to $\mathbf{c_{tissue}}$. A higher weighting parameter λ favors the minimization of $\|L\alpha_\lambda\|$, which means more filtering and a smoother result. A smaller λ leads to less filtering and a better goodness of fit. Image taken from [79].

cause a drastic variation in $\|L\alpha_\lambda\|$ and therefore in the smoothness of the solution. The horizontal part, on the other hand, corresponds to solutions where $\|D \cdot \boldsymbol{\alpha}_\lambda - \mathbf{c_{tissue}}\|$ and therefore the goodness of fit is very sensitive to changes in the regularization parameter. As a consequence, the λ corresponding to the solution at the corner of the L-curve is considered the optimal regularization parameter, which achieves a small residual and solution norm [78]. After determination of the optimal λ and the corresponding B-spline coefficients α_i, the impulse response $R_F(t_i)$ can be calculated using Equation (2.19).

As explained for the Fermi function approach, when calculating the MBF it is necessary to address the time shift τ_d between contrast agent arrival in the LV and the myocardium. In their later work, Jerosch et al. [75] proposed a method to determine τ_d when model-independent deconvolution is used. This method is based on the authors' observation that the maximum value of the impulse response R_{max} stays approximately the same when the AIF is shifted in the direction of increasing time until the foot of the AIF passes by the foot of the tissue curve. For larger time shifts R_{max} increases significantly (see Figure 2.9). Jerosch et al. show with simulations that the time shift corresponding to the point where

R_{max} increases significantly can be considered the correct one. The authors also determine the MBF from the maximum amplitude of the impulse response rather than its initial amplitude value, which can be seen as a generalization of the convolutional relation where the input function is not directly measured at the inlet of the ROI [75].

Implementation: First of all, AIF and myocardial tissue curve are both divided by the same scaling factor which is equal to the area under the curve of the whole AIF, calculated using the function `trapz`. This normalization is done because it facilitates the comparison of the norms necessary for L-curve determination [47]. The impulse response is composed of fourth-degree B-spline polynomials with 15 equally spaced break points, as suggested by Jerosch et al. [47]. For creating the knot sequence with edge knots of multiplicity k the function `augknt` is used. Then the B-splines $B_j^{(k)}(t_i)$ are generated by the function `bspline_basis` and the design matrix $D_{i,j}$ is calculated according to Equation (2.23).
For the determination of the B-spline coefficients α_i functions of the 'Regularization Tools' library by Hansen [79] are used. First, the first-order difference operator L is generated with `get_l`. Then, the GSVD is calculated using `cgsvd` and the optimal value for the regularization parameter λ is determined with the function `l_curve`. In order to favor smooth results, an upper threshold for the regularized solution norm $\|L\alpha_\lambda\|$ is introduced that is set to $thr = 10^{-2.5}$, below which the corner of the L-curve is found by the function `l_corner`. After determining a suitable λ, the Tikhonov regularized solution for α_i is calculated with `tikhonov` and then inserted into Equation (2.19) to determine $R_F(t_i)$.
The impulse response is calculated for time shifts from $\tau_d = 0 \cdot \Delta t$ to $\tau_d = 15 \cdot \Delta t$, as done in the Fermi approach. Note that here the AIF is shifted in the direction of increasing time, which means that AIF and myocardial tissure curve need to be shortened by one time step after every round (the tissue curve at the first sampling point and the AIF at the last one). The maximum value of each impulse response corresponding to a certain time shift is saved into a vector, considering R_{max} as a function of τ_d. The correct time shift is determined as the point of the maximum curvature of $R_{max}(\tau_d)$, which is done by calculating the maximum of the second derivative of the function using `diff`. The corresponding MBF is then calculated according to Equation (2.18).

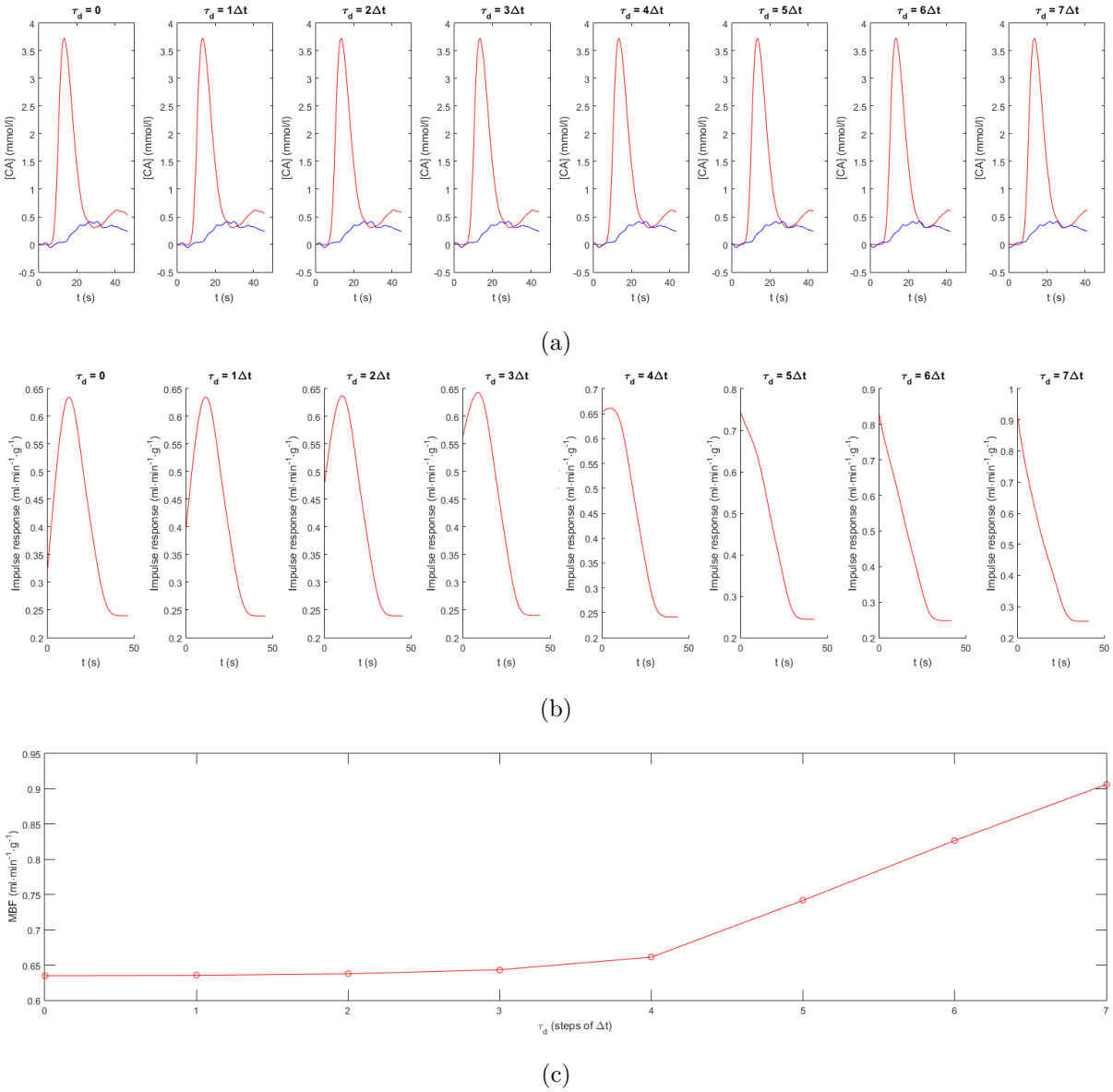

Figure 2.9: Exemplary impulse responses determined with model-independent deconvolution for different time shifts between AIF and myocardial curve. In (a) the AIF, shifted in the direction of increasing time, and the myocardial curve used for deconvolution are shown in red and blue, respectively. The corresponding determined myocardial perfusion-weighted impulse responses (expressed in units of $ml \cdot min^{-1} \cdot g^{-1}$) are plotted in (b). The graph in (c) shows the dependency of the myocardial blood flow estimate on the time shift τ_d. Note that MBF stays approximately constant until the foot of the AIF passes by the foot of the myocardial curve. In this example, $\tau_d = 4\Delta t$ is determined as the correct time shift.

2.5.2.3 ARMA model

The autoregressive moving average (ARMA)[3] approach allows parametric modeling of a dynamic system without any direct curve fitting [82]. It was introduced for myocardial perfusion quantification by Neyran et al. [48] in 2002. The ARMA model relates the discrete time samples of AIF ($c_{AIF}(t_i)$) and myocardial tissue curve ($c_{tissue}(t_i)$) according to [82]:

$$c_{tissue}(t_i) = \sum_{k=0}^{Q} b_k c_{AIF}(t_{i-k}) - \sum_{m=1}^{L} a_m c_{tissue}(t_{i-m}), \tag{2.30}$$

where b_k ($k = 0...Q$) and a_m ($m = 1...L$) are constants and L and Q are the auto-regressive (AR) and moving average (MA) order, respectively. This equation states that the value of the system output at any time, $c_{tissue}(t_i)$, can be predicted when knowing the L previous values of the observed output and Q previous values of the observed input [83]. The coefficients b_k and a_m can be determined as the least squares solution of Equation (2.30), which is given in matrix form as [82]:

$$\begin{pmatrix} c_{AIF}(t_1) & 0 & \dots & 0 & 0 & \dots & 0 \\ c_{AIF}(t_2) & c_{AIF}(t_1) & \dots & 0 & c_{tissue}(t_1) & \dots & 0 \\ \vdots & \vdots & \dots & \vdots & \vdots & \dots & \vdots \\ c_{AIF}(t_N) & c_{AIF}(t_{N-1}) & \dots & c_{AIF}(t_{N-Q}) & c_{tissue}(t_{N-1}) & \dots & c_{tissue}(t_{N-L}) \end{pmatrix} \cdot \begin{pmatrix} b_0 \\ \vdots \\ b_Q \\ -a_1 \\ \vdots \\ -a_L \end{pmatrix} = \begin{pmatrix} c_{tissue}(t_1) \\ c_{tissue}(t_2) \\ \vdots \\ c_{tissue}(t_N) \end{pmatrix}, \tag{2.31}$$

where $c_{AIF}(t_i)$ and $c_{tissue}(t_i)$ are assumed to be zero for $i \leq 0$ [82]. In order to determine the impulse response of the modeled system, the z-transform [84] can be applied on Equation (2.30):

$$\left[1 + \sum_{m=1}^{L} a_m z^{-m}\right] C_{tissue}(z) = \sum_{k=0}^{Q} b_k z^{-k} C_{AIF}(z). \tag{2.32}$$

[3]It would be more accurate to refer to the model in use as a description with linear constant coefficient difference equations (LCCDE) [80] since ARMA models describe stochastic processes [81] and in this thesis deterministic signals are studied. However, in the myocardial DCE-MRI literature ARMA is the commonly used term, which is why it is also used in this thesis.

By rearranging Equation (2.32) the z-transform of the impulse response can be obtained as:

$$R(z) = \frac{C_{tissue}(z)}{C_{AIF}(z)} = \frac{\sum_{k=0}^{Q} b_k z^{-k}}{1 + \sum_{m=1}^{L} a_m z^{-m}}. \tag{2.33}$$

Consequently, the inverse z-transform of $R(z)$ yields the myocardial perfusion-weighted impulse response $R_F(t_i)$ of the system. The MBF is then obtained from the maximum value of $R_F(t_i)$, while the correct time shift is determined in the same way as in the Fermi function approach (see Section 2.5.2.1).
Since the ARMA model corresponds to an infinite impulse response (IIR) system, $R_F(t_i)$ can get close to but never equal to zero [48]. Neyran et al. therefore point out to choose small values for Q and L in order to reduce the degrees of freedom and to stabilize the deconvolution process [48].

Implementation: As suggested by Batchelor et al. [80], the model orders are chosen as $Q = 0$ and $L = 2$. The coefficients b_k and a_m are determined from Equation (2.31) using `lsqlin`. Then, they are given as an input to the function `impz` which directly returns $R_F(t_i)$. In order to determine the correct time shift τ_d, $R_F(t_i)$ and the squared L^2-norm of the residual of measured and fitted myocardial curve are calculated for time shifts from $\tau_d = 0 \cdot \Delta t$ to $\tau_d = 15 \cdot \Delta t$. The correct time shift and the corresponding impulse response are chosen as the ones that minimize the squared L^2-norm of the residual. As the last step, the MBF is calculated according to Equation (2.18).

2.6 Analysis of quantitative perfusion maps

The semi-quantitative parameter maps of SI and $[CA]$ data (normalized US, AUC and SIM) as well as the MBF maps (Fermi modeling, Tikhonov regularization with B-splines and ARMA modeling) of each patient were analyzed visually and quantitatively. Quantitative pixel-wise analysis was supplemented by calculating the global mean values of perfusion parameters of all pixels in the myocardial ROI. An exemplary segmentation of

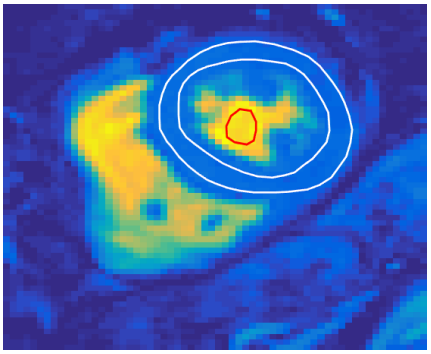

Figure 2.10: Segmentation of the myocardium (white) and the ROI in the LV blood pool (red).

the myocardium and the ROI in the LV blood pool are shown in Figure 2.10 (performed on SIM maps, as described in Section 2.5.1).

Visual analysis was carried out by two experienced observers of myocardial DCE-MRI. The ground truth for presence of perfusion deficits and/or dark rim artifacts was determined by visual evaluation of each patient's DCE series (together with late enhancement (LE) images indicating necrotic myocardial areas). This evaluation yielded subendocardial perfusion deficits for three of the eight compared patients. Furthermore, dark rim artifacts were present in the DCE series of three patients. Areas of reduced values of myocardial perfusion parameters were interpreted as perfusion deficits on quantitative perfusion maps. For the visual analysis of MBF maps the latter were overlaid on a gray-scale SIM map for better orientation and calculation was performed for a dilated ROI including areas around the myocardium (see Figure 2.11). When the region of perfusion deficits on quantitative perfusion maps coincided with (or was included in) the region found for the ground truth, the perfusion deficit was interpreted as true perfusion deficit else as false perfusion deficit.

2.7 Phantom experiment

A phantom experiment was carried out in order to validate the approach of SI to $[CA]$ conversion used in this thesis. The phantom consisted of 16 glass bottles filled with Gadovist-doped water of different concentrations (see Figure 2.12). The contrast agent

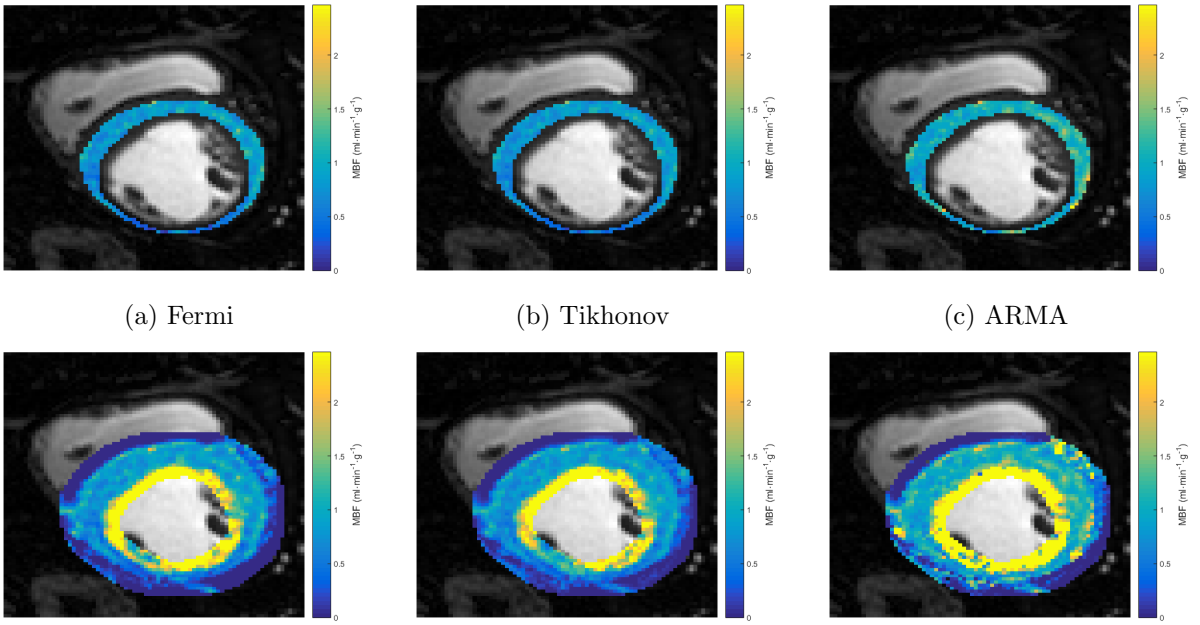

(a) Fermi (b) Tikhonov (c) ARMA

(d) Fermi, dilated ROI (e) Tikhonov, dilated ROI (f) ARMA, dilated ROI

Figure 2.11: MBF maps determined with Fermi modeling, Tikhonov regularization with B-splines and ARMA modeling for the myocardial ROI as well as a dilated version of it. The MBF maps are overlaid on a gray-scale SIM map for better orientation.

concentration ranged from 0 to 5 mmol/l (see Table 2.1). For the measurements the bottles were placed into a water bath in the isocenter of the scanner. MRI acquisition was performed using the same sequences and settings as described in Section 2.2. Mean SI in the DCE series as well as mean T_1 value from the MOLLI measurement were determined in each of the bottles.

The goal of the experiment was to calculate the approximated contrast agent concentrations $[\tilde{CA}]$ using Equation (2.3) and Equation (1.1) to compare the results with the ground truth $[CA]$ values. The scaling factor Ψ of the signal model was estimated according to Equation (2.5) using the measured SI and T_1 value of pure water. The T_1 relaxivity constant of Gadovist in water, r_1, was estimated by inserting the ground truth $[CA]$ values and the respective measured T_1 values into Equation (1.1) and calculating the mean value of all obtained r_1 values.

Table 2.1: Contrast agent concentrations in the different bottles of the phantom.

bottle nr.	1	2	3	4	5	6	7	8	9	10	11	12	13	14	15	16
$[CA]$ (mmol/l)	0	0.01	0.2	0.3	0.4	0.5	0.7	0.9	1.2	1.5	2	2.5	3	3.5	4	5

Figure 2.12: Phantom consisting of 16 glass bottles filled with Gadovist-doped water of different concentrations.

2.8 Statistical analysis

Statistical analysis was performed using the programs MedCalc (MedCalc Software, Ostend, Belgium) and Matlab (Mathworks Inc., Natick, USA). Mean values are generally specified together with standard deviations (SD). A significance level of 0.05 was employed for statistical tests.

The relationship between calculated contrast agent concentrations $[\tilde{CA}]$ and ground truth contrast agent concentrations $[CA]$ in the phantom experiment to validate the SI to $[CA]$ conversion was determined by linear regression. Coefficient of determination (R^2) and 95% confidence intervals for intercept and slope were used to check the compatibility with the identity relationship.

The visual agreement of perfusion deficits found in any type of quantitative perfusion maps compared to the ground truth for presence of perfusion deficits from corresponding dynamic DCE-MRI series was specified as sensitivity and specificity together with their 95% confidence intervals. Relationships between semi-quantitative and quantitative perfusion parameters were analyzed by means of correlation and linear regression analysis. Linear regression equations and coefficients of determination were calculated for global mean

values, pixel-wise for every patient as well as for all pixels of all compared patients. Moreover, global quantitative myocardial perfusion determined with Fermi modeling, with Tikhonov regularization with B-splines and with ARMA modeling were compared by paired t-test (without multiple comparison correction).

3 Results

3.1 Phantom experiment

The signal intensity measured at increasing contrast agent concentrations of the phantom is shown in Figure 3.1. The relation between SI and $[CA]$ is approximately linear for low dosages of contrast agent and non-linear at higher dosages.
The estimation of the T_1 relaxivity constant of Gadovist in water at approximately $19°C$ yielded $r_1 = 3.98 l/mmol \cdot s$. The resulting relation between the ground truth concentration $[CA]$ and the concentration $[\tilde{CA}]$ derived via the signal intensity model is plotted in Figure 3.2. The high coefficient of determination ($R^2 = 0.988$) and the regression equation ($y = 0.997x - 0.089$ with 95% confidence intervals $[0.93, 1.06]$ and $[-0.23, 0.05]$ for slope and intercept, respectively) suggest the validity of the SI to $[CA]$ conversion approach.

3.2 Denoising for semi-quantitative analysis

PCA denoising and Savitzky-Golay filtering were applied on raw SI time curves to investigate the behaviour of each method and decide for one of them for further use in semi-quantitative analysis.

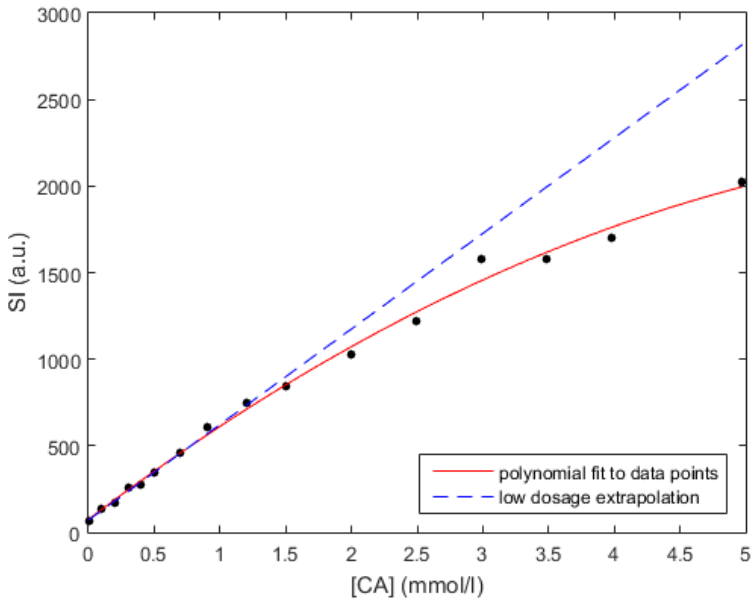

Figure 3.1: Measured phantom signal intensity as a function of contrast agent concentration. The red curve fitted to the measurement points emphasizes the non-linear relation between SI and $[CA]$. The blue dashed line represents the extrapolation of the linear relation between SI and $[CA]$ at low contrast agent dosage.

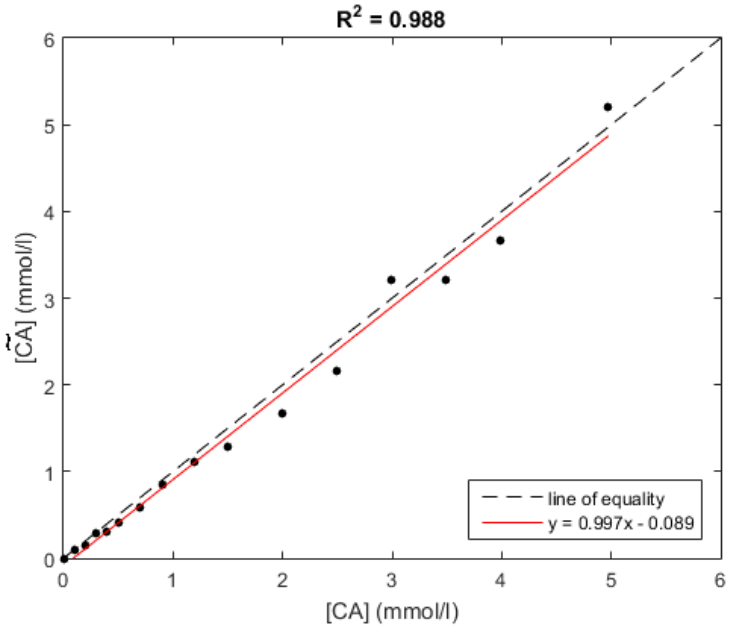

Figure 3.2: Relationship between ground truth concentration $[CA]$ and the concentration $[\tilde{CA}]$ derived via the signal intensity model.

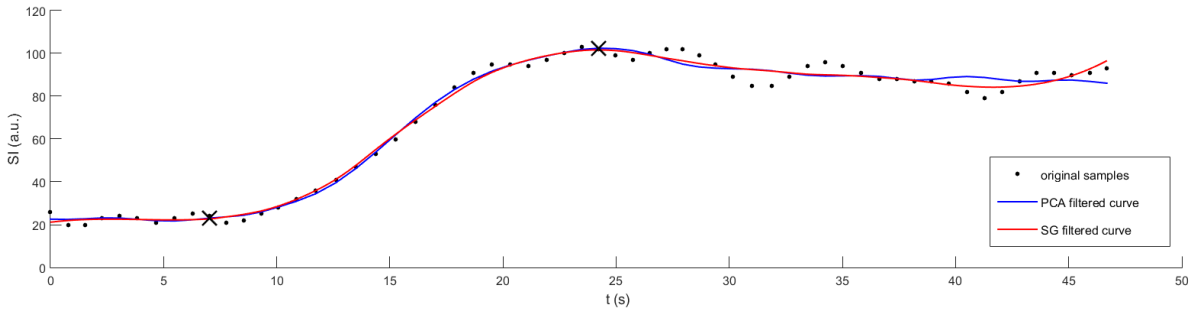

Figure 3.3: Direct comparison of the results of SI time curve denoising with PCA and Savitzky-Golay filter. The black crosses mark the detected minimum and maximum point of the denoised curves.

3.2.1 Automated PCA filter

The automated determination of the optimal number of principal components using a threshold of $S \leq 15\%$ worked for 10 of the 11 patients. For the remaining patient the principal component number at the lowest reached value of S was chosen as the optimal one (at $S = 18\%$). The mean computation time for determination of the principal component number was $40.5 \pm 4.5s$. After determination of the optimal principal component number, the PCA filter processing time for denoising of the whole heart ROI of one patient was on average $0.075 \pm 0.003s$.

3.2.2 Savitzky-Golay filter

The mean computation time of applying the adaptive SG filter on the whole heart ROI of one patient was $54.1 \pm 7.7s$.

3.2.3 Comparison of denoising methods

PCA denoising and Savitzky-Golay filtering were compared qualitatively by evaluating denoised SI time curves and calculating semi-quantitative parameter maps with the

denoised data obtained with both methods. Figure 3.3 shows a direct comparison of the results of applying both methods to a typical raw myocardial SI time curve. Both denoised curves closely resemble each other, especially in the part used for determination of the semi-quantitative parameters (between minimum and maximum point). The first two rows in Figure 3.4 illustrate maps of the semi-quantitative parameters up-slope, area under the curve and signal intensity maximum calculated for SI time data which had been denoised with each method, respectively. The difference maps obtained by subtracting the semi-quantitative parameter maps of SG filtered data from the respective maps of PCA filtered data are depicted in the third row in Figure 3.4. The difference in the myocardial region is very small for all three parameters. For all further calculations in semi-quantitative analysis PCA denoising was employed because of its higher computational efficiency.

3.3 Semi-quantitative analysis of SI data

The average computation time for the determination of the semi-quantitative parameters US, AUC and SIM for one signal curve was $7.88 \cdot 10^{-4} s$. Typical semi-quantitative parameter maps are shown in the first row in Figure 3.4. Notably a (true) perfusion deficit is visualized at the inferior wall of the left ventricle. Sensitivity and specificity for the detection of perfusion deficits were highest for the SIM maps (see Table 3.1). Dark rim artifacts were never mistaken for a perfusion deficit in any of the semi-quantitative perfusion maps. Normalized global US, AUC and SIM values are specified in Table 3.2 and show only small variation between patients.

3.4 Semi-quantitative analysis of [CA] data

The mean value of the measured pre-contrast $T_{1,0}$ values used for signal intensity to concentration conversion was $1962.0 \pm 50.2 ms$ for the LV blood pool and $1242.5 \pm 73.5 ms$ for the myocardium.

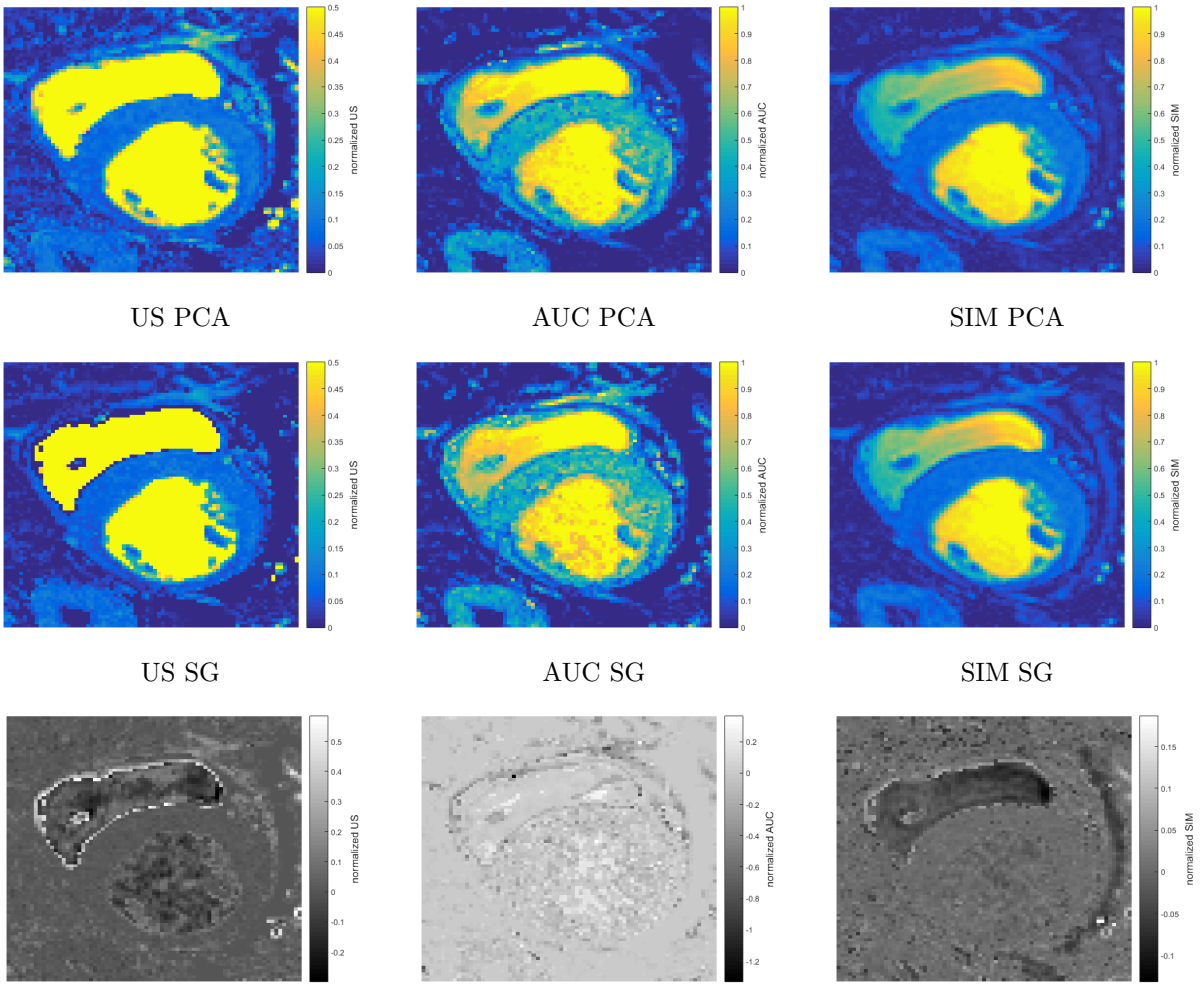

Figure 3.4: Comparison of maps of the semi-quantitative parameters US, AUC and SIM. The first two rows show the semi-quantitative parameter maps obtained from PCA and Savitzky-Golay filtered data, respectively. The third row depicts the difference maps calculated by subtracting the respective maps in the second row from the ones in the first row.

Table 3.1: Specificity, sensitivity and corresponding 95% confidence intervals for visual detection of perfusion deficits in semi-quantitative parameter maps of SI data.

parameter	**sensitivity**	**specificity**
US SI	67 [9, 99]	100 [48, 100]
AUC SI	100 [29, 100]	80 [28, 100]
SIM SI	100 [29, 100]	100 [48, 100]

Table 3.2: Mean, standard deviation and range of the normalized global mean values of the SI semi-quantitative parameters of all patients.

parameter	**mean ± SD**	**range**
US SI	0.077 ± 0.008	[0.064, 0.087]
AUC SI	0.283 ± 0.075	[0.165, 0.367]
SIM SI	0.145 ± 0.019	[0.115, 0.170]

3.4.1 Visual analysis and global indices

Figure 3.5 shows typical semi-quantitative parameter maps of $[CA]$ data of the same patient as in Figure 3.4. Whereas specificity for the detection of perfusion deficits was 100% for all types of semi-quantitative parameter maps, sensitivity was smaller than 100% for all variants (see Table 3.3). Similar as in the SI case, dark rim artifacts were never mistaken for a perfusion deficit in any of the semi-quantitative perfusion maps.
Normalized global US $[CA]$, AUC $[CA]$ and SIM $[CA]$ values are specified in Table 3.4 and show compared to the SI case higher variation between patients.

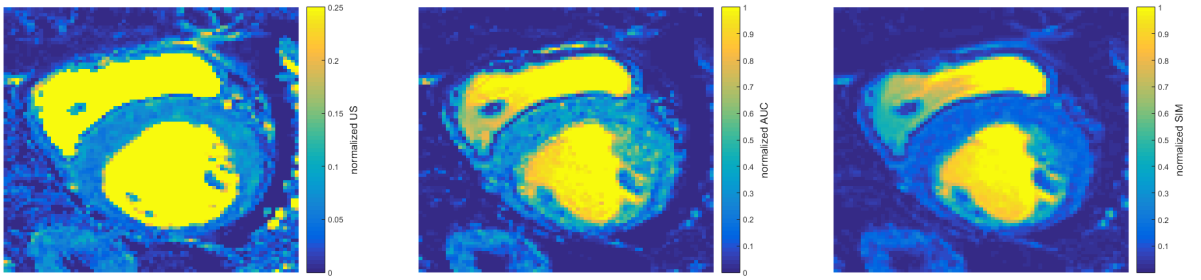

US AUC SIM

Figure 3.5: Typical semi-quantitative parameter maps of $[CA]$ data.

Table 3.3: Specificity, sensitivity and corresponding 95% confidence intervals for visual detection of perfusion deficits in semi-quantitative parameter maps of $[CA]$ data.

parameter	**sensitivity**	**specificity**
US $[CA]$	67 [9, 99]	100 [48, 100]
AUC $[CA]$	33 [1, 91]	100 [48, 100]
SIM $[CA]$	67 [9, 99]	100 [48, 100]

3.4.2 Correlation between semi-quantitative parameters of SI and [CA] data

The correlations between corresponding normalized SI and $[CA]$ semi-quantitative parameters are summarized in Table 3.5. The correlation was worst for US. Moreover, R^2 of pixel-wise correlation varied substantially between patients.

Figure 3.6 shows the scatter plot and regression line of all patients' normalized global mean values of corresponding SI and $[CA]$ semi-quantitative parameters. Figure 3.7 illustrates the scatter plot and regression line of the SI and $[CA]$ semi-quantitative parameters calculated for all myocardial pixels of all patients.

Table 3.4: Mean, standard deviation and range of the normalized global mean values of the [CA] semi-quantitative parameters of all patients.

parameter	**mean ± SD**	**range**
US [CA]	0.057 ± 0.013	[0.034, 0.072]
AUC [CA]	0.239 ± 0.070	[0.140, 0.331]
SIM [CA]	0.111 ± 0.026	[0.066, 0.134]

Table 3.5: Correlation between respective SI and [CA] semi-quantitative parameters. R^2 all patients = mean and standard deviation of the R^2 values of all patients; R^2 global means = R^2 of the global mean values of all patients; R^2 all pixels = R^2 of all myocardial pixels of all patients.

parameter	**R^2 all patients** mean ± SD	**R^2 global means**	**R^2 all pixels**
US	0.374 ± 0.179	0.496	0.360
AUC	0.434 ± 0.254	0.735	0.584
SIM	0.422 ± 0.253	0.735	0.558

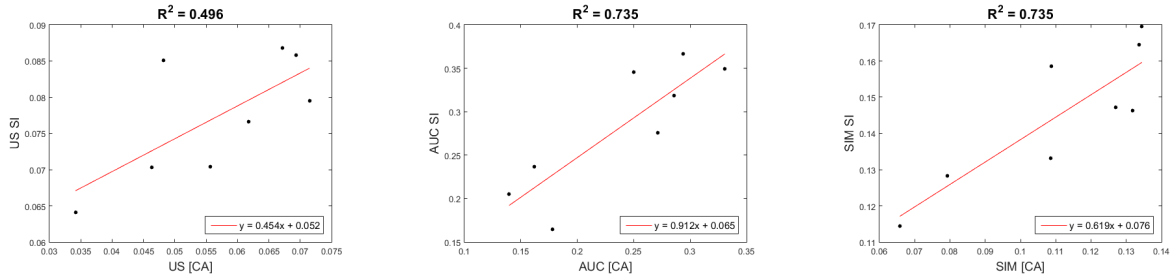

(a) US (b) AUC (c) SIM

Figure 3.6: Scatter plot, regression line and R^2 of normalized global mean values of SI and [CA] semi-quantitative parameters of all patients.

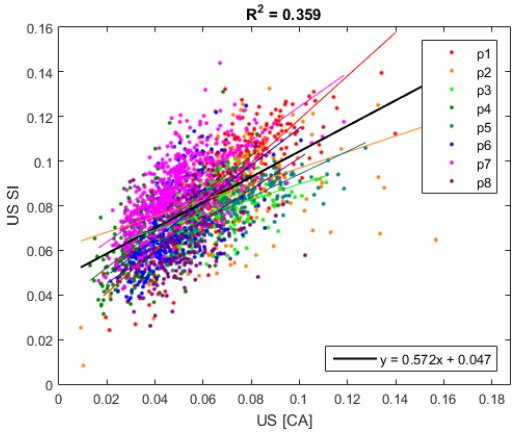

(a) US

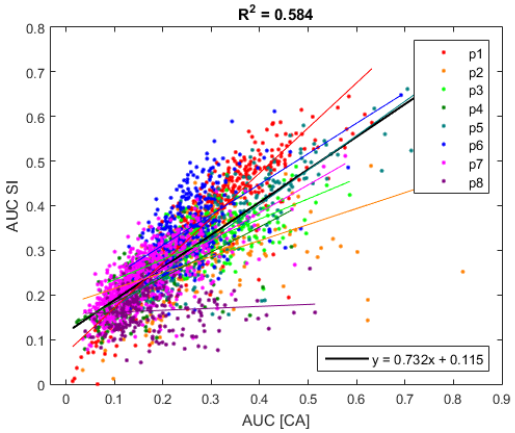

(b) AUC

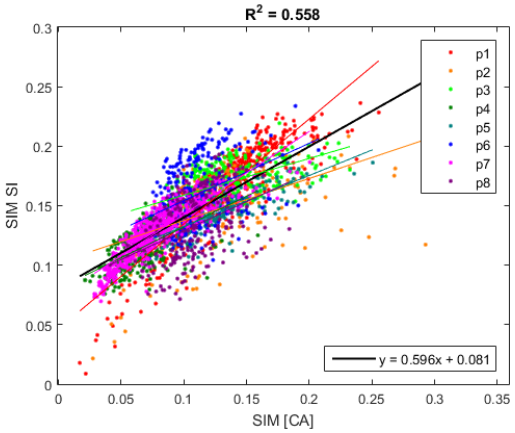

(c) SIM

Figure 3.7: Scatter plot, regression line and R^2 of normalized SI and $[CA]$ semi-quantitative parameters of all myocardial pixels of all patients. The contributions of each patient (p1 to p8) are color coded and respective regression lines are indicated.

3.5 Quantitative analysis

3.5.1 Typical single pixel results

The average computation time of deconvolving one signal curve with the AIF was $0.106s$ for Fermi modeling, $0.388s$ for Tikhonov regularization with B-splines and $0.064s$ for ARMA modeling. Typical impulse responses obtained by application of the three deconvolution methods on the $[CA]$ signal curve of a single myocardial pixel are illustrated in Figure 3.8 (a) to (c). The impulse response of Fermi modeling is the only one starting at its maximum value and declining to zero. Impulse responses obtained with Tikhonov regularization with B-splines typically show no or only a slight ascent in the beginning and a plateau when the minimum of the impulse response is reached. ARMA impulse responses exhibit an initial steep ascent followed by an approximate exponential decay. Figure 3.8 (d) shows the myocardial curve fit resulting from convolving each impulse response ((a) to (c)) with the AIF. Due to its restriction to first pass, the Fermi fit curve is shorter than the other two. In the given example, the time shift determined with Tikhonov regularization was $\tau_d = 1 \cdot \Delta t$, while both Fermi and ARMA modeling yielded $\tau_d = 2 \cdot \Delta t$.

3.5.2 Visual analysis and global indices

Figure 2.11 shows typical MBF maps determined with Fermi modeling (a), Tikhonov regularization with B-splines (b) and ARMA modeling (c) together with the dilated ROI versions (d)-(f) used for visual analysis. The sensitivity and specificity of the visual detection of perfusion deficits in the MBF maps with dilated myocardial ROI are given in Table 3.6. MBF maps determined with Fermi modeling were most accurate, but no method reached 100% sensitivity. As in the case of semi-quantitative perfusion maps, in no case a dark rim artifact led to a visual perfusion defect in the MBF maps.

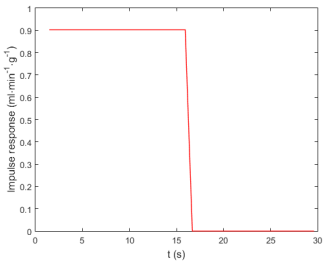

(a) Fermi impulse response

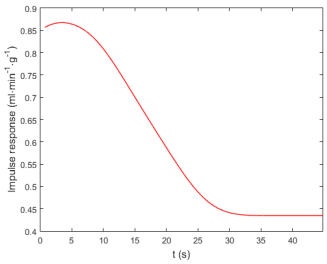

(b) Tikhonov impulse response

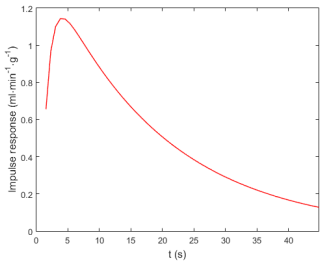

(c) ARMA impulse response

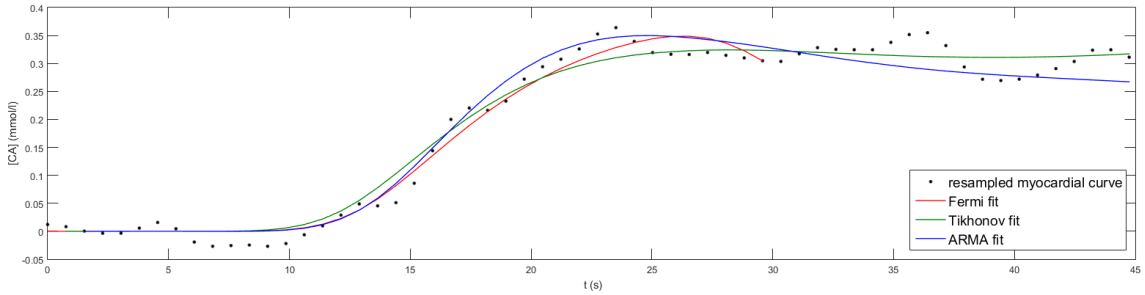

(d) Myocardial curve fit obtained by convolution of each impulse response with the AIF.

Figure 3.8: Typical impulse responses and myocardial curve fits obtained with Fermi modeling, Tikhonov regularization with B-splines and ARMA modeling.

Table 3.6: Specificity, sensitivity and corresponding 95% confidence intervals for visual detection of perfusion deficits in MBF maps determined with Fermi modeling, Tikhonov regularization with B-splines and ARMA modeling.

method	**sensitivity**	**specificity**
Fermi	67 [9, 99]	100 [48, 100]
Tikhonov	67 [9, 99]	80 [28, 100]
ARMA	67 [9, 99]	40 [5, 85]

Global MBF values determined with the three deconvolution methods differed significantly (see Figure 3.9 (a)).

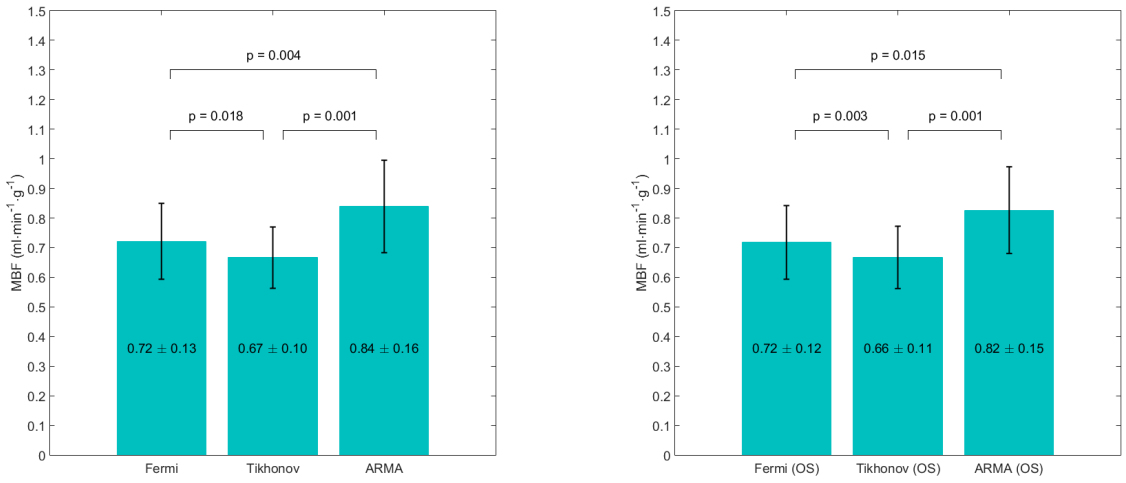

(a) (b)

Figure 3.9: Mean and standard deviation of the global mean MBF values of all patients determined with Fermi modeling, Tikhonov regularization with B-splines and ARMA modeling (a) without and (b) with outlier suppression (OS). The standard deviation is indicated with error bars. p-values refer to paired t-test. (Outlier suppression, see Section 3.5.6)

3.5.3 Correlation between MBF and semi-quantitative parameters of SI data

Table 3.7 shows the correlations between MBF and normalized SI semi-quantitative parameters for the global mean values of all patients and for all myocardial pixels of all patients. Furthermore, mean and standard deviation of all patients' R^2 values are given. In general, pixel-wise correlations were only moderate. Similar to the correlations between semi-quantitative SI and $[CA]$ parameters, correlation were worst for US. Figure 3.10 illustrates the scatter plots and regression lines of the combinations of MBF method and semi-quantitative parameter that yielded the lowest and highest R^2 taking the mean value of each row in columns 3 and 4 in Table 3.7.

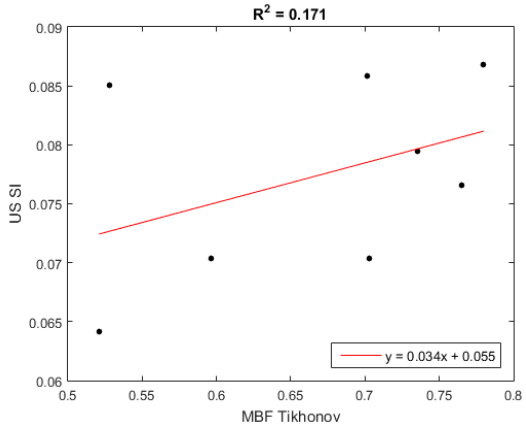

(a) MBF Tikhonov vs. US SI

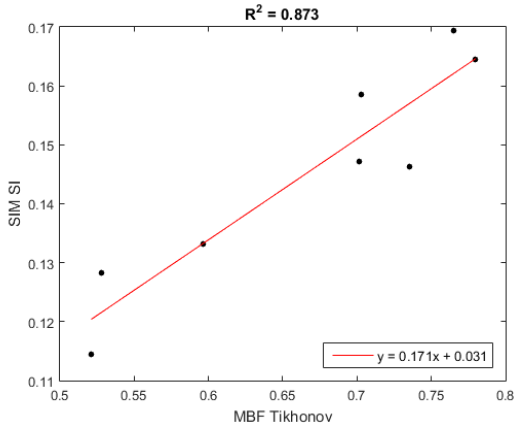

(b) MBF Tikhonov vs. SIM SI

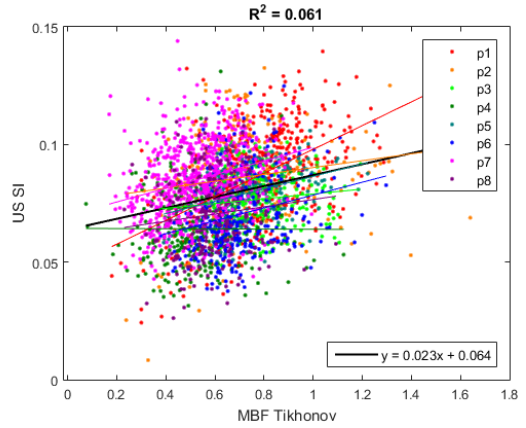

(c) MBF Tikhonov vs. US SI

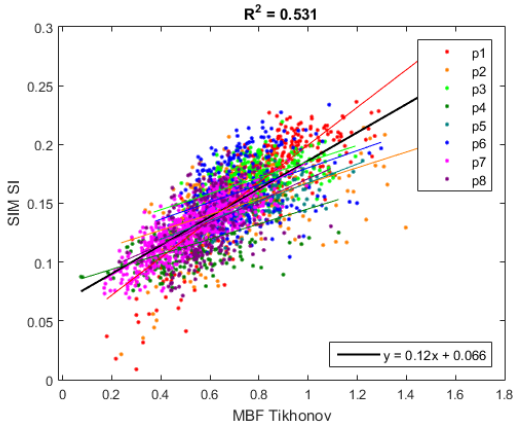

(d) MBF Tikhonov vs. SIM SI

Figure 3.10: Exemplary scatter plots, regression lines and R^2 describing the relation between semi-quantitative parameters of SI data and MBF results of different deconvolution methods for global mean values ((a) and (b)) and for all myocardial pixels of all patients ((c) and (d)). The contributions of each patient (p1 to p8) are color coded and supported by respective regression lines.

Table 3.7: Correlation between SI semi-quantitative parameters and MBF determined with Fermi modeling, Tikhonov regularization with B-splines and ARMA modeling. R^2 all patients = mean and standard deviation of the R^2 values of all patients; R^2 global means = R^2 of the global mean values of all patients; R^2 all pixels = R^2 of all myocardial pixels of all patients.

parameter	**R^2 all patients** mean ± SD	**R^2 global means**	**R^2 all pixels**
MBF Fermi vs. US SI	0.068 ± 0.071	0.325	0.080
MBF Fermi vs. AUC SI	0.200 ± 0.131	0.584	0.317
MBF Fermi vs. SIM SI	0.395 ± 0.229	0.718	0.491
MBF Tikhonov vs. US SI	0.067 ± 0.076	0.171	0.061
MBF Tikhonov vs. AUC SI	0.198 ± 0.126	0.712	0.364
MBF Tikhonov vs. SIM SI	0.375 ± 0.215	0.873	0.531
MBF ARMA vs. US SI	0.208 ± 0.114	0.493	0.204
MBF ARMA vs. AUC SI	0.066 ± 0.034	0.414	0.178
MBF ARMA vs. SIM SI	0.295 ± 0.146	0.583	0.379

3.5.4 Correlation between MBF and semi-quantitative parameters of [CA] data

Table 3.8 presents the correlations between MBF and normalized $[CA]$ semi-quantitative parameters for the global mean values of all patients and for all myocardial pixels of all patients. Furthermore, mean and standard deviation of all patients' R^2 values are given. In contrast to the correlations with semi-quantitative parameters determined from SI curves, correlations were substantially stronger. Interestingly, there was neither a semi-quantitative parameter nor a deconvolution method showing overall stronger correlations than the others. Figure 3.11 illustrates the scatter plots and regression lines of the combinations of MBF method and semi-quantitative parameter that yielded the lowest and highest R^2 taking the mean value of each row in columns 3 and 4 in Table 3.8.

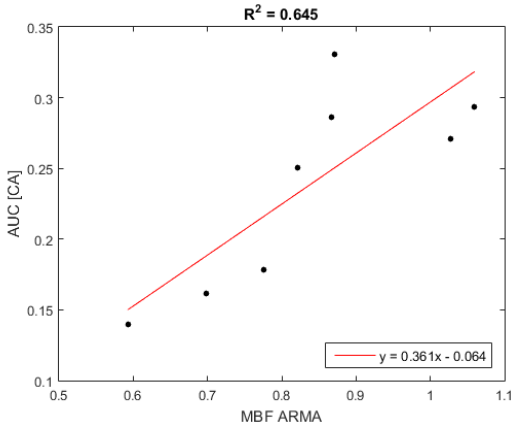

(a) MBF ARMA vs. AUC [CA]

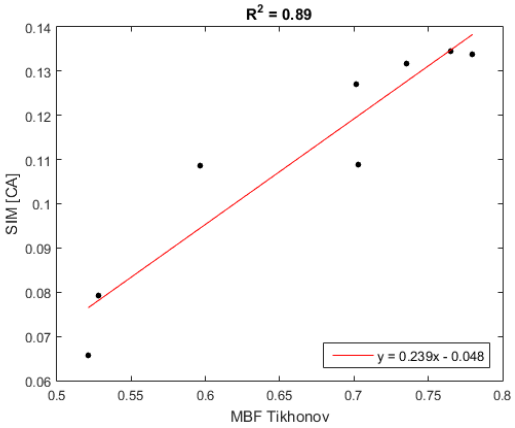

(b) MBF Tikhonov vs. SIM [CA]

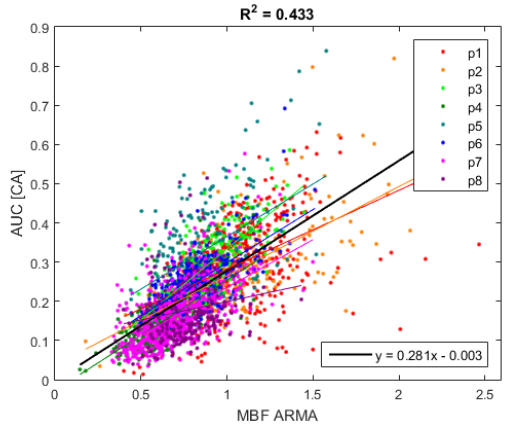

(c) MBF ARMA vs. AUC [CA]

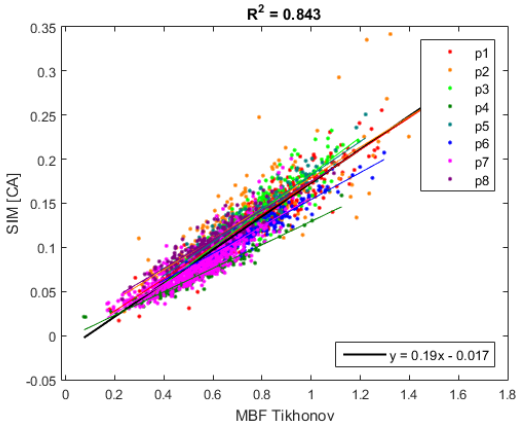

(d) MBF Tikhonov vs. SIM [CA]

Figure 3.11: Exemplary scatter plots, regression lines and R^2 describing the relation between semi-quantitative parameters of [CA] data and MBF results of different deconvolution methods for global mean values ((a) and (b)) and for all myocardial pixels of all patients ((c) and (d)). The contributions of each patient (p1 to p8) are color coded and respective regression lines are indicated.

Table 3.8: Correlation between [CA] semi-quantitative parameters and MBF determined with Fermi modeling, Tikhonov regularization with B-splines and ARMA modeling. R^2 all patients = mean and standard deviation of the R^2 values of all patients; R^2 global means = R^2 of the global mean values of all patients; R^2 all pixels = R^2 of all myocardial pixels of all patients.

parameter	**R^2 all patients** mean ± SD	**R^2 global means**	**R^2 all pixels**
MBF Fermi vs. US [CA]	0.618 ± 0.087	0.729	0.635
MBF Fermi vs. AUC [CA]	0.577 ± 0.187	0.888	0.660
MBF Fermi vs. SIM [CA]	0.899 ± 0.082	0.860	0.846
MBF Tikhonov vs. US [CA]	0.589 ± 0.077	0.591	0.584
MBF Tikhonov vs. AUC [CA]	0.554 ± 0.194	0.898	0.662
MBF Tikhonov vs. SIM [CA]	0.855 ± 0.077	0.890	0.843
MBF ARMA vs. US [CA]	0.769 ± 0.129	0.737	0.729
MBF ARMA vs. AUC [CA]	0.351 ± 0.186	0.645	0.433
MBF ARMA vs. SIM [CA]	0.668 ± 0.120	0.769	0.686

3.5.5 Correlation between MBF methods

In Table 3.9 the correlations between the MBF results obtained with the three deconvolution methods are presented for the global mean MBF values, the MBF values of all myocardial pixels of all patients and as mean and standard deviation of all patients' R^2 values. Whereas MBF determined with Fermi modeling and Tikhonov regularization with B-splines correlated excellently, correlation of both variants with MBF from ARMA modeling was notably smaller. The first row in Figure 3.12 shows the scatter plots and regression lines of all patients' global mean MBF values determined with Fermi modeling, Tikhonov regularization with B-splines and ARMA modeling. The first column in Figure 3.13 illustrates the scatter plots and regression lines of the MBF calculated with the three methods for all myocardial pixels of all patients. Obvious outlier pixels are striking in the scatter plots including MBF values determined by deconvolution with ARMA modeling.

Table 3.9: Correlation between MBF results obtained with Fermi modeling, Tikhonov regularization with B-splines and ARMA modeling without and with outlier suppression. R^2 all patients = mean and standard deviation of the R^2 values of all patients; R^2 global means = R^2 of the global mean values of all patients; R^2 all pixels = R^2 of all myocardial pixels of all patients; OS = outlier suppressed dataset.

methods	**R^2 all patients** mean ± SD	**R^2 global means**	**R^2 all pixels**
Fermi vs. Tikhonov	0.943 ± 0.009	0.858	0.910
Fermi vs. ARMA	0.757 ± 0.143	0.736	0.734
Tikhonov vs. ARMA	0.704 ± 0.125	0.715	0.694
Fermi vs. Tikhonov (OS)	0.946 ± 0.011	0.878	0.917
Fermi vs. ARMA (OS)	0.783 ± 0.083	0.781	0.794
Tikhonov vs. ARMA (OS)	0.741 ± 0.067	0.758	0.762

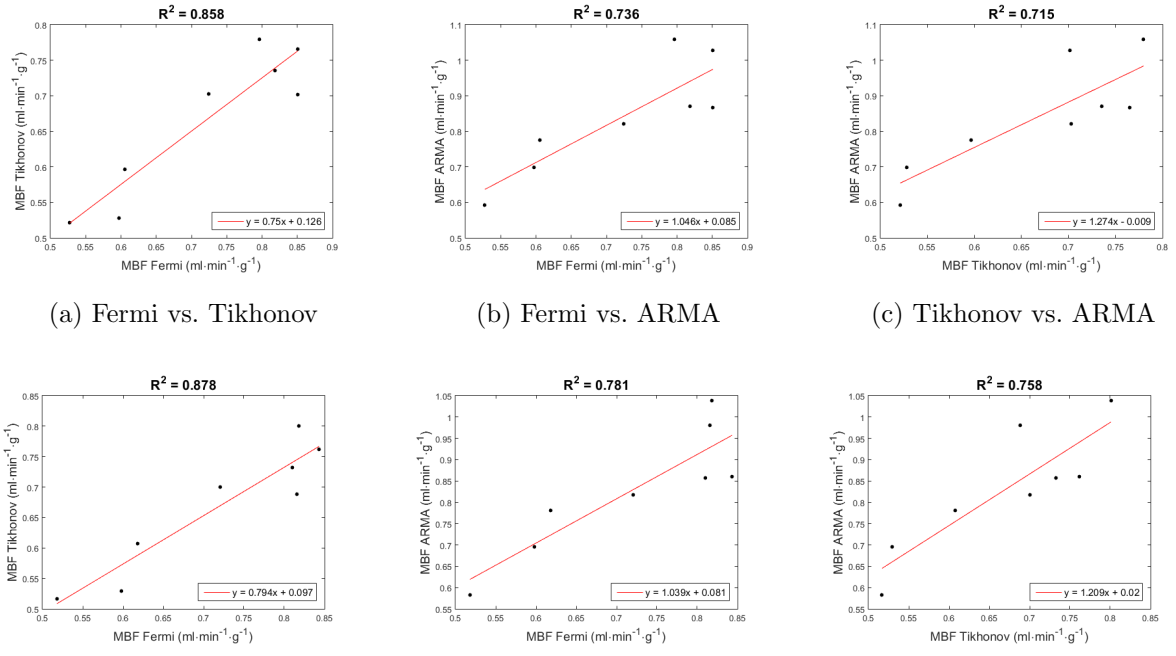

(a) Fermi vs. Tikhonov (b) Fermi vs. ARMA (c) Tikhonov vs. ARMA

(d) Fermi vs. Tikhonov (OS) (e) Fermi vs. ARMA (OS) (f) Tikhonov vs. ARMA (OS)

Figure 3.12: Scatter plots, regression lines and coefficients of determination R^2 of all patients' global mean MBF estimates. OS denotes the outlier-suppressed dataset (see Section 3.5.6).

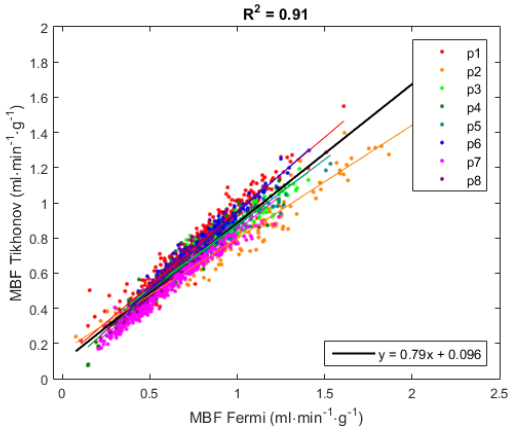

(a) Fermi vs. Tikhonov

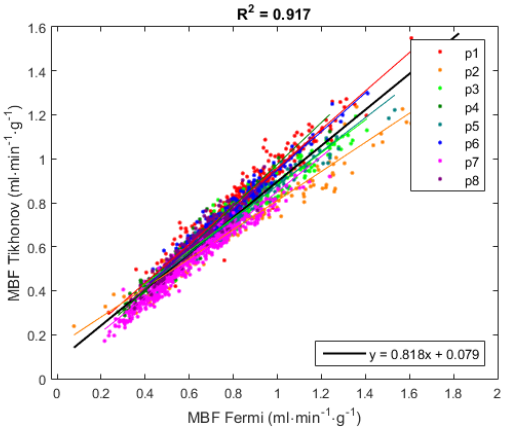

(b) Fermi vs. Tikhonov (OS)

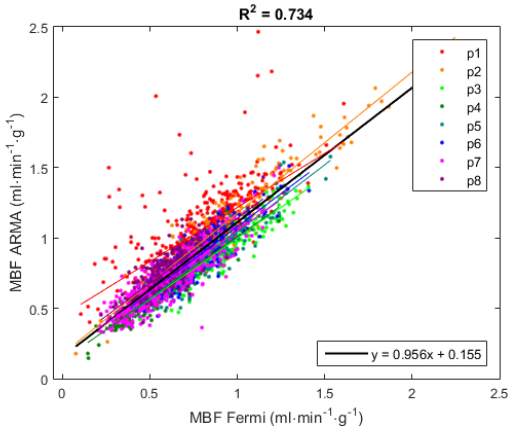

(c) Fermi vs. ARMA

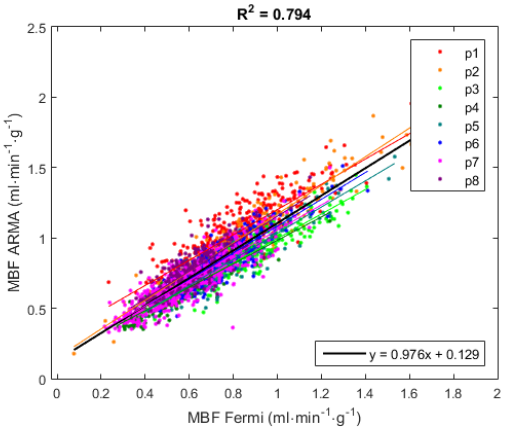

(d) Fermi vs. ARMA (OS)

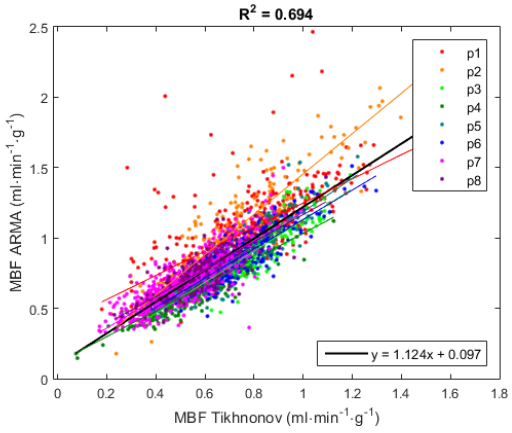

(e) Tikhonov vs. ARMA

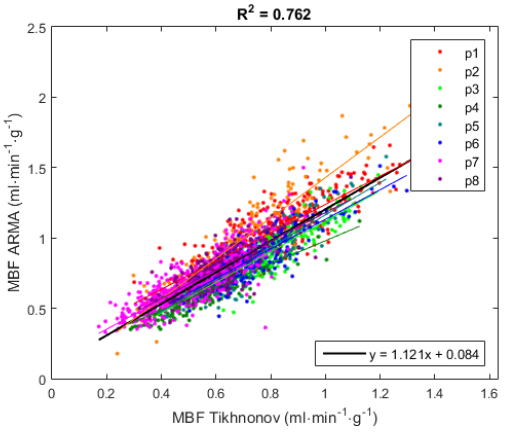

(f) Tikhonov vs. ARMA (OS)

Figure 3.13: Scatter plots, regression lines and coefficients of determination R^2 of MBF values of all myocardial pixels of all patients without and with outlier suppression (OS). The contributions of each patient (p1 to p8) are color coded and respective regression lines are indicated. (Outlier suppression, see Section 3.5.6)

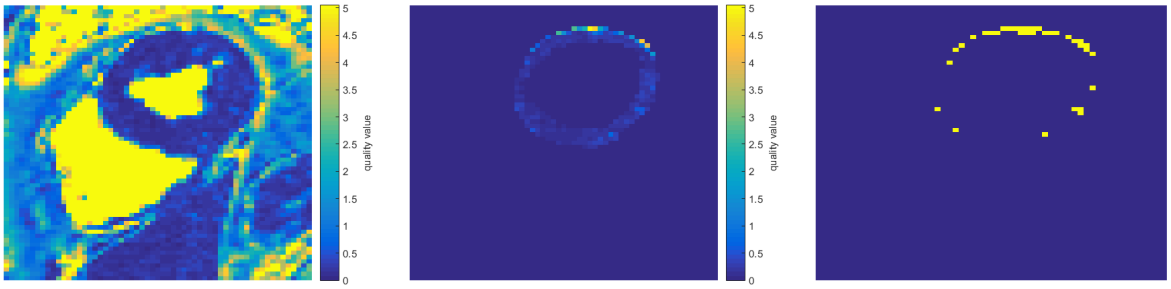

(a) quality map (b) quality map, myocardial ROI (c) detected outliers

Figure 3.14: Typical motion correction quality map and result of outlier detection.

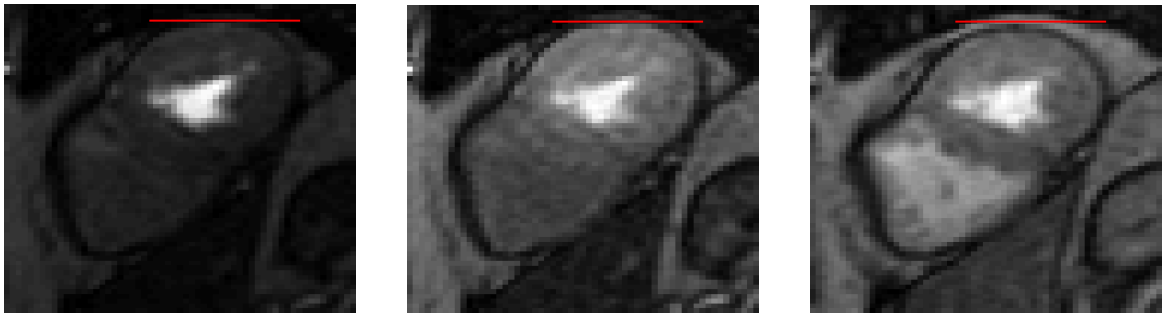

(a) t = 16.4s (b) t = 19.8s (c) t = 39.5s

Figure 3.15: Selected images at different time points of the DCE series corresponding to the quality map in Figure 3.14. The red line marks the position of the upper edge of the myocardium during first pass and emphasizes the myocardial displacement after first pass.

3.5.6 Motion correction quality map and outlier detection

The average time for determination of one pixel in the motion correction quality map was 0.075s. Figure 3.14 shows a typical quality map for the whole heart ROI (a) and the myocardial ROI (b) as well as the result of the outlier detection (c). Selected images of the corresponding DCE series are illustrated in Figure 3.15. During contrast agent arrival in the LV (a) and the myocardium (b) the upper edge of the myocardium is at the same position marked by the red line. After first pass (c), the upper edge has moved down two pixels. In this region the pixels of the quality map in Figure 3.14 (b) show a high deviation from the other myocardial pixels, which led to their classification as outliers.

The algorithm detected 8.4% of all myocardial pixels of all patients as outliers. The global mean MBF values and the correlations between the MBF methods were determined a second time for the outlier-suppressed (OS) myocardial ROI of all patients. The mean and the standard deviation of the global mean MBF values of all patients determined with the three deconvolution methods were modified minimally, but mostly in the case of MBF determined by deconvolution with ARMA modeling. Differences remained significant (see Figure 3.9 (b)). Outlier suppression altered correlations (see Table 3.9) as well as scatter plots together with regression lines (see Figures 3.12 and 3.13) primarily in case of involvement of MBF determined by deconvolution with ARMA modeling.

4 Discussion

The aim of this thesis was to determine and compare pixel-wise semi-quantitative and quantitative perfusion parameters from motion-corrected myocardial DCE-MRI data acquired in patients with coronary heart disease under resting condition. It was shown that myocardial perfusion parameter maps present information about perfusion deficits in a clear manner, which is a key advantage over visual evaluation of a whole DCE series. Moreover, parameter maps showed to be insensitive to the dark rim artifact, which may result in a decrease of the number of false positives in diagnosing perfusion deficits employing parameter maps. However, pixel-wise analysis is sensitive to noise and artifacts and therefore effective denoising methods and/or appropriate regularization techniques are required for calculation of perfusion parameter maps.

4.1 Deconvolution analysis

Method comparison Pixel-wise quantification of myocardial blood flow was feasible with all three deconvolution methods (Fermi modeling, Tikhonov regularization with B-splines, ARMA modeling). However, the p-values in Figure 3.9 (a) show a statistically significant difference in the results of MBF estimation of each method. Nevertheless, for all three deconvolution methods the obtained global mean MBF values are in the range of MBF estimates reported by other myocardial DCE-MRI studies at rest ($0.51ml \cdot min^{-1} \cdot g^{-1}$ to $1.03ml \cdot min^{-1} \cdot g^{-1}$) [39, 50, 85–88]. ARMA modeling yielded the highest mean MBF value and Tikhonov regularization a slightly lower one than Fermi modeling. The higher

ARMA mean MBF value fits well to the results of Neyran et al. [48], who reported for the ARMA method an overestimation of the MBF for values below $1ml \cdot min^{-1} \cdot g^{-1}$ in pixel-wise analysis of DCE data of an explanted pig heart. Zarinabad et al. [49] also observed an overestimation of the MBF by the ARMA approach in the whole range of 1 to $5ml \cdot min^{-1} \cdot g^{-1}$, investigated using a hardware perfusion phantom and pixel-wise evaluation. Fermi modeling and Tikhonov regularization have been shown to provide similar MBF estimates at rest in ROI-based [88] as well as pixel-wise [50] analysis. This is also suggested by the high R^2 values obtained when correlating both methods (see Table 3.9 and Figure 3.12 and 3.13). The correlation of each method with ARMA was notably lower, which partly arose from outliers, visible in the scatter plots of all myocardial pixels of all patients in Figure 3.13. Employing outlier suppression, the correlation between ARMA and each of the other methods was improved.

Fermi modeling Fermi modeling, the most widely applied deconvolution method in absolute quantification of myocardial perfusion [50], is straightforward to implement, fast compared to other deconvolution methods and only requires to specify the starting values of the nonlinear fitting process. It has been validated against PET [50] and microspheres [32, 89] and been shown to be robust against noise even in pixel-wise evaluation [49]. Moreover, Zarinabad et al. [49] reported in experiments with simulated data and their hardware perfusion phantom that Fermi modeling was approximating the myocardial blood flow well for low MBF values ($< 1ml \cdot min^{-1} \cdot g^{-1}$). However, in that study the absolute error of the Fermi method was high at higher MBF values [49]. This may arise from the disadvantage that the fixed impulse response shape assumption may not be appropriate [50]. One feature of the Fermi method different from the other two methods that should be pointed out is the restriction of the signal curves to first pass for extracellular contrast agents [7]. The limitation to first pass has the remarkable advantage that the function is fitted only to the part of the [CA] time curve that had been acquired during breath hold and is therefore most unlikely to show distortions due to motion. However, this statement goes along with the assumption that the end of first pass can be accurately determined. If specified, most authors define the end of first pass of AIF and tissue curve as the valley point after the

first peak of the AIF [57, 88], which might not necessarily coincide with the end of first pass in the myocardium. In this thesis, one patient was excluded from statistical analysis because of this reason; the maximum of the myocardial signal curve was not reached at chosen end of first pass (see Section 4.5). Nevertheless, Fermi modeling can be considered a robust method for perfusion quantification at rest.

Tikhonov regularization with B-splines Tikhonov regularization with B-splines is the most involved method to implement and also several times slower than the other two regarding computation time (see Section 3.5.1), which results from the determination of the optimal regularization parameter for the signal curve of every single pixel. If specified, the optimal regularization parameter is usually determined using the L-curve criterion in ROI-based analysis [47, 75, 90]. In pixel-wise analysis, however, choosing the point of the L-curve with maximum curvature led to under-regularized impulse responses with strong oscillations. Therefore, an upper threshold for the regularized solution norm of $\|L\alpha_\lambda\| \leq 10^{-2.5}$ was introduced, similarly as suggested by Sourbron et al. [91]. This ad-hoc solution has the disadvantage that it may work for a certain set of data, but that it cannot be considered generally applicable.

Like Fermi modeling, Tikhonov regularization with B-splines has also been validated against microspheres [47, 89] and PET [50]. Simulation results and experiments with a hardware perfusion phantom indicated that Tikhonov regularization is compared with Fermi modeling, ARMA modeling and exponential basis deconvolution [92] most sensitive to noise and showing the highest absolute error [49]. Unfortunately, the authors of that study did not specify exactly how they determined the regularization parameter.

A distinct advantage of Tikhonov regularization over other deconvolution methods is that the estimate of the myocardial blood flow as maximum of the impulse response is almost independent of the determined time shift τ_d as long as the foot of the AIF precedes or coincides with the foot of the tissue curve [75]. Therefore, if only the MBF value is of interest, a fixed time delay of $\tau_d = 0$ would still yield accurate MBF estimates (see Figure 2.9). Fermi modeling, in contrast, has been shown to be sensitive to the determined τ_d [93]. Jerosch et al. [47] mentioned as further advantage of Tikhonov regularization

that it is not necessary to restrict the signal curves to first pass. However, single pixel evaluation showed that taking the whole signal curves makes this method sensitive to motion artifacts, which are most probable after first pass due to the irregular breathing pattern of patients after breath-hold. One could suggest to restrict the signal curves to first pass as done for Fermi modeling, which has been shown in ROI-based analysis not to alter the result of Tikhonov regularization significantly [88]. However, this approach worked indeed for the majority of pixels but failed in some to produce a physiologically meaningful impulse response. To sum it up, Tikhonov regularization with B-splines has the potential to provide accurate myocardial perfusion estimates, but it is highly dependent on the quality of motion correction and the development of a generally applicable procedure for determination of the optimal regularization parameter per pixel is necessary.

ARMA modeling ARMA modeling with low auto-regressive and moving-average order is faster than other deconvolution methods [94] and has provided promising results in pixel-wise perfusion quantification [49, 95]. In greater detail, Zarinabad et al. obtained in their method comparison study [49] with ARMA modeling and exponential basis deconvolution the most accurate MBF estimates for simulated data as well as the hardware perfusion phantom. It is plausible that these two methods yield similar results since it has been shown that ARMA modeling can be considered as a generalization of the exponential basis deconvolution in the sense that it also implicitly models the impulse response as a sum of exponential functions just with a different approach to determine the exponents [80]. ARMA modeling is sensitive to the choice of auto-regressive (L) and moving-average order (Q) [95] and methods exist to determine the optimal ones [96]. In this thesis, the highest combination of orders yielding smooth impulse responses ($Q = 0$ and $L = 2$) was chosen. Figure 3.8 (c) shows that the ARMA impulse response does not fulfill the assumption of a monotonically decaying function, which might be an indication that the ARMA model is not completely appropriate.

Comparing the bar diagrams of the global mean MBF values with and without outlier suppression (see Figure 3.9) suggests that ARMA modeling is the method most sensitive to imperfect motion correction. The same can be deduced from a comparison of the

scatter plots of all myocardial pixels of all patients with and without outlier suppression in Figure 3.13. As with Tikhonov regularization, restricting the $[CA]$ time curves to first pass led to physiologically not meaningful impulse responses in some pixels. With the given data the promising results reported by Zarinabad et al. [49, 95] could not be reproduced, which can be explained by the sensitivity of the method to distortions in myocardial $[CA]$ time curves.

One general aspect that should be mentioned is that deliberately no denoising has been applied on the $[CA]$ time curves used for deconvolution in order to evaluate the performance of the deconvolution methods on raw signals and not alter the results by choice of a certain denoising method. This differs from the study by Zarinabad et al. [49] who applied spatial and temporal filtering previous to pixel-wise deconvolution analysis. Furthermore, Biglands et al. [57, 97] suggested to perform up-sampling on the interpolated $[CA]$ time curves. In this thesis, however, it was of interest to compare the deconvolution methods applied on signals with a natural sampling rate equal to the mean heart rate rather than comparing the effects of different sampling resolutions.

4.2 Semi-quantitative analysis

Denoising Denoising is an essential preprocessing step for pixel-wise determination of semi-quantitative perfusion parameters. A qualitative comparison between Savitzky-Golay filtering and PCA denoising yielded very similar results for both methods (see Figure 3.3 and 3.4). However, PCA exhibited two distinct advantages that led to the decision to choose PCA over Savitzky-Golay filtering. First, PCA uses the original data points, so the data is not altered by interpolation and up-sampling as necessary for Savitzky-Golay filtering. The low number of data points also results in less computation time of point-wise operations in semi-quantitative analysis. Second, once the optimal principal component number has been determined, PCA is extremely fast. Even including the time for optimal principal component number determination, PCA was faster than adaptive Savitzky-Golay

filtering for the denoising of the whole heart ROI.

A point of criticism of the chosen method is that arbitrary thresholds need to be set for subsequent automated determination of the optimal principal component number. First of all, the percentage S corresponding to the accepted information loss needs to be specified. As mentioned before, the threshold value had to be increased for one of the eleven patients since the threshold fixed for the other patients was not reached. A reason for this behavior could be that the previously determined heart ROI was not optimal in the sense that, apart from the tissue of interest, additional structures were included in the ROI, which may have influenced the result of the global filtering process [66]. Also Kim et al. [98], who applied automated PCA filtering on DCE computed tomography (CT) images, pointed out that for different clinical settings different threshold values may be appropriate. Consequently, further investigations are necessary to determine the optimal threshold value for every patient. A second issue of automated determination of the optimal principal component number using the FRI criterion concerns that there is no published information about a general rule for the choice of the maximum lag of the autocorrelation function and the upper boundary for the second order polynomial fit. In this thesis, the chosen maximum lag was oriented towards the default value of the Matlab autocorrelation function and the upper bound was chosen to be one point shorter than the maximum lag. To sum it up, the determination of the optimal principal component number using the FRI criterion requires development of decision rules for the choice of threshold values in order to be fully automated and generally applicable.

Semi-quantitative parameters Semi-quantitative parameters are usually calculated exclusively for SI time curves. However, the parameters are only determined correctly if a linear relationship between signal intensity and contrast agent concentration can be assumed [99]. Since for the applied contrast agent dosage of $0.05 mmol/kg$ body weight signal saturation can be expected for the AIF as well as myocardial tissue curve [29, 100], SI to $[CA]$ conversion was performed also for semi-quantitative analysis. In order to investigate the influence of the SI to $[CA]$ conversion, semi-quantitative parameters were determined for SI and $[CA]$ data. Relating SI and $[CA]$ semi-quantitative parameters in scatter plots

of all myocardial pixels of all patients (see Figure 3.7) indicated a non-linear relationship, which explains the rather low linear correlation values of SI and $[CA]$ semi-quantitative parameters and the high variation of R^2 values among patients (see Table 3.5). The scatter plots of normalized global mean values of SI and $[CA]$ semi-quantitative parameters of all patients in Figure 3.6 and the corresponding R^2 values suggest that the normalization of the parameters area under the curve and signal intensity maximum works well.
The correlations between SI semi-quantitative parameters and MBF estimates determined with Fermi modeling, Tikhonov regularization and ARMA modeling, respectively, have shown to be only moderate and especially low for the up-slope parameter (see Table 3.7). Correlating $[CA]$ semi-quantitative parameters with the MBF values determined with the three deconvolution methods yielded heterogeneous results (see Table 3.8). Fermi modeling and Tikhonov regularization showed a high correlation with the parameter signal intensity maximum, while ARMA modeling had the highest correlation with the up-slope parameter. However, taking into account all three deconvolution methods, the highest correlation was obtained with signal intensity maximum. The lower correlation of the deconvolution methods with the up-slope might be surprising since this parameter is considered the most reliable semi-quantitative parameter for evaluation of myocardial perfusion [101]. However, studies indicate that the up-slope is only superior if the ratio of up-slope values under stress and at rest (myocardial perfusion reserve index, MPRI) is used [99, 102, 103].

4.3 Visual analysis

Visual analysis yielded high sensitivities and specificities for the detection of subendocardial perfusion deficits in semi-quantitative parameter maps of SI data (see Table 3.1). In contrast, for semi-quantitative parameter maps of $[CA]$ data high specificity but only moderate sensitivity could be achieved (see Table 3.3). A reason for the lower sensitivity of detection of perfusion deficits in $[CA]$ semi-quantitative parameter maps may be that they are more noisy, showing a higher standard deviation relative to the mean value in the myocardial ROI than obtained for SI semi-quantitative parameter maps. It can be assumed that this

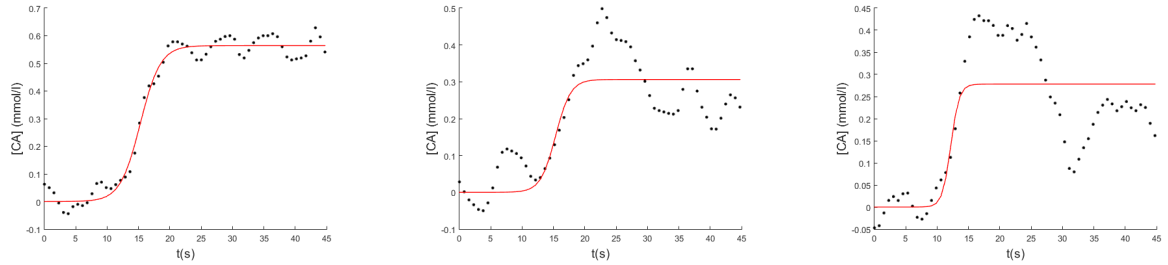

(a) (b) (c)

Figure 4.1: Exemplary sigmoid function fit to a typical (a) and distorted ((b) and (c)) myocardial $[CA]$ time curves of the same patient. Imperfect motion correction manifests in sudden jumps in the signal typically before contrast agent arrival in the myocardium (b) and right after end of breath-hold ((b) and (c)).

additional noise is introduced by the SI to $[CA]$ conversion algorithm. Visual analysis of MBF maps yielded the same moderate sensitivity for all three deconvolution methods, but very different specificity values. The low specificity of ARMA modeling results from its instable behavior at border pixels between myocardium and LV. Taking into account all types of parameter maps, signal intensity maximum of SI data performed best. Combining this finding with the high correlation with the MBF suggests that signal intensity maximum can be considered a robust parameter for evaluation of myocardial perfusion at rest.

4.4 Outlier detection

A quality map was calculated to identify $[CA]$ time curves distorted due to imperfect motion correction of the DCE series. Figure 4.1 contrasts the fit of the sigmoid function of the quality map algorithm to a myocardial signal for which the motion correction produced a satisfying result (a) with the fit to two signals that were detected as outliers ((b) and (c)). The phases where the motion correction algorithm showed the highest potential to produce unsatisfying results were shortly before contrast agent arrival in the myocardium and right after first pass. This can be explained by the observation that patients typically breath in a bit deeper before breath hold and show an irregular breathing pattern right afterwards,

which causes strong displacements of the heart in the raw (not motion-corrected) DCE series.

Including outlier suppression in the determination of myocardial blood flow did not change the global mean MBF values significantly (p-values were 0.547, 0.826 and 0.059 for Fermi modeling, Tikhonov regularization and ARMA modeling, respectively). However, R^2 values of all method comparisons increased, especially the ones with ARMA modeling. The reason for ARMA modeling appearing most sensitive to imperfect motion correction may be that it simply reflects the linear differential relation between given AIF and myocardial signal, which makes the ARMA approach vulnerable to heavily distorted signal curves.

It should be pointed out that the quality map approach cannot distinguish between signal distortions due to motion or other sources like partial volume effects. However, it was referred to as motion correction quality map since imperfect motion correction appeared to be the major reason for distorted signals inside the segmented myocardial ROI (which already excludes border pixels to the LV and structures outside the myocardium). Furthermore, outlier detection using a median-derived threshold based on the assumption that motion correction worked well for the majority of the pixels in the myocardial ROI. Finally, the sigmoid fit function obviously cannot model the shape of each type of myocardial tissue curve since depending on the patient the myocardial signal may show an increase or decrease in amplitude after the first pass. However, that only few parameters need to be fitted makes this approach very robust. Moreover, outlier detection in the myocardial ROI works with relative quality values, which allows to spot heavily distorted signals because they do not deviate from the sigmoid curve in the same pattern as the other myocardial signals in the ROI.

4.5 Limitations

The obtained estimates of absolute myocardial blood flow could not be compared with results of the gold standard method PET since the group of patients did not undergo PET examinations. Also, examinations under pharmacological stress were not feasible.

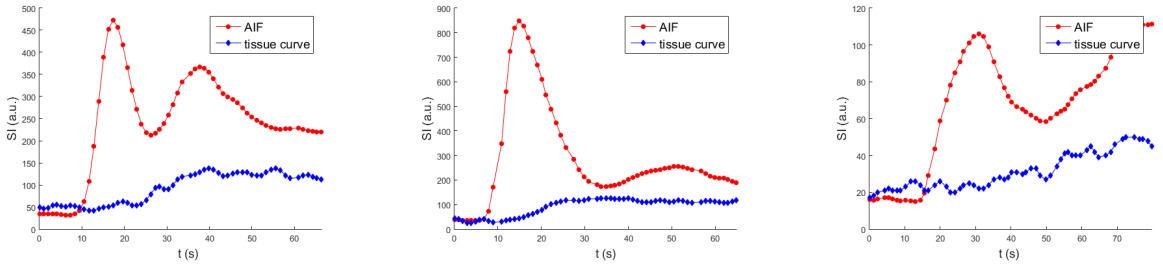

(a) (b) (c)

Figure 4.2: Arterial input function (AIF) and exemplary myocardial tissue curve of each patient excluded from comparative analysis. For the first patient, the maximum of the tissue curve was reached after the detected end of first pass (a). The second patient had a sampling gap in the up-slope phase of the AIF (b) and the third patient exhibited generally heavily distorted signals (c).

Furthermore, the sample size of patients was very small. Three of the eleven patients were excluded from comparative analysis due to characteristics of their SI time curves. The first excluded patient exhibited myocardial tissue curves which reached their maximum value after the automatically determined end of first pass (see Figure 4.2 (a)). As mentioned before, this was a substantial problem for deconvolution with the Fermi method, but also the algorithm for determination of the semi-quantitative parameters failed in this case since it also only evaluates the first pass restricted signal. Consequently, the commonly applied determination of end of first pass at the valley point of the AIF should be revised. The second excluded patient had a sampling gap resulting from a missed ECG trigger exactly at the up-slope part of the AIF (see Figure 4.2 (b)). This was a particular problem for the algorithm calculating the up-slope which determined a probably too steep up-slope for the AIF. A solution to this problem may be fitting a gamma variate function to the AIF. For the deconvolution methods the sensitivity to single sampling gaps is assumed to be small since they are applied on the entire (or first pass restricted) signal curve. The third patient was excluded due to heavily distorted myocardial SI time curves, whose maximum was not reached before the detected end of first pass (see Figure 4.2 (c)). Also the AIF exhibited a very uncommon shape. The deviation of the expected curve shapes may have been caused by this patient's atrial fibrillation.

Regarding the visual analysis of semi-quantitative parameter and MBF maps it should be mentioned that the windowing was not optimized. Furthermore, applying a 2D smoothing filter on the maps may have increased the visibility of perfusion deficits, especially in the semi-quantitative parameter maps of $[CA]$ data and the MBF maps.

The success of semi-quantitative and quantitative perfusion analysis depends fundamentally on the quality of preceding image registration. Moreover, segmentation has a crucial influence on the statistical analysis of the values inside the defined region. The DCE data was registered by an in-line program of the MR Scanner directly after image acquisition. Standard instead of advanced settings were chosen to save computation time. Segmentation was done manually by a moderately experienced user. Therefore, it cannot be ruled out that occasionally signals from outside the myocardium were included in the myocardial ROI.

Several limitations concern the estimation of contrast agent concentration from signal intensity. First, the same constant flip angle was assumed for every pixel because the acquisition of B_1 maps of the heart for B_1 inhomogeneity correction was not feasible in the clinical setting. Second, the MOLLI sequence is known to underestimate the T_1 value [104], but still was chosen due to its robustness and high precision [104]. An anyway probably more significant limitation in T_1 determination was the estimation of the pre-contrast myocardial T_1 value from a single ROI in the T_1 map. A sector-wise estimation of T_1 values would have been desirable, but was not feasible due to issues regarding resolution and partial volume effects in the T_1 maps. Further investigations will be needed to evaluate the influence of varying myocardial T_1 values on perfusion quantification. Third, employing Equation (1.1), fast water exchange [105] and the same T_1 relaxivity constant were assumed for the left ventricular blood pool and the myocardium. The fast exchange assumption may hold for whole blood, but may be inappropriate for myocardial tissue, whose water exchange might rather be described using the slow or intermediate exchange condition [105]. However, if and under which conditions water exchange influences the analysis of myocardial DCE-MRI using extracellular contrast agents is controversial [106, 107] and still a topic of ongoing research.

4.6 Conclusion

Pixel-wise quantification of myocardial blood flow was feasible with all three deconvolution methods (Fermi modeling, Tikhonov regularization with B-splines, ARMA modeling). Methodological differences led to significantly different global mean MBF estimates for each approach. However, the correlations between the results of the different deconvolution methods (especially Fermi modeling and Tikhonov regularization with B-splines) were strong. Considering practical aspects, Fermi modeling appeared to be the preferable deconvolution method due to its robustness and computational efficiency. Tikhonov regularization with B-splines was the slowest method and requires a refinement of the determination of the optimal regularization parameter in order to be generally applicable in pixel-wise analysis. ARMA modeling has shown to be sensitive to signal distortions due to imperfect motion correction.

Determination of pixel-wise semi-quantitative parameters turned out to be less trivial than often stated in the literature. Sophisticated denoising methods and minimum/maximum detection are necessary to cope with all kinds of physiologic and pathologic signal shapes. Assuming MBF estimates describe myocardial perfusion accurately, the comparison with semi-quantitative parameters of $[CA]$ data indicated that certain semi-quantitative parameters may not be appropriate descriptors of myocardial perfusion. Only the parameter signal intensity maximum showed high correlations with MBF estimates. The comparison of MBF estimates and semi-quantitative parameters of SI data showed that there is no strong correlation between them. Consequently, semi-quantitative parameters determined for data acquired in a standard clinical setting cannot be used as an estimator for absolute myocardial perfusion.

Pixel-wise quantitative perfusion maps have shown to be insensitive to the dark rim artifact and to clearly display information about location and transmurality of perfusion deficits. For pure visual analysis, maps of SI semi-quantitative parameters are preferable - especially the signal intensity maximum map - due to their low noise level. It can be concluded that visual analysis of pixel-wise quantitative perfusion maps has the potential to replace visual

analysis of DCE series in the future.

Retrospective conversion from signal intensity to contrast agent concentration using a signal model allows for standard clinical imaging procedures and contrast agent dosages recommended by clinical guidelines. However, for more accurate estimates of contrast agent concentration several aspects need to be improved, especially the estimation of myocardial pre-contrast T_1 values from T_1 maps.

Further research is needed to evaluate the behavior of the semi-quantitative and quantitative methods when they are applied on myocardial DCE-MRI data acquired in patients under stress condition.

Bibliography

[1] ADAM Health Solutions. URL: https://www.nlm.nih.gov/medlineplus/ency/imagepages/9367.htm.

[2] Spencer J. H., Anderson S. E., and Iaizzo P. A. Human coronary venous anatomy: implications for interventions. *Journal of cardiovascular translational research* Vol. 6 No. 2 (2013), pp. 208–217.

[3] Katz A. M. *Physiology of the Heart*. Fourth Edition. LWW, Nov. 2005. ISBN: 9780781755016.

[4] Schelbert H. R. Anatomy and physiology of coronary blood flow. *Journal of nuclear cardiology* Vol. 17 No. 4 (2010), pp. 545–554.

[5] Lilly L. *Pathophysiology of Heart Disease: A Collaborative Project of Medical Students and Faculty*. Third Edition. LWW, Oct. 2002. ISBN: 9780781740272.

[6] Gebker R. and Fleck E. Pathophysiology of myocardial perfusion. In: E N., Rossum AC van, and E F. *Cardiovascular Magnetic Resonance*. Steinkopff Verlag, Darmstadt, 2004, pp. 181–85. ISBN: 978-3-642-62152-9.

[7] Jerosch-Herold M. Quantification of myocardial perfusion by cardiovascular magnetic resonance. *J Cardiovasc Magn Reson* Vol. 12 No. 1 (2010), p. 57.

[8] Gerber B. L., Raman S. V., Nayak K., Epstein F. H., Ferreira P., Axel L., and Kraitchman D. L. Myocardial first-pass perfusion cardiovascular magnetic resonance: history, theory, and current state of the art. *Journal of Cardiovascular Magnetic Resonance* Vol. 10 No. 1 (2008), p. 18.

[9] Bellin M.-F. and Van Der Molen A. J. Extracellular gadolinium-based contrast media: an overview. *European journal of radiology* Vol. 66 No. 2 (2008), pp. 160–167.

[10] Kramer C. M., Barkhausen J., Flamm S. D., Kim R. J., Nagel E., et al. Standardized cardiovascular magnetic resonance (CMR) protocols 2013 update. *J Cardiovasc Magn Reson* Vol. 15 No. 1 (2013), p. 91.

[11] Reiter U. and Reiter G. *MR-Herzbildgebung interaktiv*. First Edition. Georg Thieme Verlag Stuttgart, 2009. ISBN: 978-3-13-148551-9.

[12] Rohrer M., Bauer H., Mintorovitch J., Requardt M., and Weinmann H.-J. Comparison of magnetic properties of MRI contrast media solutions at different magnetic field strengths. *Investigative radiology* Vol. 40 No. 11 (2005), pp. 715–724.

[13] Laurent S., Elst L. V., and Muller R. N. Comparative study of the physicochemical properties of six clinical low molecular weight gadolinium contrast agents. *Contrast media & molecular imaging* Vol. 1 No. 3 (2006), pp. 128–137.

[14] Mikawa M., Miwa N., Bräutigam M., Akaike T., and Maruyama A. Gd3+-loaded polyion complex for pH depiction with magnetic resonance imaging. *Journal of biomedical materials research* Vol. 49 No. 3 (2000), pp. 390–395.

[15] Stanisz G. J. and Henkelman R. M. Gd-DTPA relaxivity depends on macromolecular content. *Magnetic Resonance in Medicine* Vol. 44 No. 5 (2000), pp. 665–667.

[16] Rehwald W. G., Wagner A., and Albert T. S. E. Clinical Cardiovascular Magnetic Resonance Imaging Techniques. In: Warren J. Manning D. J. P. *Cardiovascular Magnetic Resonance*. Second Edition. Elsevier Ltd, Oxford, 2010. ISBN: 0443066868.

[17] Weber S., Kronfeld A., Kunz R. P., Fiebich M., Horstick G., Kreitner K.-F., and Schreiber W. G. Comparison of three accelerated pulse sequences for semiquantitative myocardial perfusion imaging using sensitivity encoding incorporating temporal filtering (TSENSE). *Journal of Magnetic Resonance Imaging* Vol. 26 No. 3 (2007), pp. 569–579.

[18] Arai A. E. Magnetic resonance first-pass myocardial perfusion imaging. *Topics in Magnetic Resonance Imaging* Vol. 11 No. 6 (2000), pp. 383–398.

[19] Schreiber W. G., Schmitt M., Kalden P., Mohrs O. K., Kreitner K.-F., and Thelen M. Dynamic contrast-enhanced myocardial perfusion imaging using saturation-prepared TrueFISP. *Journal of Magnetic Resonance Imaging* Vol. 16 No. 6 (2002), pp. 641–652.

[20] Barkhausen J., Hunold P., Jochims M., and Debatin J. F. Imaging of myocardial perfusion with magnetic resonance. *Journal of Magnetic Resonance Imaging* Vol. 19 No. 6 (2004), pp. 750–757.

[21] Di Bella E., Parker D., and Sinusas A. On the dark rim artifact in dynamic contrast-enhanced MRI myocardial perfusion studies. *Magnetic resonance in medicine* Vol. 54 No. 5 (2005), pp. 1295–1299.

[22] Storey P., Chen Q., Li W., Edelman R. R., and Prasad P. V. Band artifacts due to bulk motion. *Magnetic resonance in medicine* Vol. 48 No. 6 (2002), pp. 1028–1036.

[23] Lyne J. C., Gatehouse P. D., Assomull R. G., Smith G. C., Kellman P., Firmin D. N., and Pennell D. J. Direct comparison of myocardial perfusion cardiovascular magnetic resonance sequences with parallel acquisition. *Journal of Magnetic Resonance Imaging* Vol. 26 No. 6 (2007), pp. 1444–1451.

[24] Sung K. and Nayak K. S. Measurement and characterization of RF nonuniformity over the heart at 3T using body coil transmission. *Journal of Magnetic Resonance Imaging* Vol. 27 No. 3 (2008), pp. 643–648.

[25] Wieben O., Francois C., and Reeder S. B. Cardiac MRI of ischemic heart disease at 3T: potential and challenges. *European journal of radiology* Vol. 65 No. 1 (2008), pp. 15–28.

[26] Kim D., Gonen O., Oesingmann N., and Axel L. Comparison of the effectiveness of saturation pulses in the heart at 3T. *Magnetic resonance in medicine* Vol. 59 No. 1 (2008), pp. 209–215.

[27] Kellman P. and Arai A. E. Imaging sequences for first pass perfusion - a review. *Journal of Cardiovascular Magnetic Resonance* Vol. 9 No. 3 (2007), pp. 525–537.

[28] Kremers F. P., Hofman M., Groothuis J. G., Jerosch-Herold M., Beek A. M., Zuehlsdorff S., Nielles-Vallespin S., Rossum A. C. van, and Heethaar R. M. Improved correction of spatial inhomogeneities of surface coils in quantitative analysis of first-pass myocardial perfusion imaging. *Journal of Magnetic Resonance Imaging* Vol. 31 No. 1 (2010), pp. 227–233.

[29] Utz W., Niendorf T., Wassmuth R., Messroghli D., Dietz R., and Schulz-Menger J. Contrast–dose relation in first-pass myocardial MR perfusion imaging. *Journal of Magnetic Resonance Imaging* Vol. 25 No. 6 (2007), pp. 1131–1135.

[30] Vallée J.-P., Lazeyras F., Kasuboski L., Chatelain P., Howarth N., Righetti A., and Didier D. Quantification of myocardial perfusion with FAST sequence and Gd bolus in patients with normal cardiac function. *Journal of Magnetic Resonance Imaging* Vol. 9 No. 2 (1999), pp. 197–203.

[31] Jerosch-Herold M., Wilke N., Stillman A. E., and Wilson R. F. Magnetic resonance quantification of the myocardial perfusion reserve with a Fermi function model for constrained deconvolution. *Medical physics* Vol. 25 No. 1 (1998), pp. 73–84.

[32] Christian T. F., Rettmann D. W., Aletras A. H., Liao S. L., Taylor J. L., Balaban R. S., and Arai A. E. Absolute myocardial perfusion in canines measured by using dual-bolus first-pass MR imaging. *Radiology* Vol. 232 No. 3 (2004), pp. 677–684.

[33] Gatehouse P. D., Elkington A. G., Ablitt N. A., Yang G.-Z., Pennell D. J., and Firmin D. N. Accurate assessment of the arterial input function during high-dose myocardial perfusion cardiovascular magnetic resonance. *Journal of Magnetic Resonance Imaging* Vol. 20 No. 1 (2004), pp. 39–45.

[34] Bokacheva L., Rusinek H., Chen Q., Oesingmann N., Prince C., Kaur M., Kramer E., and Lee V. S. Quantitative determination of Gd-DTPA concentration in T1-weighted MR renography studies. *Magnetic resonance in medicine* Vol. 57 No. 6 (2007), pp. 1012–1018.

[35] Cernicanu A. and Axel L. Theory-based signal calibration with single-point T1 measurements for first-pass quantitative perfusion MRI studies. *Academic radiology* Vol. 13 No. 6 (2006), pp. 686–693.

[36] Heydari B., Kwong R. Y., and Jerosch-Herold M. Technical advances and clinical applications of quantitative myocardial blood flow imaging with cardiac MRI. *Progress in cardiovascular diseases* Vol. 57 No. 6 (2015), pp. 615–622.

[37] Gupta V., Kirişli H. A., Hendriks E. A., Geest R. J. van der, Giessen M. van de, Niessen W., Reiber J. H., and Lelieveldt B. P. Cardiac MR perfusion image processing techniques: a survey. *Medical image analysis* Vol. 16 No. 4 (2012), pp. 767–785.

[38] Hsu L.-Y., Groves D. W., Aletras A. H., Kellman P., and Arai A. E. A quantitative pixel-wise measurement of myocardial blood flow by contrast-enhanced first-pass CMR perfusion imaging: microsphere validation in dogs and feasibility study in humans. *JACC: Cardiovascular Imaging* Vol. 5 No. 2 (2012), pp. 154–166.

[39] Weng A., Ritter C., Beer M., Hahn D., and Köstler H. Quantitative pixelwise myocardial perfusion maps from first-pass perfusion MRI. *The British journal of radiology* Vol. 87 No. 1039 (2014).

[40] Nagel E., Klein C., Paetsch I., Hettwer S., Schnackenburg B., Wegscheider K., and Fleck E. Magnetic resonance perfusion measurements for the noninvasive detection of coronary artery disease. *Circulation* Vol. 108 No. 4 (2003), pp. 432–437.

[41] Al-Saadi N., Nagel E., Gross M., Schnackenburg B., Paetsch I., Klein C., and Fleck E. Improvement of myocardial perfusion reserve early after coronary intervention: assessment with cardiac magnetic resonance imaging. *Journal of the American College of Cardiology* Vol. 36 No. 5 (2000), pp. 1557–1564.

[42] Koh T. S., Bisdas S., Koh D. M., and Thng C. H. Fundamentals of tracer kinetics for dynamic contrast-enhanced MRI. *Journal of Magnetic Resonance Imaging* Vol. 34 No. 6 (2011), pp. 1262–1276.

[43] Zierler K. L. Equations for measuring blood flow by external monitoring of radioisotopes. *Circulation Research* Vol. 16 No. 4 (1965), pp. 309–321.

[44] Clough A. V., Al-Tinawi A., Linehan J. H., and Dawson C. A. Regional transit time estimation from image residue curves. *Annals of biomedical engineering* Vol. 22 No. 2 (1994), pp. 128–143.

[45] Vinnakota K. C. and Bassingthwaighte J. B. Myocardial density and composition: a basis for calculating intracellular metabolite concentrations. *American Journal of Physiology-Heart and Circulatory Physiology* Vol. 286 No. 5 (2004), H1742–H1749.

[46] Lee D. C. and Johnson N. P. Quantification of absolute myocardial blood flow by magnetic resonance perfusion imaging. *JACC: Cardiovascular Imaging* Vol. 2 No. 6 (2009), pp. 761–770.

[47] Jerosch-Herold M., Swingen C., and Seethamraju R. T. Myocardial blood flow quantification with MRI by model-independent deconvolution. *Medical physics* Vol. 29 No. 5 (2002), pp. 886–897.

[48] Neyran B., Janier M. F., Casali C., Revel D., and Canet Soulas E. P. Mapping myocardial perfusion with an intravascular MR contrast agent: robustness of deconvolution methods at various blood flows. *Magnetic resonance in medicine* Vol. 48 No. 1 (2002), pp. 166–179.

[49] Zarinabad N., Chiribiri A., Hautvast G. L., Ishida M., Schuster A., Cvetkovic Z., Batchelor P. G., and Nagel E. Voxel-wise quantification of myocardial perfusion by cardiac magnetic resonance. Feasibility and methods comparison. *Magnetic resonance in medicine* Vol. 68 No. 6 (2012), pp. 1994–2004.

[50] Miller C. A., Naish J. H., Ainslie M. P., Tonge C., Tout D., Arumugam P., Banerji A., Egdell R. M., Clark D., Weale P., et al. Voxel-wise quantification of myocardial blood flow with cardiovascular magnetic resonance: effect of variations in methodology and validation with positron emission tomography. *Journal of Cardiovascular Magnetic Resonance* Vol. 16 No. 1 (2014).

[51] Ólafsdóttir H., Stegmann M. B., and Larsson H. B. Automatic assessment of cardiac perfusion MRI. In: *International Conference on Medical Image Computing and Computer-Assisted Intervention*. Springer. 2004, pp. 1060–1061.

[52] Xue H., Zuehlsdorff S., Kellman P., Arai A., Nielles-Vallespin S., Chefdhotel C., Lorenz C. H., and Guehring J. Unsupervised inline analysis of cardiac perfusion MRI. In: *International Conference on Medical Image Computing and Computer-Assisted Intervention*. Springer. 2009, pp. 741–749.

[53] Beache G. M., Khalifa F., El-Baz A., and Gimelfarb G. Fully automated framework for the analysis of myocardial first-pass perfusion MR images. *Medical physics* Vol. 41 No. 10 (2014).

[54] Messroghli D. R., Plein S., Higgins D. M., Walters K., Jones T. R., Ridgway J. P., and Sivananthan M. U. Human Myocardium: Single-Breath-hold MR T1 Mapping with High Spatial Resolution-Reproducibility Study. *Radiology* Vol. 238 No. 3 (2006), pp. 1004–1012.

[55] Xue H., Shah S., Greiser A., Guetter C., Littmann A., Jolly M.-P., Arai A. E., Zuehlsdorff S., Guehring J., and Kellman P. Motion correction for myocardial T1 mapping using image registration with synthetic image estimation. *Magnetic resonance in medicine* Vol. 67 No. 6 (2012), pp. 1644–1655.

[56] Hautvast G., Chiribiri A., Zarinabad N., Schuster A., Breeuwer M., and Nagel E. Myocardial blood flow quantification from MRI by deconvolution using an exponential approximation basis. *IEEE Transactions on Biomedical Engineering* Vol. 59 No. 7 (2012), pp. 2060–2067.

[57] Biglands J., Magee D., Boyle R., Larghat A., Plein S., and Radjenović A. Evaluation of the effect of myocardial segmentation errors on myocardial blood flow estimates from DCE-MRI. *Physics in medicine and biology* Vol. 56 No. 8 (2011), p. 2423.

[58] Positano V., Santarelli M. F., and Landini L. Automatic characterization of myocardial perfusion in contrast enhanced MRI. *EURASIP Journal on Applied Signal Processing* Vol. 2003 (2003), pp. 413–421.

[59] Brix G., Schad L. R., Deimling M., and Lorenz W. J. Fast and precise T1 imaging using a TOMROP sequence. *Magnetic resonance imaging* Vol. 8 No. 4 (1990), pp. 351–356.

[60] Fritsch F. N. and Carlson R. E. Monotone piecewise cubic interpolation. *SIAM Journal on Numerical Analysis* Vol. 17 No. 2 (1980), pp. 238–246.

[61] DiBella E. and Kholmovski E. Accuracy of assuming uniform temporal sampling in the analysis of cardiac perfusion MRI datasets. In: *Proc Intl Soc Mag Reson Med.* Vol. 3577. 2006.

[62] Jolliffe I. *Principal Component Analysis (Springer Series in Statistics).* 2nd. Springer, Oct. 2002. ISBN: 9780387954424.

[63] Hansen P. C. *Rank-Deficient and Discrete Ill-Posed Problems: Numerical Aspects of Linear Inversion (Monographs on Mathematical Modeling and Computation).* Society for Industrial and Applied Mathematics, 1998. ISBN: 9780898714036.

[64] Golub P. G. H. and Loan P. C. F. V. *Matrix Computations (Johns Hopkins Studies in the Mathematical Sciences).* 3rd. The Johns Hopkins University Press, Oct. 1996. ISBN: 9780801854132.

[65] Jackson J. E. *A User's Guide to Principal Components.* 1st ed. Wiley-Interscience, Mar. 1991. ISBN: 9780471622673.

[66] Balvay D., Kachenoura N., Espinoza S., Thomassin-Naggara I., Fournier L. S., Clement O., and Cuenod C.-A. Signal-to-noise ratio improvement in dynamic contrast-enhanced CT and MR imaging with automated principal component analysis filtering. *Radiology* Vol. 258 No. 2 (2011), pp. 435–445.

[67] Balvay D., Frouin F., Calmon G., Bessoud B., Kahn E., Siauve N., Clément O., and Cuenod C. A. New criteria for assessing fit quality in dynamic contrast-enhanced T1-weighted MRI for perfusion and permeability imaging. *Magnetic resonance in medicine* Vol. 54 No. 4 (2005), pp. 868–877.

[68] Reeder S. B., Wintersperger B. J., Dietrich O., Lanz T., Greiser A., Reiser M. F., Glazer G. M., and Schoenberg S. O. Practical approaches to the evaluation of signal-to-noise ratio performance with parallel imaging: Application with cardiac imaging and a 32-channel cardiac coil. *Magnetic Resonance in Medicine* Vol. 54 No. 3 (2005), pp. 748–754.

[69] Price R. R., Axel L., Morgan T., Newman R., Perman W., Schneiders N., Selikson M., Wood M., and Thomas S. R. Quality assurance methods and phantoms for magnetic resonance imaging: report of AAPM nuclear magnetic resonance Task Group No. 1. *Medical physics* Vol. 17 No. 2 (1990), pp. 287–295.

[70] Dietrich O., Raya J. G., Reeder S. B., Reiser M. F., and Schoenberg S. O. Measurement of signal-to-noise ratios in MR images: Influence of multichannel coils, parallel imaging, and reconstruction filters. *Journal of Magnetic Resonance Imaging* Vol. 26 No. 2 (2007), pp. 375–385.

[71] Freedman D. and Diaconis P. On the histogram as a density estimator: L 2 theory. *Probability theory and related fields* Vol. 57 No. 4 (1981), pp. 453–476.

[72] Savitzky A. and Golay M. J. Smoothing and differentiation of data by simplified least squares procedures. *Analytical chemistry* Vol. 36 No. 8 (1964), pp. 1627–1639.

[73] Press W. H., Flannery B. P., Teukolsky S. A., and Vetterling W. T. *Numerical Recipes in C: The Art of Scientific Computing, Second Edition*. 2nd ed. Cambridge University Press, Oct. 1992. ISBN: 9780521431088.

[74] Axel L. Tissue mean transit time from dynamic computed tomography by a simple deconvolution technique. *Investigative radiology* Vol. 18 No. 1 (1983), pp. 94–99.

[75] Jerosch-Herold M., Hu X., Murthy N. S., and Seethamraju R. T. Time delay for arrival of MR contrast agent in collateral-dependent myocardium. *IEEE Transactions on medical imaging* Vol. 23 No. 7 (2004), pp. 881–890.

[76] Tikhonov A., Goncharsky A., Stepanov V., and Yagola A. G. *Numerical Methods for the Solution of Ill-Posed Problems*. Dortrecht: Kluwer, Dec. 1995. The Netherlands.

[77] Verotta D. Estimation and model selection in constrained deconvolution. *Annals of biomedical engineering* Vol. 21 No. 6 (1993), pp. 605–620.

[78] Hansen P. C. Analysis of discrete ill-posed problems by means of the L-curve. *SIAM review* Vol. 34 No. 4 (1992), pp. 561–580.

[79] Hansen P. C. Regularization tools: A Matlab package for analysis and solution of discrete ill-posed problems. *Numerical algorithms* Vol. 6 No. 1 (1994), pp. 1–35.

[80] Batchelor P., Chiribiri A., Nooralipour N. Z., and Cvetkovic Z. ARMA regularization of cardiac perfusion modeling. In: *ICASSP*. 2010, pp. 642–645.

[81] Ljung L. and Glad T. *Modeling of Dynamic Systems*. 1st ed. Prentice Hall, May 1994. ISBN: 9780135970973.

[82] Murase K., Yamazaki Y., and Shinohara M. Autoregressive moving average (ARMA) model applied to quantification of cerebral blood flow using dynamic susceptibility contrast-enhanced magnetic resonance imaging. *Magnetic Resonance in Medical Sciences* Vol. 2 No. 2 (2003), pp. 85–95.

[83] Wiart M., Rognin N., Berthezene Y., Nighoghossian N., Froment J.-C., and Baskurt A. Perfusion-based segmentation of the human brain using similarity mapping. *Magnetic resonance in medicine* Vol. 45 No. 2 (2001), pp. 261–268.

[84] Oppenheim A. V., Schafer R. W., and Buck J. R. *Discrete-Time Signal Processing*. 2nd ed. Prentice Hall, Jan. 1999. ISBN: 9780137549207.

[85] Hsu L.-Y., Kellman P., and Arai A. E. Nonlinear myocardial signal intensity correction improves quantification of contrast-enhanced first-pass MR perfusion in humans. *Journal of Magnetic Resonance Imaging* Vol. 27 No. 4 (2008), pp. 793–801.

[86] Ichihara T., Ishida M., Kitagawa K., Ichikawa Y., Natsume T., Yamaki N., Maeda H., Takeda K., and Sakuma H. Quantitative analysis of first-pass contrast-enhanced myocardial perfusion MRI using a patlak plot method and blood saturation correction. *Magnetic resonance in medicine* Vol. 62 No. 2 (2009), pp. 373–383.

[87] Pack N. A., DiBella E. V., Rust T. C., Kadrmas D. J., McGann C. J., Butterfield R., Christian P. E., and Hoffman J. M. Estimating myocardial perfusion from dynamic contrast-enhanced CMR with a model-independent deconvolution method. *Journal of Cardiovascular Magnetic Resonance* Vol. 10 No. 1 (2008).

[88] Pack N. A. and DiBella E. V. Comparison of myocardial perfusion estimates from dynamic contrast-enhanced magnetic resonance imaging with four quantitative analysis methods. *Magnetic resonance in medicine* Vol. 64 No. 1 (2010), pp. 125–137.

[89] Schuster A., Zarinabad N., Ishida M., Sinclair M., Wijngaard J. P. van den, Morton G., Hautvast G. L., Bigalke B., Horssen P. van, Smith N., et al. Quantitative assessment of magnetic resonance derived myocardial perfusion measurements using advanced techniques: microsphere validation in an explanted pig heart system. *Journal of Cardiovascular Magnetic Resonance* Vol. 16 No. 1 (2014).

[90] Petersen S. E., Jerosch-Herold M., Hudsmith L. E., Robson M. D., Francis J. M., Doll H. A., Selvanayagam J. B., Neubauer S., and Watkins H. Evidence for microvascular dysfunction in hypertrophic cardiomyopathy, New insights from multiparametric magnetic resonance imaging. *Circulation* Vol. 115 No. 18 (2007), pp. 2418–2425.

[91] Sourbron S., Luypaert R., Van Schuerbeek P., Dujardin M., and Stadnik T. Choice of the regularization parameter for perfusion quantification with MRI. *Physics in medicine and biology* Vol. 49 No. 14 (2004).

[92] Keeling S. L., Kogler T., and Stollberger R. Deconvolution for DCE-MRI using an exponential approximation basis. *Medical image analysis* Vol. 13 No. 1 (2009), pp. 80–90.

[93] Zarinabad N., Hautvast G. L., Sammut E., Arujuna A., Breeuwer M., Nagel E., and Chiribiri A. Effects of tracer arrival time on the accuracy of high-resolution (voxel-wise) myocardial perfusion maps from contrast-enhanced first-pass perfusion magnetic resonance. *IEEE Transactions on Biomedical Engineering* Vol. 61 No. 9 (2014), pp. 2499–2506.

[94] Sammut E., Zarinabad N., Vianello P. F., and Chiribiri A. Quantitative Assessment of Perfusion–Where Are We Now? *Current Cardiovascular Imaging Reports* Vol. 7 No. 7 (2014), pp. 1–11.

[95] Zarinabad N., Chiribiri A., Hautvast G. L., Shuster A., Sinclair M., Wijngaard J. P. van den, Smith N., Spaan J. A., Siebes M., Breeuwer M., et al. Modelling parameter role on accuracy of cardiac perfusion quantification. In: *International Conference on Functional Imaging and Modeling of the Heart*. Springer. 2013, pp. 370–382.

[96] Gooijer J. G. de, Abraham B., Gould A., and Robinson L. Methods for determining the order of an autoregressive-moving average process: A survey. *International Statistical Review/Revue Internationale de Statistique* (1985), pp. 301–329.

[97] Biglands J. D., Magee D. R., Sourbron S. P., Plein S., Greenwood J. P., and Radjenovic A. Comparison of the diagnostic performance of four quantitative myocardial perfusion estimation methods used in cardiac mr imaging: ce-marc substudy. *Radiology* Vol. 275 No. 2 (2015), pp. 393–402.

[98] Kim S. M., Haider M. A., Jaffray D. A., and Yeung I. W. Improved accuracy of quantitative parameter estimates in dynamic contrast-enhanced CT study with low temporal resolution. *Medical physics* Vol. 43 No. 1 (2016), pp. 388–400.

[99] Al-Saadi N., Gross M., Bornstedt A., Schnackenburg B., Klein C., Fleck E., and Nagel E. Vergleich verschiedener Parameter zur Bestimmung eines Index der myokardialen Perfusionsreserve zur Erkennung von Koronarstenosen mit kardiovaskulärer Magnetresonanztomographie. *Zeitschrift für Kardiologie* Vol. 90 No. 11 (2001), pp. 824–834. ISSN: 1435-1285.

[100] Lee D. C., Johnson N. P., O'Hara K., and Harris K. R. Correcting the underestimation of absolute myocardial blood flow by magnetic resonance perfusion imaging. *Circulation* Vol. 118 No. Suppl 18 (2008), pp. 645–646.

[101] Ruan C., Yang S., Clarke G. D., Amurao M. R., Partyka S. R., Bradley Y. C., and Cusi K. First-pass contrast-enhanced myocardial perfusion MRI using a maxi-

mum up-slope parametric map. *IEEE Transactions on Information Technology in Biomedicine* Vol. 10 No. 3 (2006), pp. 574–580.

[102] Huber A., Schweyer M., Bauner K., Theisen D., Rist C., Mühling O., Näbauer M., Schoenberg S., and Reiser M. MRT zur Beurteilung der Myokardperfusion. *Der Radiologe* Vol. 47 No. 4 (2007), pp. 319–324.

[103] Huber A., Sourbron S., Klauss V., Schaefer J., Bauner K. U., Schweyer M., Reiser M., Rummeny E., and Rieber J. Magnetic resonance perfusion of the myocardium: semiquantitative and quantitative evaluation in comparison with coronary angiography and fractional flow reserve. *Investigative radiology* Vol. 47 No. 6 (2012), pp. 332–338.

[104] Kellman P. and Hansen M. S. T1-mapping in the heart: accuracy and precision. *Journal of cardiovascular magnetic resonance* Vol. 16 No. 1 (2014).

[105] Donahue K. M., Weisskoff R. M., and Burstein D. Water diffusion and exchange as they influence contrast enhancement. *Journal of Magnetic Resonance Imaging* Vol. 7 No. 1 (1997), pp. 102–110.

[106] Larsson H. B., Rosenbaum S., and Fritz-Hansen T. Quantification of the effect of water exchange in dynamic contrast MRI perfusion measurements in the brain and heart. *Magnetic resonance in medicine* Vol. 46 No. 2 (2001), pp. 272–281.

[107] Judd R. M., Reeder S. B., and May-Newman K. Effects of water exchange on the measurement of myocardial perfusion using paramagnetic contrast agents. *Magnetic resonance in medicine* Vol. 41 No. 2 (1999), pp. 334–342.